3D Boundary Element Simulation of Droplet Dynamics in Microchannels: How Droplets Squeeze Through Constrictions and Move in Electric Fields

THÈSE N^{O} 8621 (2018)

PRÉSENTÉE LE 23 MAI 2018
À LA FACULTÉ DES SCIENCES ET TECHNIQUES DE L'INGÉNIEUR
COMPLEXITÉ ÉMERGENTE DANS LES SYSTÈMES PHYSIQUES
PROGRAMME DOCTORAL EN PHYSIQUE

ÉCOLE POLYTECHNIQUE FÉDÉRALE DE LAUSANNE

POUR L'OBTENTION DU GRADE DE DOCTEUR ÈS SCIENCES

PAR

Simon Sebastian SCHÜTZ

acceptée sur proposition du jury:

Prof. R. Houdré, président du jury
Prof. T. Schneider, directeur de thèse
Prof. J.-C. Baret, rapporteur
Prof. B. Scheid, rapporteur
Prof. F. Gallaire, rapporteur

ÉCOLE POLYTECHNIQUE
FÉDÉRALE DE LAUSANNE
Suisse
2018

Acknowledgements

The work presented in this thesis was carried out at the École Polytechnique Fédérale de Lausanne (EPFL) in the Emergent Complexity in Physical Systems laboratory (ECPS) between the spring of 2014 and the spring of 2018. In these four years, I have received the support and help from many people, who contributed their share to the success of this work.

First and foremost, I thank my thesis advisor, Tobias M. Schneider. As his first PhD student, I joined the ECPS lab right when it moved to Lausanne, and watched it grow from *two guys in two offices doing science* into a full laboratory. His enthusiasm, excitement and ability to see things in a larger context were a great motivation for me. He entrusted me with the responsibility of choosing and implementing my own solutions to the challenges I encountered in my research, but was always available to support me with resources, sound advice, and encouragement.

I express my gratitude to professors François Gallaire, Jean-Christophe Baret and Sindy Tang. François has been following my progress since the beginning of my thesis, and gave valuable feedback in my PhD candidacy exam and on other occasions. Jean-Christophe hosted me for a week in his experimental lab in Bordeaux, and shared with me his research idea on droplet sorting, which was to become a central part of my PhD work. In Sindy's lab in Stanford, I spent three exciting weeks, matching experiment and simulation for two-droplet interaction.

I thank all members of the ECPS lab, past and present: Tobias Kreilos, Florian Reetz (geb. Sprung), Sajjad Azimi, Laureline Hentgen, Mirko Farano, Iryna Sivak, Emilio Lozano, Ayşe Yeşil, and Alessia Ferraro. Tobias joined shortly after me, and his presence turned ECPS into a lab. I fondly remember the time when all ECPS students — Tobias, Florian, Sajjad and me — would fit into one office, the breaks by the lake and evenings of *Game of Thrones*. After moving into the new lake view office, Laureline and later Mirko were ideal office mates, with whom I shared leg space and valuable discussions. The last third of my PhD was the most turbulent, but quite enjoyable nonetheless, with five new colleagues, new traditions, lakeside barbecues, and numerous occasions where we had one beer and then went home. I thank Alessia for the time we shared. Thanks to Hecke Schrobsdorff for his support and updates from Göttingen, and to Petra Bendel, our lab's secretary, for her administrative support and for keeping an eye on the salmon.

I also thank the members of the Laboratory for Fluid Mechanics and Instabilities (LFMI), in particular Mathias Nagel, Lailai Zhu, Giacomo Gallino, and Gioele Balestra. Mathias' expertise in boundary element methods accelerated my start into this new field and method. Lailai gave me valuable suggestions on past research in boundary elements, and shared with me some of his data. Giacomo and Gioele started their PhD work at the same time as me, and I wish them all the best for the end of their theses and beyond.

I am grateful to Laura Chacon, Birte Riechers, Aurelie Vigne, and Kevin Bougis from CRPP Bordeaux, who hosted me during my research stay, showed me the city, and introduced me to working in a microfluidic laboratory. I thank my collaborators Ouriel Caën, Mani Teja Jammalamadaka and Thomas Beneyton for their contribution to our common research results on droplet sorting. I am also grateful to Jian-Wei Khor, Minkyu Kim and the other members of the Tang lab at Stanford university for hosting me in their laboratory, for valuable discussions and good scientific collaboration.

In the past four years, I spent much time in the office, but some also outside. I thank all my friends from the *Stammtisch*, particularly Wolfram, Jeremie, Margareta, Anna, Liz, Maryline, Robert and Tomáš. We had a wonderful time trying to speak German and French, sunny evenings at the lake, and many movie nights. The summer of 2016 was amazing. I thank Margareta for the time we spent together. Thanks to Danny and Min, who did not battle the french language, but joined for the rest of the fun. I thank Patricia for being my travel companion on several occasions, and her, Andy and Ali for weekly excursions into the mysteries of German grammar. I thank my roommates Christophe, Alisa, Alfonso, and Riccardo, who I saw much less frequently than I would have liked.

Hiking clears my mind. My special thanks go to Wolfram and Anna, who were my reliable partners in the most daring adventures. I thank Jeremie, Léo, Giuseppe, Tomáš, Kristina, Max, Erik, and many others who joined me in my quest for fresh air.

I acknowledge long-distance support from Göttingen, where I grew up. I thank Michelle and Frederic for numerous Skype calls and conversations, both in Lausanne and Göttingen. Thanks to Simon Christoph and Sebastian Stein, with whom I had the pleasure to do physics and other fun activities for the last 10 years. I thank Bettina and Stefan, who visited me in Switzerland to test their tolerance to altitude, and Ariane, who ended up doing the same.

I thank my family, my parents Hildegard and Kai-Uwe, my brother Leonard, and Maria, Maren and Jan. When you're out there, far away, in a place where you don't speak the language, it feels good to have a home.

A final thanks goes to Simon Christoph, Wolfram and Anna, who proofread this thesis for language and content, and gave me valuable feedback.

Lausanne, March 2018 Simon Schütz

Abstract

Flows of fluids with free surfaces show complex dynamical behavior. Examples include effects like capillary surface waves, topological transitions such as droplet breakup and coalescence, or pattern formation in wetting and de-wetting dynamics. These complex phenomena result from a highly nonlinear evolution that is driven by the interplay of surface forces and the changing surface geometry. Droplet-based microfluidics both utilizes the free-surface dynamics in a wide range of applications in science and engineering, and, due to the precise control of flows at small scales, allows to study the dynamics experimentally.

An analytical description of the dynamics is made difficult by the high degree of nonlinearity. Numerical tools complement experiments, as they give access to quantities of interest such as the pressure fields inside a fluid or local stresses on the interface, and allow for a precise control of parameters and models of physical effects. We use numerical tools to study the complex dynamics of free surface flows.

In the first part of this thesis, we develop a fully-resolved 3D boundary element method for simulating droplet dynamics in complex geometries. The developed numerical tool allows us to follow the dynamic deformation of droplets with variable viscosity ratio between droplet and continuous phase, under the effect of Young-Laplace surface tension, gravity, and dielectric stresses due to electric fields. Free interfaces are represented by a novel smooth surface representation that gives an accurate description for the surface shape and curvature.

In the second part, we address two practically relevant problems. First, we study the breakup of droplets as concentrated emulsions are injected into a narrow constriction, and describe the underlying physical mechanism that drives the breakup. Second, we analyze the efficiency of droplet sorting with dielectrophoresis, and propose a new sorting device that operates at lower voltage and reduces stress on the droplets. In careful quantitative comparisons between numerics and experiments, we find that in-plane surface stresses due to nonequilibrium surfactant distributions have a major impact on free interface dynamics, and merit further study.

Keywords: nonlinear physics, free surfaces, multi-phase flow, droplet microfluidics, lab-on-a-chip, boundary element method, droplet breakup, dielectrophoresis, droplet sorting

Zusammenfassung

Flüssigkeiten mit freien Grenzflächen zeigen ein komplexes dynamisches Verhalten, wie kapillare Oberflächenwellen, topologische Übergänge wie etwa Abriss und Verschmelzen von Tropfen, oder Musterbildung in der Benetzung von Oberflächen. Diese komplexen Phänomene sind Folge des hoch nichtlinearen Zusammenspiels von Oberflächenkräften und Veränderungen der Oberflächengeometrie. Tropfenbasierte Mikrofluidik nutzt die Dynamik freier Oberflächen in einem großen Anwendungsfeld in Wissenschaft und Technik, ermöglicht durch eine präzise Kontrolle von kleinskaligen Strömungen aber auch eine Untersuchung der Dynamik selbst.

Der hohe Grad an Nichtlinearität erschwert eine analytische Beschreibung der Dynamik. Numerische Simulationen ergänzen Experimente, indem sie relevante Größen wie die Druckverteilung in der Flüssigkeit oder die die Spannungen auf der Oberfläche zugänglich machen und eine präzise Kontrolle von Parametern und Modellen der physikalischen Effekte erlauben. Wir untersuchen die komplexe Dynamik von Strömungen mit freien Oberflächen numerisch.

Im ersten Teil dieser Arbeit entwickeln wir eine voll aufgelöste 3D Randelementmethode zur Simulation von Tropfendynamik in komplexen Geometrien. Die entwickelte Simulation ermöglicht die Untersuchung der dynamische Verformung von Tropfen mit variablem Viskositätsverhältnis zwischen Tropfen und umgebender Flüssigkeit, unter dem Einfluss von Young-Laplace-Oberflächenspannungen, Gravitation und dielektrischen Kräften durch elektrische Felder. Eine glatte Oberflächendarstellung ermöglicht eine genaue Beschreibung der Oberflächenform und Krümmung.

Im zweiten Teil behandeln wir zwei praktisch relevante Probleme. Erstens untersuchen wir das Auseinanderbrechen von Tropfen, wenn dichte Emulsionen in einen verengten Kanal einströmen, und beschreiben den zugrundeliegenden physikalischen Mechanismus. Zweitens analysieren wir die Effizienz des Sortierens von Tropfen durch Dielektrophorese, und entwickeln eine neue Geometrie, die mit geringerer elektrischer Spannung arbeitet und so die mechanische Verformung der Tropfen minimiert. Durch einen gründlichen quantitativen Vergleich zwischen Numerik und Experimenten erkennen wir, dass Spannungen in den Oberflächen, ausgelöst durch eine Nichtgleichgewichtsverteilung von Tensiden, einen signifikanten Einfluss auf die Oberflächendynamik haben und weiterer Untersuchung bedürfen.

Schlüsselwörter: Nichtlineare Physik, Freie Oberflächen, Mehrphasenströmung, Tropfenbasierte Mikrofluidik, lab-on-a-chip, Randelementmethode, Tropfenabriss, Dielektrophorese, Tropfensortierung

Contents

Acknowledgements **i**

Abstracts (English, Deutsch) **iii**

Contents **vii**

List of Figures **xi**

1 Introduction **1**
- 1.1 Droplet Dynamics in Microfluidics . . . 2
- 1.2 Numerical Simulation Methods for Multiphase Flow . . . 5
- 1.3 Structure of this Work . . . 7

2 Theory / Mathematical Model **9**
- 2.1 Boundary Integral Formulation for Stokes Flow . . . 10
  - 2.1.1 Fundamental Solution of Stokes Flow . . . 11
  - 2.1.2 Boundary Integral Equation for Stokes Flow . . . 12
  - 2.1.3 Boundary Conditions . . . 14
  - 2.1.4 Boundary Integral Equations with a Fluid Interface . . . 14
- 2.2 Boundary Integral Formulation for Electrostatics . . . 17
  - 2.2.1 Boundary Integral Equation for Electrostatics . . . 17
  - 2.2.2 Boundary Integral Equations with a Dielectric Interface . . . 19
- 2.3 Surface Stress Models for Stokes Flow . . . 21
  - 2.3.1 Young-Laplace Surface Tension Model . . . 21
  - 2.3.2 Dielectric Surface Stress . . . 22
  - 2.3.3 Surface Stress due to Gravity . . . 23
- 2.4 Further Relevant Boundary Integrals . . . 23
  - 2.4.1 Volume of a Domain . . . 24
  - 2.4.2 Center of Mass . . . 24
  - 2.4.3 Determine if a Point is Inside a Domain . . . 24
- 2.5 Stokes Flow in a Rectangular Duct . . . 25
  - 2.5.1 Series Representation for the Velocity . . . 25
  - 2.5.2 Approximation by a Biparabolic Profile . . . 26
  - 2.5.3 Pressure Gradient in a Rectangular Duct . . . 27

2.5.4 Poiseuille Flow 28
2.6 Summary 29

I Boundary Element Method for 3D Stokes Flow 31

3 Numerical Implementation 35
3.1 Boundary-Element Simulation of Stokes Flow 37
3.1.1 Discretizing the Boundary Integral Equations 38
3.1.2 Solving the Linear System 39
3.2 Boundary-Element Simulation for Electrostatics 40
3.3 Mesh and Surface Representation 41
3.3.1 Local Refinement 42
3.3.2 Treatment of Edges 42
3.3.3 Constraining Degrees of Freedom 43
3.4 Smooth Surface Representation 43
3.4.1 Approximating the Normal Vector 44
3.4.2 Locally Fitting a Paraboloid 44
3.4.3 Interpolating Between Corner Vertices of a Cell 46
3.4.4 Properties of the Representation 46
3.5 Numerical Integration 49
3.5.1 Nearly Singular Integration 49
3.5.2 Accuracy of the Numerical Quadrature 50
3.6 Time Stepping 53
3.6.1 Stability of the Time Stepping 53
3.6.2 Mesh Regularization 54
3.7 Implementation 55
3.7.1 Parallelization 55
3.8 Summary 57

4 Code Validation 59
4.1 Flow Past a Moving Sphere 60
4.2 Flow in a Cuboid Duct 62
4.3 Sphere Moving Past a Plane Wall 64
4.4 Droplet in Extension Flow 65
4.5 Droplet in a Cylindrical Capillary 66
4.6 Rising Droplet under Gravity 69
4.7 Dielectric Sphere in a Uniform Electric Field 70
4.8 Droplet in a Uniform Electric Field 71
4.9 Summary 74

II Droplet Dynamics in Microchannels **75**

5 Droplet Breakup in Constrictions **79**
5.1 Time-varying Droplet Configuration Determines Break-up Probability of Drops within a Concentrated Emulsion 80
5.2 Interaction and Breakup of Droplet Pairs in a Microchannel Y-Junction 81
5.2.1 Introduction 82
5.2.2 Problem Formulation and Methods 83
5.2.3 Results and Discussion 86
5.2.4 Conclusion 94
5.2.5 Appendix 95
5.3 Summary 96

6 Dielectrophoretic Sorting of Droplets **97**
6.1 Rational Design of a High-Throughput Droplet Sorter 98
6.1.1 Results and Discussion 101
6.1.2 Conclusions 110
6.1.3 Materials and Methods 111
6.1.4 Appendix 112
6.2 High Throughput Multiplexed Fluorescence Activated Droplet Sorting 114
6.3 Summary 117

7 Conclusions and Outlook **119**
7.1 3D Boundary Element Simulation of Droplets 119
7.2 Droplet Dynamics in Microchannels 122
7.3 Final Remarks 124

A Appendix: Jacobian, Normal and Curvature of the Smooth Surface Representation **127**
A.1 Jacobian and Normal Vector 127
A.2 Curvature 128

Bibliography **131**

Curriculum Vitae **141**

List of Figures

1.1 Strategies for pressure-driven continuous droplet creation 2
1.2 Devices for droplet sorting 4

2.1 Fundamental solution of Stokes flow around a point force 11
2.2 Stokes flow in one domain 12
2.3 Stokes flow in two domains 15
2.4 Electric field in droplet sorting 17
2.5 Domains for the electric solver 19
2.6 Young-Laplace surface stress 22
2.7 Dielectric surface stress 22
2.8 Errors of approximating the velocity in a rectangular duct 26
2.9 Accuracy of the paraboloid inlet boundary condition 27
2.10 Approximations of the downstream pressure gradient in a rectangular duct . . 28

3.1 Mesh representation with quadrilateral cells 41
3.2 Mesh refinement and hanging nodes 42
3.3 Mesh nodes on corners and edges 43
3.4 Construction of the normal vector in the smooth surface representation 44
3.5 Local surface shape in the smooth surface representation 45
3.6 Accuracy of the smooth surface representation 47
3.7 Representation of a spherical surface, at different stages of refinement 48
3.8 Quadrature formula for nearly singular integration 49
3.9 Magnitude of Stokeslet and stresslet 50
3.10 Integration accuracy for the Stokeslet 51
3.11 Integration accuracy for the stresslet 52
3.12 Loop for advancing the simulation forward in time 53
3.13 Parallelized storage of the linear system 55
3.14 Scaling of the parallelization with the number of processor cores 56

4.1 Relative error of the Stokes drag 61
4.2 Mean error of the exterior velocity field for the smooth surface representation . 62
4.3 Downstream velocity for flow in a square duct 62
4.4 Relative error of the integrated wall-normal velocity and integrated stress, for a Couette flow and the flow through a square duct 63

4.5 Geometry of a sphere that moves parallel to a plane no-slip wall 64
4.6 Drag and torque acting on a sphere 64
4.7 Steady-state shape of a droplet in an extensional flow 65
4.8 Deformation of a droplet in an extensional flow 65
4.9 Refined mesh for the steady-state droplet in a cylindrical capillary 66
4.10 Equilibrium shape of droplets in a round capillary 67
4.11 Advection velocity and fluid pressure for droplets in a round capillary 68
4.12 Flow in a droplet rising under gravity 69
4.13 Velocity of a nearly-spherical droplet rising in a gravitational field 70
4.14 Electric field lines around a sphere in a uniform field 70
4.15 Field around a dielectric sphere in a uniform electric field 71
4.16 Deformed droplet in an electric field (image) 71
4.17 Deformation of a dielectric droplet in a uniform field (graph) 72

5.1 Droplet breakup in a concentrated emulsion 80
5.2 Interaction of droplet pairs in a Y-junction 83
5.3 Design of the microfluidic device for two-droplet interaction 85
5.4 Interaction of two droplets in a Y-junction: Midplane pressure field 87
5.5 Neck formation in two droplets interacting in a Y-junction 88
5.6 Final volume of the first fragment of D_1 after pinch-off 89
5.7 Simulation results for the relation between initial droplet offset and the resulting droplet breakup 90
5.8 Experimental results for the relation between initial droplet offset and the resulting droplet breakup 91
5.9 In-plane velocity on the droplet surface 93

6.1 Genealogy of existing droplet sorter designs 99
6.2 Mechanism of dielectrophoretic sorting 100
6.3 Relative DEP force ξ around commonly used electrode designs 104
6.4 3D geometry and efficiency of a simple bar electrode 105
6.5 Sorting efficiency of a shielded electrode 106
6.6 Sorting efficiency of a pair of two active electrodes 107
6.7 Experimental droplet sorting at different electrode voltages 109
6.8 Deformation of droplets in the experiment 110
6.9 Accuracy of the approximation formula for small radii 113
6.10 Multiplexed sorting geometry in the experiment 114
6.11 Numerically predicted and experimentally observed droplet trajectories in the multiplexed sorting geometry 115
6.12 Electrode voltages for sorting of droplets with different characteristic radius R in the multiplexed sorting geometry 116

7.1 Internal flow in closely packed droplets 123
7.2 Breakup of liquid threads in a long, straight channel 124

1 Introduction

Contents

1.1 Droplet Dynamics in Microfluidics 2
1.2 Numerical Simulation Methods for Multiphase Flow 5
1.3 Structure of this Work 7

Fluid dynamics at small length scales is dominated by interfacial effects, which scale with the second power of the length. At small scales, they dominate over bulk effects that scale with the third power. Fluid systems at small scales therefore behave differently from those at larger scales. Free interfaces between immiscible fluids show particularly complex behavior. They display highly nonlinear phenomena like capillary surface waves, topological transitions such as droplet breakup and coalescence, and pattern formation in wetting and de-wetting dynamics.

The field of *droplet-based microfluidics* uses fluids with free interfaces to control material transport and mixing. Material is enclosed in fluid droplets and advected by an immiscible outer phase. With microchannel geometries on the μm-mm-scale, droplet volumes range from fractions of picoliters to several hundred nanoliters.

Due to the precise control of flows at small scales, microfluidic systems not only lay the foundation for novel applications, but also allow for detailed experimental studies of the free surface dynamics. Analytical descriptions of these systems are difficult due to the high degree of nonlinearity. Numerical tools complement experiments, as they give access to quantities of interest such as the pressure fields inside a fluid or local stresses on the interface, and allow for a precise control of parameters and models of physical effects.

This thesis makes two contributions. First, we develop a numerical 3D boundary element method to study the complex dynamics of free surface flows. This numerical tool allows us to follow the dynamic deformation of droplets in confined microfluidic systems. Second, we combine the simulation with experimental results to address two practically relevant problems: The breakup of droplets in the reinjection of concentrated emulsions, and high-throughput dielectrophoretic droplet sorting.

1.1 Droplet Dynamics in Microfluidics

Droplet based microfluidics is a key technology with numerous applications, for example in crystal synthesis (e.g. Zheng et al. [2003]; Gerdts et al. [2006]), DNA screening (e.g. Agresti et al. [2010]; Pekin et al. [2011]) or single-cell culture and analysis (e.g. Clausell-Tormos et al. [2008]; Joensson and Andersson Svahn [2012]). Whitesides [2006] gives a historic overview of microfluidic technologies. Applications exploit important features of the droplet system: Droplets have small volume, so that small quantities of proteins or DNA suffice to perform repeated experiments. In crystal synthesis, which is used to crystallize proteins for analyzing their structure, the small volume helps to control the rate of nucleation. Screening applications benefit from the high rate of throughput, facilitating the search for rare mutations. Inside biocompatible water-in-oil droplets, living cells can be cultivated under a constant supply of nutrients, which enter the droplets by diffusion through the continuous phase.

Microfluidic devices for lab-on-a-chip applications are often manufactured by soft lithography: A network of microchannels is imprinted into a silicon-based substrate and covered with a glass plate, with flexible tubings feeding the device with operating fluids. Transparent substrates allow for imaging under a microscope. Droplets act as micro-compartments, which are manipulated via the fluid flow, transported, processed or stored. Seemann et al. [2011] describe the manufacturing process of a microfluidic device, and typical approaches to droplet creation and processing. In the following we describe the key droplet manipulation steps and highlight the free-surface dynamics involved.

Creation of Droplets

The automated creation of monodisperse droplets has laid the foundations for droplet microfluidics. In static microchannel geometries and controlled purely by fixing the flow rates of the incoming droplet and continuous phase, droplets of fixed volume are created continuously and at high frequency (Ahn et al. [2006b] create 10 pL droplets at 2 kHz) through a dripping process [Plateau, 1873; Eggers, 1997]. Joensson and Andersson Svahn [2012] identify three main strategies for pressure-driven droplet generation: In coflowing droplet generation

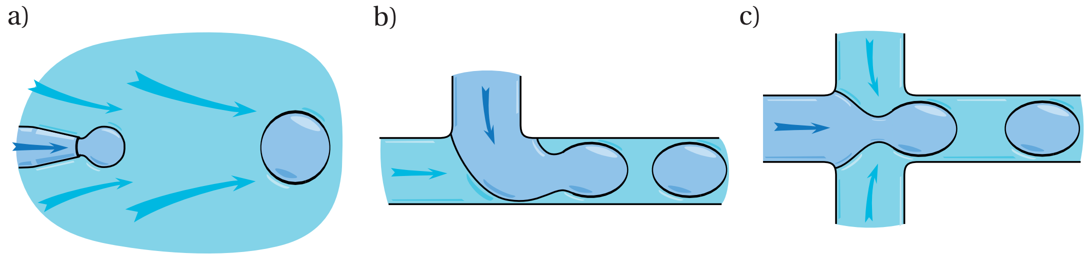

Figure 1.1: Strategies for pressure-driven continuous droplet creation. *a)* Coflowing droplet generation, after Umbanhowar et al. [2000]. *b)* Droplet generation in a T-junction, after Thorsen et al. [2001]. *c)* Droplet generation by flow focusing, after Anna et al. [2003].

(Umbanhowar et al. [2000], Figure 1.1a), droplets pinch off from the narrow tip of a capillary moving in an external flow, either inside a microfluidic device or in a large bulk volume of the external phase. A design which is easy to integrate into a microfluidic device is a T-junction (Thorsen et al. [2001], Figure 1.1b) between two rectangular channels. For higher flow rates, a flow focusing geometry (Anna et al. [2003], Figure 1.1c) is used. This symmetric setup is similar to the T-junction, but requires an additional inlet channel for the continuous phase.

Transport

The fluid transport in microfluidic devices is driven by pressure gradients. In typical setups, the inlet pressure is built up by syringe pumps outside the device, while the outlet is kept at ambient pressure. Due to the small channel cross-sections and the viscosity of the working fluids, the inlet pressure can be on the order of hundreds of kPa. The rate of flow is controlled via the inlet pumps, and flow paths can be modified using pneumatic or magnetic valves [Xi et al., 2017]. Microchannels of appropriate length and shape can promote mixing inside droplets [Tice et al., 2003], or leave sufficient time for incubation or chemical reactions (e.g. in Brosseau et al. [2014]; Zheng et al. [2003]).

Storage and Reinjection

For incubation over extended amounts of time [Pekin et al., 2011] or repeated traversal of the same microfluidic device [Agresti et al., 2010], droplets are stored outside of the microfluidic device, and later reinjected into the device. Droplet storage poses two technical challenges: Both the coalescence of droplets in dense emulsions, and their breakup during the reinjection process need to be avoided.

In typical flow conditions, droplet coalescence happens naturally when two droplet interfaces come close. Coalescence reduces the total area of the free interface, thus lowering the free energy of the droplet system [Shikhmurzaev, 2007]. To suppress the merging of droplets, the interfaces are loaded with *surfactants*, surface-active agents that accumulate on the interface and lower the surface energy. The presence of surfactants has multiple effects: First, they slow the approach of two interfaces, by suppressing drainage of the continuous phase through *Marangoni stresses* (tangential stresses on the interface due to an uneven surfactant concentration, see Stone and Leal [1990]). Then, as Bibette et al. [1999] summarize, surfactants cause various chemical and entropic repulsive forces between interfaces. The precise contribution of different stabilizing effects of surfactants depends strongly on the fluids and type of surfactant: While widely used in applications, key questions on surfactant action remain open. The distribution, adsorption and effect of surfactants on interfaces is subject of ongoing research in surface rheology and physicochemical hydrodynamics (see for example van Hunsel et al. [1986]; Stone and Leal [1990]; Song et al. [2006]; Riechers et al. [2016]). The books by Probstein [2003], Shikhmurzaev [2007] and Rosen and Kunjappu [2012] give insight into surface chemistry and modeling approaches. To coerce coalescence in surfactant-stabilized emulsions, one uses appropriate flow configurations (see for example Mazutis and Griffiths [2012]) or *electrocoalescence* (for example in Ahn et al. [2006a]).

The breakup of droplets has been studied in various flow situations, such as shear flows [Stone, 1994], extensional flows [Bentley and Leal, 1986] or junctions [Ménétrier-Deremble and Tabeling, 2006; Christopher et al., 2009; Leshansky and Pismen, 2009]. Breakup follows from a competition between viscous stresses and surface tension, quantified by the capillary number Ca. For breakup in droplet reinjection, first experimental studies were performed by Rosenfeld et al. [2014] and Gai et al. [2016a], describing breakup as a stochastic phenomenon depending on the capillary number, droplet size and ratio of viscosity between droplet and continuous phase. We recently made this description more precise, by noting that stochastic breakup behavior is limited to only a certain range of droplet configurations before entering a constriction, and deterministic for others [Khor et al., 2017].

Sorting

In specific applications such as protein screening or directed evolution (see for example Agresti et al. [2010]; Pekin et al. [2011]; Mazutis et al. [2013]; Gielen et al. [2016]), the continuous stream of droplets needs to be split up, and droplets need to be separated into different channels based on their contents. Xi et al. [2017] review the various methods that exert a force on individual droplets and move them across the stream lines of the continuous phase towards a desired microchannel entrance. One very common method for droplet sorting is the use of *dielectrophoresis* [Pohl, 1958], whereby a difference in electric polarizability between the droplet and continuous phase moves droplets towards regions of high electric field strength. Since the first dielectrophoretic sorting device by Ahn et al. [2006b], the approach has found widespread use and many designs have followed (for example by Wang et al. [2007]; Baret et al. [2009b]; Agresti et al. [2010]; Gielen et al. [2016]; Frenzel and Merten [2017], see also Figure 1.2). For picoliter-sized droplets, Sciambi and Abate [2015] reached a sorting frequency of 30 kHz, while Leman et al. [2015] were able to build a functioning sorting device for droplets at the

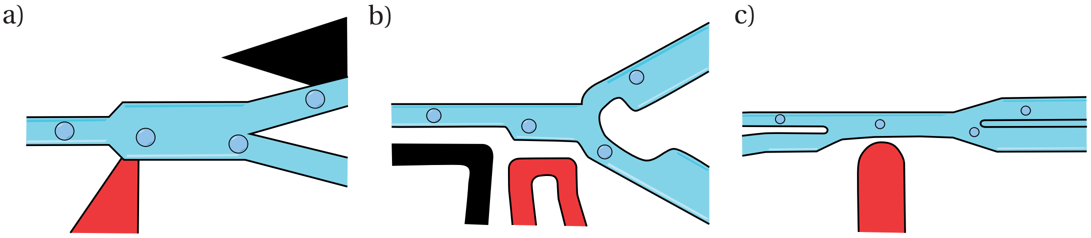

Figure 1.2: Devices for droplet sorting, with the microchannel shown in blue and active and ground electrodes in red and black. *a)* Seminal design by Ahn et al. [2006b], with electrodes in a separate layer below the microchannel. *b)* Design by Agresti et al. [2010], with electrodes and microchannel on the same level. *c)* Sorter by Sciambi and Abate [2015] for sorting at 30 kHz droplet throughput. Here, to avoid shear-induced droplet breakup, the barrier downstream from the sorter does not span the whole height of the channel.

femtoliter-scale. Electrodes in sorting devices are manufactured by the same methods as the microchannels, but filled with a conducting liquid. To avoid displacement and accumulation of ions in the working fluids, voltage of high-frequency (tens of kHz) alternating polarity is applied to the electrodes. The change in polarity does not alter the direction of force on the droplet, as the force depends on gradients in the square of the field strength.

1.2 Numerical Simulation Methods for Multiphase Flow

While the size and setup of microfluidic systems renders them accessible to optical imaging, experimental methods alone do not always provide the insight to understand droplet dynamics in sufficient detail, as quantities like the internal pressure fields or stress distributions are hard to measure. This gap in understanding is filled by numerical methods, which take mathematical models of the fundamental physical processes, and predict a system behavior which can then be compared to experimental observations. In this way, numerical methods help to design and optimize microfluidic systems, and to understand the underlying physics.

Cristini and Tan [2004] give an overview of the most common numerical simulation methods for droplet flow. A versatile numerical approach to modeling fluid flow is the *finite element method* (FEM, described for example by Gresho and Sani [1998]), which solves the flow equations in a weak form on a volumetric mesh that spans the whole fluid domain. The interface is tracked by faces of the finite-element mesh, so that the mesh must be changed at each time step [Tryggvason et al., 2001]. Interface capturing methods, such as the *volume of fluid method* [Leshansky and Pismen, 2009; Hoang et al., 2013; Chen and Yang, 2014] or the *level-set method* [Bertakis et al., 2010], do not require such a periodic re-meshing: They define an additional indicator field in the volume, which determines the location and shape of the interface. Finite-element and interface capturing methods are flexible, as they pose few constraints on the geometry of the simulation domain or the type of flow equation to solve. Topological transitions like droplet coalescence or breakup can be treated in a straightforward way. However, accurately describing the interface as part of a volume mesh requires a high mesh resolution, which carries a high computational cost that is not always justified by the typically laminar and large-scale fluid motion in the bulk.

Spectral methods [Peyret, 2000], which are widely used in other areas of computational fluid dynamics, are less suitable for simulations with free interfaces. They lack flexibility in the shape and topology of the simulation domain and adapt poorly to jump conditions on the interface.

Boundary element methods are an example of *mesh-free* methods. They allow to describe linear Stokes flow without volume forces by mapping the flow equations onto surfaces and interfaces of a geometry [Pozrikidis, 1992; Sutradhar et al., 2008; Cristini and Tan, 2004]. Since the mesh only represents the boundaries of the flow domain, where surface forces act, the dimensionality of the problem is effectively decreased by one, from 3D bulk description to 2D interfaces. Integral equations relate the flow on one point on the boundary to flows and stresses on all boundaries. Evaluating these integral equations at a finite number of points (*collocation method*, see for example Pozrikidis [1992]) or in a weak form (*Galerkin method*, for example in Sutradhar et al. [2008]) leads to a linear system of equations for the flow and stresses on the boundary. Since only the boundaries are discretized, the number of degrees of freedom is typically much smaller than for finite element methods, while the boundary is described more accurately. However, the reduction of dimensionality comes at a cost: The nonlocal coupling of the boundary integrals leads to a densely populated linear system. This contrasts finite element method and related interface capturing methods, where the coupling is local, yielding a sparse problem that scales more easily to a high number of degrees of freedom for highly resolved or complex geometries.

Numerous boundary element simulations have been designed for flow that is effectively two-dimensional, either in systems with rotational symmetry (for example Sherwood [1988]; Stone and Leal [1989b]) or flows in a shallow fluid layer (for example Dai and Shelley [1993]; Nagel and Gallaire [2015]). For full three-dimensional flow, certain simple flow geometries allow the use of special Green's functions that simplify calculations [Griggs et al., 2007; Pozrikidis, 1992]. In other cases, those simplifications are not possible. Free-surface simulations in three dimensions (as presented by Zinchenko et al. [1997]; Zinchenko and Davis [2006]; Wang and Dimitrakopoulos [2012]; Heltai et al. [2014] and many others) require a high computational effort, with particular challenges arising from determining the curvature of the free interfaces, and performing surface integrals over the boundary when the integrand is a Green's function that may diverge. With boundary element methods, topological transitions such as droplet breakup need to be explicitly modeled by the simulation scheme, for example by local re-meshing as described by Cristini et al. [2001].

In our work, we use the *collocation boundary element method*. In the geometries we want to describe, droplets are separated from each other and the microchannel walls by thin liquid films, which the boundary-based description represents well (whereas a volume mesh would require a high spatial resolution). The method allows us to accurately model surface tension and the influence of electric fields, which themselves can be calculated by boundary-element integration. By evaluating the boundary integrals at collocation points, we calculate the velocity right at the mesh vertices, where we deform the droplet mesh. A coupling between an electric boundary-element solver and a solver for the flow field has previously been presented by House [2012] for single-phase flow with solid conducting particles. We however simulate multi-phase flow, and determine the electric field in both fluid phases.

1.3 Structure of this Work

After this introduction, we continue with the mathematical description of droplet flow and electrostatics (Chapter 2), which will lay the basis for our work. This thesis makes two core contributions, which are the development of a coupled electric/flow solver for 3D flow in confined geometries, and its application to two relevant applications in droplet flow. The results are presented in two parts:

In **Part I**, we describe the implementation and validation of a boundary element method for 3D Stokes flow. In Chapter 3, we derive the discretized boundary integral equations and explain their implementation. The validation of correctness and accuracy of the numerical code is discussed in Chapter 4.

In **Part II**, we apply the numerical scheme to two research problems in droplet flow. In Chapter 5, we analyze the mechanism for the breakup of droplets in constricting microchannels, which is relevant in droplet reinjection. Dielectrophoretic droplet sorting and microchannel design principles for high sorting throughput are discussed in Chapter 6.

The thesis concludes with a summary and outlook in Chapter 7.

2 Theory / Mathematical Model

Contents

2.1 Boundary Integral Formulation for Stokes Flow 10
  2.1.1 Fundamental Solution of Stokes Flow 11
  2.1.2 Boundary Integral Equation for Stokes Flow 12
  2.1.3 Boundary Conditions 14
  2.1.4 Boundary Integral Equations with a Fluid Interface 14
2.2 Boundary Integral Formulation for Electrostatics 17
  2.2.1 Boundary Integral Equation for Electrostatics 17
  2.2.2 Boundary Integral Equations with a Dielectric Interface 19
2.3 Surface Stress Models for Stokes Flow 21
  2.3.1 Young-Laplace Surface Tension Model 21
  2.3.2 Dielectric Surface Stress 22
  2.3.3 Surface Stress due to Gravity 23
2.4 Further Relevant Boundary Integrals 23
  2.4.1 Volume of a Domain 24
  2.4.2 Center of Mass 24
  2.4.3 Determine if a Point is Inside a Domain 24
2.5 Stokes Flow in a Rectangular Duct 25
  2.5.1 Series Representation for the Velocity 25
  2.5.2 Approximation by a Biparabolic Profile 26
  2.5.3 Pressure Gradient in a Rectangular Duct 27
  2.5.4 Poiseuille Flow 28
2.6 Summary 29

Having introduced the basic concept of droplet flow in microfluidic applications, we now put our focus on the mathematical description that will underlie our analysis. We use continuum models for the fluids that comprise and surround the droplets, as well as the electric fields that are employed in droplet sorting. In this chapter, we define these models and derive a formulation that will later prove useful for the numerical implementation.

In Section 2.1, we introduce the analytic description of Stokes flow. From the Stokes equations in the volume, we derive the boundary integral equations (BIEs) for Stokes flow. Section 2.2 defines the equations for electrostatics and the resulting BIE. In Section 2.3, we present the surface stress models for the free droplet interface, which couple the Stokes solution to external forces (like the Maxwell stress from the electric fields). Section 2.4 presents integral equations for computing geometrical quantities from surface integrals. Finally, in Section 2.5, we present some analytical solutions of the Stokes equation that are used as boundary conditions for flow in a microchannel, and discuss their accuracy.

2.1 Boundary Integral Formulation for Stokes Flow

The fluids in microfluidic applications are typically incompressible and Newtonian. Due to the small length scale and low flow velocities, the Reynolds number is small, and the inertial terms of the Navier-Stokes equation are negligible. Therefore, flow is described by the incompressible Stokes equations (see e.g. Pozrikidis [1992], p. 2),

$$\nabla \cdot \boldsymbol{u} = 0, \tag{2.1a}$$

$$\boldsymbol{b} + \nabla \cdot \hat{\boldsymbol{\sigma}} = \boldsymbol{0}, \tag{2.1b}$$

for the velocity field $\boldsymbol{u}$ and a pressure field p contained in the stress tensor

$$\sigma_{ij} := -p\delta_{ij} + 2\mu\epsilon_{ij}. \tag{2.2}$$

The stress tensor is the constitutive relation between the stress in the fluid and the rate of strain

$$\epsilon_{ij} := \frac{1}{2}\left(\frac{\partial u_i}{\partial x_j} + \frac{\partial u_j}{\partial x_i}\right) \tag{2.3}$$

for a Newtonian fluid. Here, μ is the dynamic viscosity of the fluid and $\boldsymbol{b}$ some body force (per unit volume) on the fluid. The Stokes equations are linear, and the absence of a local time derivative indicates that instantly adapts to its boundary conditions in space. While the first Stokes equation (2.1a) simply describes the incompressibility of the fluid (and is often omitted), the second equation (2.1b) describes a local stress balance between the internal forces of the fluid and the external body force. If we assume that no external body forces are present but gravity with $\boldsymbol{b} := -\rho g \boldsymbol{e}_z$, we can define a modified pressure $p' := p + \rho g z$ and a modified stress tensor $\sigma'_{ij} := -p'\delta_{ij} + 2\mu\epsilon_{ij}$. The stress balance (2.1b) then reads

$$\nabla \cdot \hat{\boldsymbol{\sigma}}' \;=\; \mathbf{0}. \tag{2.4}$$

In the absence of other body forces, we will later replace equation (2.1b) by the more elegant equation (2.4), keeping in mind that the equations are then based on the modified pressure p'.

2.1.1 Fundamental Solution of Stokes Flow

The Stokes flow for a singular point force at a point $\boldsymbol{x}_0$ acting in an arbitrary direction $\boldsymbol{g}$, i.e. the solution to eq. (2.1) with

$$\boldsymbol{b}(\boldsymbol{x}) = \delta(\boldsymbol{x} - \boldsymbol{x}_0)\boldsymbol{g} \tag{2.5}$$

in an unbounded fluid volume ($\lim_{|\boldsymbol{x}|\to\infty} (|\boldsymbol{u}|, p) \to (0,0)$) is [Pozrikidis, 1992, p. 22ff]

$$\boldsymbol{u}(\boldsymbol{x}) \;=\; \frac{1}{8\pi\mu}\hat{\boldsymbol{G}}(\boldsymbol{x} - \boldsymbol{x}_0)\cdot\boldsymbol{g}, \tag{2.6a}$$

$$p(\boldsymbol{x}) \;=\; \frac{1}{8\pi}\boldsymbol{p}(\boldsymbol{x} - \boldsymbol{x}_0)\cdot\boldsymbol{g}. \tag{2.6b}$$

We call the flow field $\boldsymbol{u}$ (and associated pressure p) the *fundamental solution* of the 3D Stokes flow. The tensor

$$G_{ij}(\boldsymbol{r}) \;:=\; \frac{\delta_{ij}}{|\boldsymbol{r}|} + \frac{r_i r_j}{|\boldsymbol{r}|^3}, \tag{2.7}$$

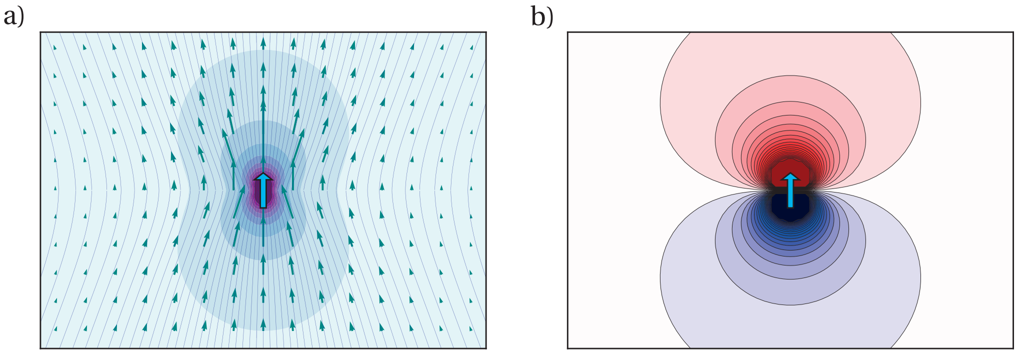

Figure 2.1: Fundamental solution of Stokes flow around a point force. The blue arrow at $\boldsymbol{x}_0$ marks the direction $\boldsymbol{g}$ of the point force. *a)* Velocity field of the fundamental solution, eq. (2.6a). The background color shows the speed $|\boldsymbol{u}|$. *b)* Pressure field of the fundamental solution, eq. (2.6b).

which describes the linear relationship between the arbitrary point force vector $\boldsymbol{g}$ and the solution $\boldsymbol{u}$, is called the *Stokeslet* or *free-space Green's function* for the velocity. Accordingly, the relation between force and pressure is described by the *pressurelet*

$$\boldsymbol{p}(\boldsymbol{r}) := \frac{2\boldsymbol{r}}{|\boldsymbol{r}|^3}. \tag{2.8}$$

The velocity and pressure fields of the fundamental solution are shown in Figure 2.1. Both have a singularity for $\boldsymbol{x} \to \boldsymbol{x}_0$, which goes with $\frac{1}{|\boldsymbol{r}|}$ for the velocity and $\frac{1}{|\boldsymbol{r}|^2}$ for the pressure. With the fundamental solution $\boldsymbol{u}(\boldsymbol{x})$ as in eq. (2.6a), the stress tensor has the form

$$\hat{\boldsymbol{\sigma}}(\boldsymbol{x}) = \frac{1}{8\pi}\hat{\boldsymbol{T}}(\boldsymbol{x}-\boldsymbol{x}_0)\cdot\boldsymbol{g} \tag{2.9}$$

with a rank-3 tensor

$$T_{ijk}(\boldsymbol{r}) := -6\frac{r_i r_j r_k}{|\boldsymbol{r}|^5}. \tag{2.10}$$

This tensor, called the *stresslet*, describes the linear relationship between a point force of strength $\boldsymbol{g}$ at a point $\boldsymbol{x}_0$, and the stress tensor $\hat{\boldsymbol{\sigma}}$ at point $\boldsymbol{x}$.

Any body force distribution $\boldsymbol{b}(\boldsymbol{x}_0)$ can be represented by a superposition of point forces of appropriate strength and direction. Since the Stokes equations are linear, the solution for $\boldsymbol{u}$ and p can be constructed by superimposing the fundamental solutions via a convolution integral over $\boldsymbol{x}_0$. In particular, when the interior of some domain $\Omega \subset \mathbb{R}^3$ is free of volume forces, the velocity field $\boldsymbol{u}$ in this domain is uniquely defined by the forces on the domain boundaries $\partial\Omega$, such that the 3D convolution reduces to a 2D surface integral. This simplification is encoded in the *Boundary Integral Equation*.

2.1.2 Boundary Integral Equation for Stokes Flow

Let $\boldsymbol{u}$ and $\boldsymbol{u}'$ be two different regular flow fields satisfying the Stokes equations (2.1) on a domain Ω, with $\hat{\boldsymbol{\sigma}}$ and $\hat{\boldsymbol{\sigma}}'$ their respective stress tensors. Then,

$$\nabla\cdot\left(\boldsymbol{u}'\cdot\hat{\boldsymbol{\sigma}} - \boldsymbol{u}\cdot\hat{\boldsymbol{\sigma}}'\right) = 0. \tag{2.11}$$

This relation is called the *Lorentz identity* or *Lorentz reciprocal relation* (after Lorentz [1907]).[1] Choosing $\boldsymbol{u}'$ to be the fundamental solution (2.6a) with an arbitrary point force $\boldsymbol{g}$ at $\boldsymbol{x}_0$, we get

$$\nabla\cdot\left[\frac{1}{8\pi\mu}\hat{\boldsymbol{G}}(\boldsymbol{x}-\boldsymbol{x}_0)\cdot\hat{\boldsymbol{\sigma}}(\boldsymbol{x}) - \frac{1}{8\pi}\boldsymbol{u}(\boldsymbol{x})\cdot\hat{\boldsymbol{T}}(\boldsymbol{x}-\boldsymbol{x}_0)\right] = \boldsymbol{0} \tag{2.12}$$

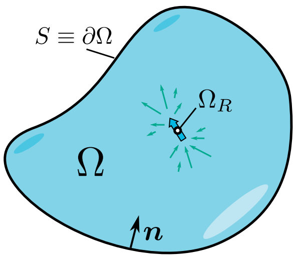

Figure 2.2: Stokes flow in the domain Ω. For a point force $\boldsymbol{g}$ at $\boldsymbol{x}_0 \in \Omega$, a spherical domain Ω_R is excluded from the volume integral.

---

[1] The Lorentz identity also holds for the equations (2.4) with the modified pressure p' that accounts for gravity.

on the domain $\Omega \setminus \Omega_R$, with Ω_R a sphere of radius R around $\boldsymbol{x}_0$ to avoid the singularity of $\boldsymbol{u}'$ at $\boldsymbol{x}_0$. Note that eq. (2.12) does not depend on $\boldsymbol{g}$. We integrate (2.12) over the domain $\Omega \setminus \Omega_R$ and use the divergence theorem

$$\int_{\Omega} \nabla \cdot \boldsymbol{F} \, \mathrm{d}^3\boldsymbol{x} = -\int_{\partial\Omega} \boldsymbol{F} \cdot \boldsymbol{n} \, \mathrm{d}^2\boldsymbol{x}, \tag{2.13}$$

(which holds for any continuously differentiable vector field $\boldsymbol{F}$ and smooth surface $\partial\Omega$ of a domain Ω) to get the relation

$$\int_{\partial(\Omega\setminus\Omega_R)} \left[\frac{1}{8\pi\mu} \hat{\boldsymbol{G}}(\boldsymbol{x}-\boldsymbol{x}_0) \cdot \hat{\boldsymbol{\sigma}}(\boldsymbol{x}) - \frac{1}{8\pi} \boldsymbol{u}(\boldsymbol{x}) \cdot \hat{\boldsymbol{T}}(\boldsymbol{x}-\boldsymbol{x}_0) \right] \boldsymbol{n}(\boldsymbol{x}) \, \mathrm{d}^2\boldsymbol{x} = \boldsymbol{0},$$

where $\boldsymbol{n}$ is the surface normal pointing into the volume (as in Figure 2.2). For $R \to 0$ we find (see also Pozrikidis [1992], p. 20f)

$$\lim_{R\to 0} \int_{\partial\Omega_R} \frac{1}{8\pi\mu} \hat{\boldsymbol{G}}(\boldsymbol{x}-\boldsymbol{x}_0) \cdot \hat{\boldsymbol{\sigma}}(\boldsymbol{x}) \boldsymbol{n}(\boldsymbol{x}) \, \mathrm{d}^2\boldsymbol{x} = \boldsymbol{0}$$

and

$$\lim_{R\to 0} \int_{\partial\Omega_R} \frac{1}{8\pi} \boldsymbol{u}(\boldsymbol{x}) \cdot \hat{\boldsymbol{T}}(\boldsymbol{x}-\boldsymbol{x}_0) \boldsymbol{n}(\boldsymbol{x}) \, \mathrm{d}^2\boldsymbol{x} = \begin{cases} -\boldsymbol{u}(\boldsymbol{x}_0) & \boldsymbol{x}_0 \in \Omega \setminus \partial\Omega \\ -\frac{\boldsymbol{u}(\boldsymbol{x}_0)}{2} & \boldsymbol{x}_0 \in \partial\Omega \\ \boldsymbol{0} & \boldsymbol{x}_0 \notin \Omega. \end{cases} \tag{2.14}$$

Thus, for any point $\boldsymbol{x}_0$ inside the domain Ω, we have

$$\boldsymbol{u}(\boldsymbol{x}_0) = -\frac{1}{8\pi\mu} \int_S \hat{\boldsymbol{G}}(\boldsymbol{x}-\boldsymbol{x}_0) \cdot \boldsymbol{f}(\boldsymbol{x}) \, \mathrm{d}^2\boldsymbol{x} + \frac{1}{8\pi} \int_S \boldsymbol{u}(\boldsymbol{x}) \cdot \hat{\boldsymbol{T}}(\boldsymbol{x}-\boldsymbol{x}_0) \cdot \boldsymbol{n} \, \mathrm{d}^2\boldsymbol{x} \tag{2.15}$$

with $S := \partial\Omega$ and the *surface stress* $\boldsymbol{f} := \hat{\boldsymbol{\sigma}} \cdot \boldsymbol{n}$. This equation, which relates the flow field in the fluid volume to the flow velocity and stresses on the surface S, is the *Boundary Integral Equation* (BIE) for 3D Stokes flow. Note that by using the Lorentz reciprocal relation, the roles of the source of the flow and the location of observation have been exchanged; now the sources sit on the boundary described by $\boldsymbol{x}$, and velocity is observed at $\boldsymbol{x}_0$ in the force-free interior of the volume.

If $\boldsymbol{x}_0$ is on the boundary S, we get

$$\frac{1}{2}\boldsymbol{u}(\boldsymbol{x}_0) = -\frac{1}{8\pi\mu} \int_S \hat{\boldsymbol{G}}(\boldsymbol{x}-\boldsymbol{x}_0) \cdot \boldsymbol{f}(\boldsymbol{x}) \, \mathrm{d}^2\boldsymbol{x} + \frac{1}{8\pi} \int_S^{PV} \boldsymbol{u}(\boldsymbol{x}) \cdot \hat{\boldsymbol{T}}(\boldsymbol{x}-\boldsymbol{x}_0) \cdot \boldsymbol{n} \, \mathrm{d}^2\boldsymbol{x}. \tag{2.16}$$

With $\boldsymbol{x}_0$ on the boundary, the Green's functions diverge for $\boldsymbol{x} \to \boldsymbol{x}_0$. However, the integrals exist and are finite if the integral over $\boldsymbol{u}$ is evaluated in a principal-value sense (i.e. excluding a circle of infinitesimal radius centered at the singularity). The factor $\frac{1}{2}$ is the fraction of solid angle around $\boldsymbol{x}_0$ that is inside Ω, for non-smooth boundaries (like corners or edges) the factor changes accordingly.

The BIE (2.16) for $\boldsymbol{x}_0$ on S provides a complete description of the flow in the volume Ω and is the basis for the Boundary Element Method (BEM). For any combination $\boldsymbol{f}$ and $\boldsymbol{u}$ on the boundary satisfying (2.16), equation (2.15) is used to determine the flow field anywhere in the domain.

Outside the domain Ω, evaluating the BIE gives

$$\mathbf{0} = -\frac{1}{8\pi\mu}\int_S \hat{\boldsymbol{G}}(\boldsymbol{x}-\boldsymbol{x}_0)\cdot\boldsymbol{f}(\boldsymbol{x})\,\mathrm{d}^2\boldsymbol{x} + \frac{1}{8\pi}\int_S \boldsymbol{u}(\boldsymbol{x})\cdot\hat{\boldsymbol{T}}(\boldsymbol{x}-\boldsymbol{x}_0)\cdot\boldsymbol{n}\,\mathrm{d}^2\boldsymbol{x}. \tag{2.17}$$

We will use this property of the Boundary Integral Equation for deriving an expression for the flow on both sides of an interface between two fluids.

2.1.3 Boundary Conditions

We typically consider four types of boundary conditions on the surface S:

- **Dirichlet** conditions, where $\boldsymbol{u}$ is specified on S, but the stress $\boldsymbol{f}$ is unknown and determined by solving the BIE. Typical situations are fixed side walls of the geometry, where $\boldsymbol{u} \equiv \mathbf{0}$ describes a no-slip boundary, or the inlet of some microchannel, where the velocity profile $\boldsymbol{u}_0(\boldsymbol{x})$ is prescribed.
- **Neumann** conditions, where the stress $\boldsymbol{f}$ is prescribed on S, and $\boldsymbol{u}$ unknown.
- **Outlet** conditions, where the wall-normal stress $\boldsymbol{f}\cdot\boldsymbol{n}$ and the tangential velocity $\boldsymbol{u}\cdot\boldsymbol{t}_i$ (for two linearly independent tangent vectors $\boldsymbol{t}_i$) are each set to zero. This sets the pressure on the outlet plane to zero, and allows for a flow normal to the outlet plane.
- **Interface** conditions, where velocity and stress on an interface are coupled to the solution in another domain. We discuss this situation in Section 2.1.4.

Different boundary conditions can be prescribed on different parts of the boundary. If we were to set Dirichlet boundary conditions on all boundaries, $\boldsymbol{f}$ would be determined only up to an arbitrary scalar constant pressure p_0 in wall-normal direction. We avoid this situation by always prescribing the pressure on at least part of the boundary.

2.1.4 Boundary Integral Equations with a Fluid Interface

The Boundary Integral Equation (2.16) provides an elegant description of Stokes flow in systems where either the flow velocity or stress is known on the domain boundary. However, when a fluid is bounded by a freely deformable interface with another fluid, neither the total stress nor the interface velocity is generally known on that interface: The two flows are coupled by the interface and need to be considered together. In deriving the description for a coupled flow with a free interface, we follow the description by Pozrikidis [1992].

Consider two Newtonian fluids of viscosity μ_1 and μ_2 in domains Ω_1 and Ω_2 with a common interface S. We assume no-slip boundary conditions, so the flow velocity is continuous across the interface,

$$\boldsymbol{u}^{(1)}(\boldsymbol{x}) \;=\; \boldsymbol{u}^{(2)}(\boldsymbol{x}) \tag{2.18}$$

for $\boldsymbol{x} \in S$. The stresses $\boldsymbol{f}^{(i)} := \hat{\boldsymbol{\sigma}}^{(i)} \cdot \boldsymbol{n}$, where $\boldsymbol{n}$ is the normal vector pointing into Ω_1, are coupled by the relation

$$\Delta \boldsymbol{f}(\boldsymbol{x}) \;:=\; \boldsymbol{f}^{(2)}(\boldsymbol{x}) - \boldsymbol{f}^{(1)}(\boldsymbol{x}), \tag{2.19}$$

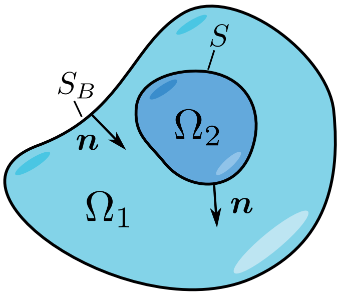

Figure 2.3: Stokes flow in the domain Ω_2, which is enclosed by another flow domain Ω_1.

where $\Delta \boldsymbol{f}(\boldsymbol{x})$ is the stress of the interface on the fluid. This net stress is due to local effects like surface tension, which are known. We discuss relevant models for the interface stress in Section 2.3.

Now let fluid (2) be a droplet fully enclosed by fluid (1) (i.e. $\partial\Omega_2 = S$), and fluid (1) a continuous phase fully enclosed by some fixed external boundary S_B ($\partial\Omega_1 = S \cup S_B$, see Figure 2.3). For $\boldsymbol{x}_0 \in \Omega_1$, the flow is described by the BIEs (2.15) and (2.17),

$$\boldsymbol{u}^{(1)}(\boldsymbol{x}_0) = -\frac{1}{8\pi\mu_1} \int\limits_{S\cup S_B} \hat{\boldsymbol{G}}(\boldsymbol{x}-\boldsymbol{x}_0)\cdot \boldsymbol{f}^{(1)}(\boldsymbol{x})\,\mathrm{d}^2\boldsymbol{x} + \frac{1}{8\pi} \overset{PV}{\int\limits_{S\cup S_B}} \boldsymbol{u}^{(1)}(\boldsymbol{x})\cdot \hat{\boldsymbol{T}}(\boldsymbol{x}-\boldsymbol{x}_0)\cdot \boldsymbol{n}\,\mathrm{d}^2\boldsymbol{x}, \tag{2.20a}$$

$$\boldsymbol{0} = \frac{1}{8\pi\mu_2} \int\limits_{S} \hat{\boldsymbol{G}}(\boldsymbol{x}-\boldsymbol{x}_0)\cdot \boldsymbol{f}^{(2)}(\boldsymbol{x})\,\mathrm{d}^2\boldsymbol{x} - \frac{1}{8\pi} \overset{PV}{\int\limits_{S}} \boldsymbol{u}^{(2)}(\boldsymbol{x})\cdot \hat{\boldsymbol{T}}(\boldsymbol{x}-\boldsymbol{x}_0)\cdot \boldsymbol{n}\,\mathrm{d}^2\boldsymbol{x}, \tag{2.20b}$$

where the signs in the second equation are flipped to respect the definition of the normal vector on S. With $\lambda := \frac{\mu_2}{\mu_1}$ the viscosity ratio, adding (2.20a)+$\lambda\cdot$(2.20b) gives

$$\begin{aligned}\boldsymbol{u}(\boldsymbol{x}_0) \;=\; &-\frac{1}{8\pi\mu_1} \int\limits_{S_B} \hat{\boldsymbol{G}}(\boldsymbol{x}-\boldsymbol{x}_0)\cdot \boldsymbol{f}(\boldsymbol{x})\,\mathrm{d}^2\boldsymbol{x} + \frac{1}{8\pi} \int\limits_{S_B} \boldsymbol{u}(\boldsymbol{x})\cdot \hat{\boldsymbol{T}}(\boldsymbol{x}-\boldsymbol{x}_0)\cdot \boldsymbol{n}\,\mathrm{d}^2\boldsymbol{x} \\ &+ \frac{1}{8\pi\mu_1} \int\limits_{S} \hat{\boldsymbol{G}}(\boldsymbol{x}-\boldsymbol{x}_0)\cdot \Delta\boldsymbol{f}(\boldsymbol{x})\,\mathrm{d}^2\boldsymbol{x} + \frac{1-\lambda}{8\pi} \int\limits_{S} \boldsymbol{u}(\boldsymbol{x})\cdot \hat{\boldsymbol{T}}(\boldsymbol{x}-\boldsymbol{x}_0)\cdot \boldsymbol{n}\,\mathrm{d}^2\boldsymbol{x}\end{aligned} \tag{2.21}$$

for the flow field in the continuous phase, $\boldsymbol{x}_0 \in \Omega_1$. Here the markers $^{(1)}$ and $^{(2)}$ have been dropped, $\boldsymbol{u}$ refers to $\boldsymbol{u}^{(i)}$ in Ω_i, and the boundary stress $\boldsymbol{f}$ on S_B is $\boldsymbol{f}^{(1)}$. In the same fashion as before, the bulk flow inside the droplet, $\boldsymbol{x}_0 \in \Omega_2$, is determined by the relation

$$\begin{aligned}\lambda\boldsymbol{u}(\boldsymbol{x}_0) \;=\; &-\frac{1}{8\pi\mu_1} \int\limits_{S_B} \hat{\boldsymbol{G}}(\boldsymbol{x}-\boldsymbol{x}_0)\cdot \boldsymbol{f}(\boldsymbol{x})\,\mathrm{d}^2\boldsymbol{x} + \frac{1}{8\pi} \int\limits_{S_B} \boldsymbol{u}(\boldsymbol{x})\cdot \hat{\boldsymbol{T}}(\boldsymbol{x}-\boldsymbol{x}_0)\cdot \boldsymbol{n}\,\mathrm{d}^2\boldsymbol{x} \\ &+ \frac{1}{8\pi\mu_1} \int\limits_{S} \hat{\boldsymbol{G}}(\boldsymbol{x}-\boldsymbol{x}_0)\cdot \Delta\boldsymbol{f}(\boldsymbol{x})\,\mathrm{d}^2\boldsymbol{x} + \frac{1-\lambda}{8\pi} \int\limits_{S} \boldsymbol{u}(\boldsymbol{x})\cdot \hat{\boldsymbol{T}}(\boldsymbol{x}-\boldsymbol{x}_0)\cdot \boldsymbol{n}\,\mathrm{d}^2\boldsymbol{x}.\end{aligned} \tag{2.22}$$

Similar relations hold for $\boldsymbol{x}_0$ on the boundaries. For $\boldsymbol{x}_0 \in S$, we have

$$\begin{aligned}\frac{1+\lambda}{2}\boldsymbol{u}(\boldsymbol{x}_0) \;=\; & -\frac{1}{8\pi\mu_1}\int\limits_{S_B}\hat{\boldsymbol{G}}(\boldsymbol{x}-\boldsymbol{x}_0)\cdot\boldsymbol{f}(\boldsymbol{x})\,\mathrm{d}^2\boldsymbol{x} + \frac{1}{8\pi}\int\limits_{S_B}\boldsymbol{u}(\boldsymbol{x})\cdot\hat{\boldsymbol{T}}(\boldsymbol{x}-\boldsymbol{x}_0)\cdot\boldsymbol{n}\,\mathrm{d}^2\boldsymbol{x} \\ & +\frac{1}{8\pi\mu_1}\int\limits_{S}\hat{\boldsymbol{G}}(\boldsymbol{x}-\boldsymbol{x}_0)\cdot\Delta\boldsymbol{f}(\boldsymbol{x})\,\mathrm{d}^2\boldsymbol{x} + \frac{1-\lambda}{8\pi}\int\limits_{S}\boldsymbol{u}(\boldsymbol{x})\cdot\hat{\boldsymbol{T}}(\boldsymbol{x}-\boldsymbol{x}_0)\cdot\boldsymbol{n}\,\mathrm{d}^2\boldsymbol{x}. \qquad (2.23)\end{aligned}$$

For $\boldsymbol{x}_0 \in S_B$, we have

$$\begin{aligned}\frac{1}{2}\boldsymbol{u}(\boldsymbol{x}_0) \;=\; & -\frac{1}{8\pi\mu_1}\int\limits_{S_B}\hat{\boldsymbol{G}}(\boldsymbol{x}-\boldsymbol{x}_0)\cdot\boldsymbol{f}(\boldsymbol{x})\,\mathrm{d}^2\boldsymbol{x} + \frac{1}{8\pi}\int\limits_{S_B}\boldsymbol{u}(\boldsymbol{x})\cdot\hat{\boldsymbol{T}}(\boldsymbol{x}-\boldsymbol{x}_0)\cdot\boldsymbol{n}\,\mathrm{d}^2\boldsymbol{x} \\ & +\frac{1}{8\pi\mu_1}\int\limits_{S}\hat{\boldsymbol{G}}(\boldsymbol{x}-\boldsymbol{x}_0)\cdot\Delta\boldsymbol{f}(\boldsymbol{x})\,\mathrm{d}^2\boldsymbol{x} + \frac{1-\lambda}{8\pi}\int\limits_{S}\boldsymbol{u}(\boldsymbol{x})\cdot\hat{\boldsymbol{T}}(\boldsymbol{x}-\boldsymbol{x}_0)\cdot\boldsymbol{n}\,\mathrm{d}^2\boldsymbol{x}. \qquad (2.24)\end{aligned}$$

Equations (2.21)-(2.24) are the *Boundary Integral Equations for Droplet Flow.* In the numerical Boundary Element Method, we use the relations for $\boldsymbol{x}_0$ on the boundary, eq. (2.23) and (2.24), to find the combination of velocities on $S \cup S_B$ and stresses on S_B that satisfies the Stokes equations. From there, we use the bulk equations (2.21) and (2.22) to determine the velocity at any point inside the domain.

Expressing the flow with just one BIE — instead of two BIEs for the two fluids — means that the values for the stress $\boldsymbol{f}^{(i)}$ on S remain unknown (just their difference $\Delta\boldsymbol{f}$ is computed). In the applications considered here, the values have no relevance for the dynamics. If need be, they could be computed by solving another BIE on domain Ω_1.

Boundary Integral Equation for the Bulk Pressure

Besides the velocity field in the domains Ω_1 and Ω_2, we also want to determine the bulk pressure $p(\boldsymbol{x}_0)$. With the pressurelet $\boldsymbol{p}(\boldsymbol{r}) = \frac{2\boldsymbol{r}}{|\boldsymbol{r}|^5}$ (eq. 2.8) and associated stress tensor $\hat{\boldsymbol{P}} := 2\nabla\boldsymbol{p}$ with

$$P_{ij}(\boldsymbol{r}) \;=\; 4\left(-\frac{\delta_{ij}}{|\boldsymbol{r}|^3}+3\frac{r_i r_j}{|\boldsymbol{r}|^5}\right), \qquad (2.25)$$

the bulk pressure is described by the BIE [Pozrikidis, 2011, p. 463f]

$$\begin{aligned}p(\boldsymbol{x}_0) \;=\; & -\frac{1}{8\pi}\int\limits_{S_B}\boldsymbol{p}(\boldsymbol{x}-\boldsymbol{x}_0)\cdot\boldsymbol{f}(\boldsymbol{x})\,\mathrm{d}^2\boldsymbol{x} + \frac{\mu_1}{8\pi}\int\limits_{S_B}\boldsymbol{u}(\boldsymbol{x})\cdot\hat{\boldsymbol{P}}(\boldsymbol{x}-\boldsymbol{x}_0)\cdot\boldsymbol{n}\,\mathrm{d}^2\boldsymbol{x} \\ & +\frac{1}{8\pi}\int\limits_{S}\boldsymbol{p}(\boldsymbol{x}-\boldsymbol{x}_0)\cdot\Delta\boldsymbol{f}(\boldsymbol{x})\,\mathrm{d}^2\boldsymbol{x} + \frac{(1-\lambda)\mu_1}{8\pi}\int\limits_{S}\boldsymbol{u}(\boldsymbol{x})\cdot\hat{\boldsymbol{P}}(\boldsymbol{x}-\boldsymbol{x}_0)\cdot\boldsymbol{n}\,\mathrm{d}^2\boldsymbol{x} \qquad (2.26)\end{aligned}$$

both for $\boldsymbol{x}_0 \in \Omega_1$ and for $\boldsymbol{x}_0 \in \Omega_2$.

2.2 Boundary Integral Formulation for Electrostatics

To calculate the dielectric surface stress in droplet sorting, the electric field needs to be known on the droplet surface. The electric field propagates on time scales much faster than the fluid motion,so that electrostatics provides an accurate description of the electric effects.

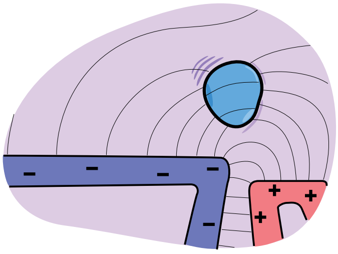

Figure 2.4: To simulate droplet sorting, the electric field around the droplet must be known.

Consider a homogeneous, non-conducting, linear and isotropic dielectric medium of electric susceptibility χ in an electric field $\boldsymbol{E}$. Such a dielectric shows a polarization of [Landau et al., 1984, p. 34ff]

$$\boldsymbol{P} = \varepsilon_0 \chi \boldsymbol{E}, \tag{2.27}$$

where $\varepsilon_0 = 8.854 \cdot 10^{-12}\mathrm{F/m}$ is the *vacuum permittivity*. Electric field and polarization add up to the *displacement field*

$$\boldsymbol{D} := \varepsilon_0 \boldsymbol{E} + \boldsymbol{P} = \varepsilon_0 \varepsilon_r \boldsymbol{E}, \tag{2.28}$$

with the *relative permittivity* $\varepsilon_r := 1 + \chi$. In the dielectric medium, the electric field follows Gauss's law

$$\nabla \cdot \boldsymbol{E} = \frac{\rho}{\varepsilon_0 \varepsilon_r}, \tag{2.29}$$

with ρ the free charge density. In electrostatics, the electric field is irrotational ($\nabla \times \boldsymbol{E} = \boldsymbol{0}$) and can be expressed by the gradient of the electric potential φ,

$$\boldsymbol{E} = -\nabla \varphi. \tag{2.30}$$

In the absence of free charges ($\rho \equiv 0$), the potential φ satisfies the Laplace equation

$$\Delta \varphi = 0. \tag{2.31}$$

As the fluid volume is charge free, and charges are only present on the droplet interface and electrodes, the electric field can be described by a boundary integral equation.

2.2.1 Boundary Integral Equation for Electrostatics

The fundamental solution of electrostatics, i.e. the electric field around a point charge ρ_0 at point $\boldsymbol{x}_0$, $\rho(\boldsymbol{x}) = \delta(\boldsymbol{x} - \boldsymbol{x}_0)\rho_0$, is

$$\varphi(\boldsymbol{x}) = G(\boldsymbol{x} - \boldsymbol{x}_0)\frac{\rho_0}{\varepsilon_0 \varepsilon_r}, \tag{2.32}$$

with the Green's function

$$G(\boldsymbol{r}) \;:=\; \frac{1}{4\pi|\boldsymbol{r}|}. \tag{2.33}$$

Much like in the case of Stokes flow (Section 2.1.2), any two solutions φ, ψ of Laplace's equation (2.31) on domain Ω satisfy

$$\nabla\cdot\left(\varphi\nabla\psi-\psi\nabla\varphi\right) \;=\; 0. \tag{2.34}$$

Like in Section 2.1.2, we choose ψ as the fundamental solution (2.32), integrate over domain $\Omega\setminus\Omega_R$ (with Ω_R a sphere of radius R around $\boldsymbol{x}_0$), and use the divergence theorem to write the volume integral as a surface integral,

$$0 \;=\; \int_{\partial(\Omega\setminus\Omega_R)}\left[\varphi(\boldsymbol{x})T_{\boldsymbol{n}}(\boldsymbol{x}-\boldsymbol{x}_0)+E_{\boldsymbol{n}}(\boldsymbol{x})G(\boldsymbol{x}-\boldsymbol{x}_0)\right]\,\mathrm{d}^2\boldsymbol{x}, \tag{2.35}$$

with

$$T_{\boldsymbol{n}}(\boldsymbol{r}) \;:=\; (\nabla G(\boldsymbol{r}))\cdot\boldsymbol{n} \;=\; -\frac{\boldsymbol{r}\cdot\boldsymbol{n}}{4\pi|\boldsymbol{r}|^3}, \tag{2.36a}$$

$$E_{\boldsymbol{n}}(\boldsymbol{x}) \;:=\; -(\nabla\varphi(\boldsymbol{x}))\cdot\boldsymbol{n}, \tag{2.36b}$$

and $\boldsymbol{n}$ the normal vector at $\boldsymbol{x}$ pointing into the volume. Just like the Stokes flow is described by the surface velocity $\boldsymbol{u}$ and surface stress $\boldsymbol{f}$, the electric field is determined by the potential φ on the surfaces, and the wall-normal field $E_{\boldsymbol{n}}$. For $\boldsymbol{x}_0\in\Omega\setminus\partial\Omega$, the limit process $R\to 0$ yields the BIE

$$\varphi(\boldsymbol{x}_0) \;=\; \int_S\left[\varphi(\boldsymbol{x})T_{\boldsymbol{n}}(\boldsymbol{x}-\boldsymbol{x}_0)+E_{\boldsymbol{n}}(\boldsymbol{x})G(\boldsymbol{x}-\boldsymbol{x}_0)\right]\,\mathrm{d}^2\boldsymbol{x}, \tag{2.37}$$

with $S:=\partial\Omega$. For $\boldsymbol{x}_0\notin\Omega$, we get

$$0 \;=\; \int_S\left[\varphi(\boldsymbol{x})T_{\boldsymbol{n}}(\boldsymbol{x}-\boldsymbol{x}_0)+E_{\boldsymbol{n}}(\boldsymbol{x})G(\boldsymbol{x}-\boldsymbol{x}_0)\right]\,\mathrm{d}^2\boldsymbol{x}. \tag{2.38}$$

For $\boldsymbol{x}_0$ on the boundary S, and S smooth, we get

$$\frac{1}{2}\varphi(\boldsymbol{x}_0) \;=\; \int_S^{PV}\left[\varphi(\boldsymbol{x})T_{\boldsymbol{n}}(\boldsymbol{x}-\boldsymbol{x}_0)+E_{\boldsymbol{n}}(\boldsymbol{x})G(\boldsymbol{x}-\boldsymbol{x}_0)\right]\,\mathrm{d}^2\boldsymbol{x}. \tag{2.39}$$

We use the BIE for $\boldsymbol{x}_0\in S$ (eq. 2.39) to find appropriate values for φ and $E_{\boldsymbol{n}}$ on the boundary that satisfy the Laplace equation (2.31). From there, we determine the potential in the interior of the domain via equation (2.37).

Electric Field in the Volume

From the BIE for the potential $\varphi(\boldsymbol{x}_0)$ for $\boldsymbol{x}_0 \in \Omega$ (eq. 2.37), we derive an expression for the electric field $\boldsymbol{E}(\boldsymbol{x}_0)$ by using the relation $\boldsymbol{E} = -\nabla\varphi$ (eq. 2.30). Pulling the gradient into the integral, we get

$$\boldsymbol{E}(\boldsymbol{x}_0) \;=\; -\nabla\varphi(\boldsymbol{x}_0) \;=\; \int_S \left[\varphi(\boldsymbol{x})\boldsymbol{\Pi}_{\boldsymbol{n}}(\boldsymbol{x}-\boldsymbol{x}_0) + E_{\boldsymbol{n}}(\boldsymbol{x})\boldsymbol{T}(\boldsymbol{x}-\boldsymbol{x}_0)\right]\,\mathrm{d}^2\boldsymbol{x}, \tag{2.40}$$

with functions

$$\boldsymbol{T}(\boldsymbol{r}) \;:=\; \nabla G(\boldsymbol{r}) \;=\; -\frac{\boldsymbol{r}}{4\pi|\boldsymbol{r}|^3}, \tag{2.41a}$$

$$\boldsymbol{\Pi}_{\boldsymbol{n}}(\boldsymbol{r}) \;:=\; \nabla T_{\boldsymbol{n}}(\boldsymbol{r}) \;=\; \frac{1}{4\pi|\boldsymbol{r}|^3}\left(\frac{3(\boldsymbol{r}\cdot\boldsymbol{n})\boldsymbol{r}}{|\boldsymbol{r}|^2} - \boldsymbol{n}\right). \tag{2.41b}$$

2.2.2 Boundary Integral Equations with a Dielectric Interface

After deriving an expression for the field in a single domain of an ideal dielectric medium, we now derive a description for two dielectrics of different permittivity, which share a common interface. Consider two homogeneous, non-conducting, linear and isotropic dielectric media of relative permittivity $\varepsilon_1, \varepsilon_2$ in domains Ω_1, Ω_2 with a common interface S. To simplify, let Ω_2 be fully enclosed by Ω_1 ($\partial\Omega_2 = S$), with normal vector $\boldsymbol{n}$ on S pointing into Ω_1 (Figure 2.5). On S, the solutions $\boldsymbol{E}^{(1)}$ for the field in Ω_1 and $\boldsymbol{E}^{(2)}$ in Ω_2 are coupled by two relations [Landau et al., 1984, p. 35]: Tangential to the interface, the electric fields are equal,

$$\boldsymbol{E}^{(1)}\cdot\boldsymbol{t} \;=\; \boldsymbol{E}^{(2)}\cdot\boldsymbol{t}, \tag{2.42}$$

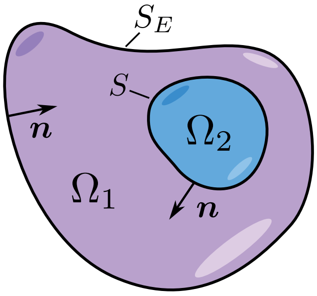

Figure 2.5: Domains Ω_1 and Ω_2 have different electric permittivity. The normal vector $\boldsymbol{n}$ on the shared interface S points into Ω_1.

with tangent vector $\boldsymbol{t}$. In the normal direction, polarization $\boldsymbol{P}$ and field $\boldsymbol{E}$ are discontinuous, but we get continuity in the displacement field,

$$\boldsymbol{D}^{(1)}\cdot\boldsymbol{n} \;=\; \boldsymbol{D}^{(2)}\cdot\boldsymbol{n}. \tag{2.43}$$

As for Stokes flow in Section 2.1.4, we now combine the BIEs that describe the fields in Ω_1 and Ω_2 to reach a description for the coupled domains. For $\boldsymbol{x}_0$ in Ω_1, BIEs (2.37) and (2.38) give

$$\varphi^{(1)}(\boldsymbol{x}_0) \;=\; \int_{S\cup S_E}\left[\varphi^{(1)}(\boldsymbol{x})T_{\boldsymbol{n}}(\boldsymbol{x}-\boldsymbol{x}_0) + E^{(1)}_{\boldsymbol{n}}(\boldsymbol{x})G(\boldsymbol{x}-\boldsymbol{x}_0)\right]\,\mathrm{d}^2\boldsymbol{x}, \tag{2.44a}$$

$$0 \;=\; -\int_S\left[\varphi^{(2)}(\boldsymbol{x})T_{\boldsymbol{n}}(\boldsymbol{x}-\boldsymbol{x}_0) + E^{(2)}_{\boldsymbol{n}}(\boldsymbol{x})G(\boldsymbol{x}-\boldsymbol{x}_0)\right]\,\mathrm{d}^2\boldsymbol{x}, \tag{2.44b}$$

with $S_E := \partial\Omega_1 \setminus S$ some external boundary of Ω_1, like an electrode at fixed potential. The sign in the second equation is flipped to respect the definition of the normal vector on S. The electric potential φ is continuous on the interface, but for the wall-normal field $E_{\boldsymbol{n}}^{(i)}$, we write relation (2.43) as $\varepsilon_1 E_{\boldsymbol{n}}^{(1)} = \varepsilon_2 E_{\boldsymbol{n}}^{(2)}$. With

$$\varepsilon := \frac{\varepsilon_2}{\varepsilon_1} \tag{2.45}$$

the *permittivity ratio* between the dielectrics, and dropping the index $^{(1)}$, we add (2.44a) and (2.44b), which yields

$$\begin{aligned} \varphi(\boldsymbol{x}_0) = & \int_{S_E}^{PV} \left[\varphi(\boldsymbol{x}) T_{\boldsymbol{n}}(\boldsymbol{x}-\boldsymbol{x}_0) + E_{\boldsymbol{n}}(\boldsymbol{x}) G(\boldsymbol{x}-\boldsymbol{x}_0)\right] \mathrm{d}^2\boldsymbol{x} \\ & + \int_S \left(1-\frac{1}{\varepsilon}\right) E_{\boldsymbol{n}}(\boldsymbol{x}) G(\boldsymbol{x}-\boldsymbol{x}_0)\, \mathrm{d}^2\boldsymbol{x} \end{aligned} \tag{2.46}$$

for $\boldsymbol{x}_0 \in \Omega_1$, with $E_{\boldsymbol{n}} := E_{\boldsymbol{n}}^{(1)}$. The same relation holds for $\boldsymbol{x}_0 \in \Omega_2$ and $\boldsymbol{x}_0 \in S$. In the same way, we reach the expression for $\boldsymbol{x}_0 \in S_E$,

$$\begin{aligned} \frac{1}{2}\varphi(\boldsymbol{x}_0) = & \int_{S_E}^{PV} \left[\varphi(\boldsymbol{x}) T_{\boldsymbol{n}}(\boldsymbol{x}-\boldsymbol{x}_0) + E_{\boldsymbol{n}}(\boldsymbol{x}) G(\boldsymbol{x}-\boldsymbol{x}_0)\right] \mathrm{d}^2\boldsymbol{x} \\ & + \int_S \left(1-\frac{1}{\varepsilon}\right) E_{\boldsymbol{n}}(\boldsymbol{x}) G(\boldsymbol{x}-\boldsymbol{x}_0)\, \mathrm{d}^2\boldsymbol{x}. \end{aligned} \tag{2.47}$$

Electric Field in the Volume with a Dielectric Interface

From the electrical potential $\varphi(\boldsymbol{x}_0)$ in the domains Ω_1 and Ω_2 (eq. 2.46), we calculate the field $\boldsymbol{E} = -\nabla\varphi$ as

$$\begin{aligned} \boldsymbol{E}(\boldsymbol{x}_0) = & \int_{S_E} \left[\varphi(\boldsymbol{x}) \boldsymbol{\Pi}_{\boldsymbol{n}}(\boldsymbol{x}-\boldsymbol{x}_0) + E_{\boldsymbol{n}}(\boldsymbol{x}) \boldsymbol{T}(\boldsymbol{x}-\boldsymbol{x}_0)\right] \mathrm{d}^2\boldsymbol{x} \\ & + \int_S \left(1-\frac{1}{\varepsilon}\right) E_{\boldsymbol{n}}(\boldsymbol{x}) \boldsymbol{T}(\boldsymbol{x}-\boldsymbol{x}_0)\, \mathrm{d}^2\boldsymbol{x}, \end{aligned} \tag{2.48}$$

with functions $\boldsymbol{T}(\boldsymbol{r})$, $\boldsymbol{\Pi}_{\boldsymbol{n}}(\boldsymbol{r})$ as defined in eq. (2.41). On the interface S, the field $\boldsymbol{E}$ is not defined, as there is a jump in the normal field component $E_{\boldsymbol{n}}^{(i)}$ on either side due to the jump in polarization.

Boundary Integral Equation for the Electric Field on S

On the interface S, neither the potential $\varphi(\boldsymbol{x}_0)$ nor the wall-normal field $E_{\boldsymbol{n}}(\boldsymbol{x})$ are known. A single BIE, like (2.46), is insufficient to determine both. We want to eliminate the dependence on $\varphi(\boldsymbol{x}_0)$ and describe the field at the interface purely in terms of $E_{\boldsymbol{n}}$.

To eliminate φ, we use the BIE (2.48) for the field $\boldsymbol{E}$ in the domains Ω_1 and Ω_2, away from the interface. With $\boldsymbol{n}_0$ the normal to S at $\boldsymbol{x}_0$ pointing into Ω_1, and $\boldsymbol{x}_0' \in (\Omega_1 \cup \Omega_2)$, we get

$$\begin{aligned} \boldsymbol{E}(\boldsymbol{x}_0') \cdot \boldsymbol{n}_0 &= \int_{S_E} \left[\varphi(\boldsymbol{x}) \boldsymbol{\Pi}_{\boldsymbol{n}}(\boldsymbol{x}-\boldsymbol{x}_0) \cdot \boldsymbol{n}_0 + E_{\boldsymbol{n}}(\boldsymbol{x}) \boldsymbol{T}(\boldsymbol{x}-\boldsymbol{x}_0) \cdot \boldsymbol{n}_0\right] \mathrm{d}^2\boldsymbol{x} \\ &+ \int_S \left(1-\frac{1}{\varepsilon}\right) E_{\boldsymbol{n}}(\boldsymbol{x}) \boldsymbol{T}(\boldsymbol{x}-\boldsymbol{x}_0) \cdot \boldsymbol{n}_0 \, \mathrm{d}^2\boldsymbol{x}. \end{aligned} \tag{2.49}$$

Calculating the field on S is difficult due to the jump in the normal component, $E_{\boldsymbol{n}}^{(2)} = \frac{1}{\varepsilon} E_{\boldsymbol{n}}^{(1)}$. With $E_{\boldsymbol{n}} := E_{\boldsymbol{n}}^{(1)}$ (as before), the limit process $\boldsymbol{x}_0' \to \boldsymbol{x}_0$ yields

$$\begin{aligned} \frac{1}{2}\left(1+\frac{1}{\varepsilon}\right) E_{\boldsymbol{n}}(\boldsymbol{x}_0) &= \int_{S_E} \left[\varphi(\boldsymbol{x}) \boldsymbol{\Pi}_{\boldsymbol{n}}(\boldsymbol{x}-\boldsymbol{x}_0) \cdot \boldsymbol{n}_0 + E_{\boldsymbol{n}}(\boldsymbol{x}) \boldsymbol{T}(\boldsymbol{x}-\boldsymbol{x}_0) \cdot \boldsymbol{n}_0\right] \mathrm{d}^2\boldsymbol{x} \\ &+ \int_S^{PV} \left(1-\frac{1}{\varepsilon}\right) E_{\boldsymbol{n}}(\boldsymbol{x}) \boldsymbol{T}(\boldsymbol{x}-\boldsymbol{x}_0) \cdot \boldsymbol{n}_0 \, \mathrm{d}^2\boldsymbol{x} \end{aligned} \tag{2.50}$$

for $\boldsymbol{x}_0 \in S$ and S smooth.

Having eliminated the potential from the BIE on S, we can now solve an electrostatics problem as follows: From a given potential on S_E, we use equations (2.47) and (2.50) to determine the field $E_{\boldsymbol{n}}$ on all surfaces. From $E_{\boldsymbol{n}}$, we can directly calculate the electric potential in the bulk with the expression (2.46) and the field with eq. (2.48). To calculate the electric field $\boldsymbol{E}^{(1)}(\boldsymbol{x}_0)$ for $\boldsymbol{x}_0 \in S$, we determine the normal component $E_{\boldsymbol{n}}$ with eq. (2.50), and the tangential component $E_{\boldsymbol{t}}$, which does not jump on the interface, with eq. (2.48).

2.3 Surface Stress Models for Stokes Flow

The solutions for Stokes flow on either side of a free interface are coupled by a surface stress $\Delta\boldsymbol{f}$, which compensates the difference in the hydrodynamic stress that the two fluids exert on the interface. We discussed this coupling in Section 2.1.4 and defined $\Delta\boldsymbol{f}$ in equation (2.19). Stresses on the interface are caused by different physical effects, three of which we model in this section.

2.3.1 Young-Laplace Surface Tension Model

The *surface tension* γ is the energy per unit area of an interface between two liquids. If the interface is curved, the surface tension causes a drop in pressure between the two liquids. The pressure drop is described by the Young-Laplace equation [Probstein, 2003]

$$\Delta p = 2\gamma\kappa, \tag{2.51}$$

with the pressure drop $\Delta p := p^{(2)} - p^{(1)}$, the *mean curvature*

$$\kappa := \frac{1}{2}(\nabla \cdot \boldsymbol{n}) = \frac{1}{2}\left(\frac{1}{R_x} + \frac{1}{R_y}\right) \tag{2.52}$$

of the surface with normal $\boldsymbol{n}$, and R_x, R_y the principal radii of curvature. The curvature is defined such that a convex droplet has a positive curvature. For a constant surface tension γ, the surface stress due to surface tension is [Pozrikidis, 2011, p. 234f][2]

$$\Delta \boldsymbol{f}_\gamma = -2\gamma\kappa\boldsymbol{n}. \tag{2.53}$$

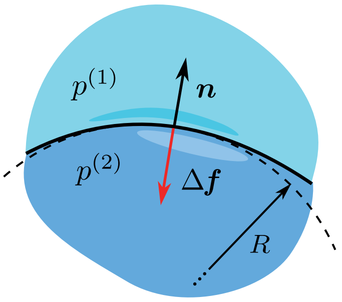

Figure 2.6: Surface tension causes a normal stress on the interface, which acts to reduce the curvature.

Inhomogeneous Surface Tension

In general, the surface tension γ between two liquids can vary along the interface. The most common causes are variations in temperature or in the local density of surfactants. In the presence of an in-plane gradient of surface tension, the surface stress is [Pozrikidis, 2011, p. 235]

$$\Delta \boldsymbol{f}_\gamma = -2\gamma\kappa\boldsymbol{n} + (\boldsymbol{n} \times \nabla\gamma) \times \boldsymbol{n}. \tag{2.54}$$

The in-plane stresses in $\Delta \boldsymbol{f}$ are called *Marangoni stresses*. As briefly mentioned in Section 1.1, modeling the relation between surfactant kinetics and surface tension is a topic of ongoing research in the field of surface rheology, and various models exist.

2.3.2 Dielectric Surface Stress

When the two fluids have different electric permittivities, an electric field causes a normal stress on the interface, directed into the medium of lower permittivity. This stress is due to a jump in the Maxwell stress tensor $\hat{\boldsymbol{\sigma}}_m$ with

$$(\sigma_m)_{ij} := \varepsilon_0\varepsilon_r E_i E_j - \tfrac{1}{2}\varepsilon_0\varepsilon_r |\boldsymbol{E}|^2 \delta_{ij} \tag{2.55}$$

for a material of relative permittivity ε_r in an electric field $\boldsymbol{E}$ [Landau et al., 1984, p. 29]. On the interface between the fluids with permittivity ε_1 and ε_2, the stress is

$$\Delta \boldsymbol{f}_{\text{Maxwell}} = \hat{\boldsymbol{\sigma}}_m^{(2)}\boldsymbol{n} - \hat{\boldsymbol{\sigma}}_m^{(1)}\boldsymbol{n}, \tag{2.56}$$

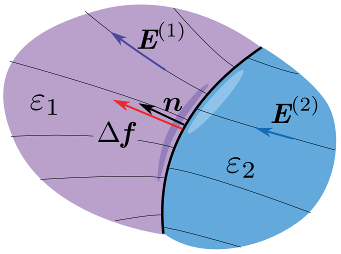

Figure 2.7: Interface between two dielectrics with $\varepsilon_2 > \varepsilon_1$. The surface stress is always directed towards the domain of lower permittivity.

with $\boldsymbol{n}$ pointing into the medium of permittivity ε_1. With the tangential fields matching ($\boldsymbol{E}^{(1)} \cdot \boldsymbol{t} = \boldsymbol{E}^{(2)} \cdot \boldsymbol{t}$) and the normal components following the relation $\varepsilon_1 E_{\boldsymbol{n}}^{(1)} = \varepsilon_2 E_{\boldsymbol{n}}^{(2)}$ as in

---

[2] Pozrikidis [2011] defines $\Delta \boldsymbol{f}$ with the opposite sign, which changes the signs in his equation 3.8.10.

Section 2.2.2, the Maxwell stress on the interface is [Sherwood, 1988]

$$\Delta \boldsymbol{f}_{\text{Maxwell}} = -\tfrac{1}{2}\varepsilon_0\varepsilon_1 \left[\left(1-\frac{1}{\varepsilon}\right)E_{\boldsymbol{n}}^2 - (1-\varepsilon)\,E_{\boldsymbol{t}}^2\right]\boldsymbol{n}, \tag{2.57}$$

with the normal field $E_{\boldsymbol{n}} := \boldsymbol{E}^{(1)}\cdot\boldsymbol{n}$, tangential field $E_{\boldsymbol{t}} := |\boldsymbol{E}^{(1)} - E_{\boldsymbol{n}}\cdot\boldsymbol{n}|$ and permittivity ratio $\varepsilon := \frac{\varepsilon_2}{\varepsilon_1}$. When the electric field is determined from the boundary integral equations in Section 2.2, the normal field component $E_{\boldsymbol{n}}$ is directly known on the interface. The tangential field, however, needs to be computed from another boundary integration, equation (2.48) in Section 2.2.2.

2.3.3 Surface Stress due to Gravity

The effect of gravity is small in most microfluidic applications, and can typically be neglected. In cases where the two fluids have different densities, $\rho^{(1)} \neq \rho^{(2)}$, the modified pressure $p' := p + \rho g z$ defined in Section 2.1 differs between the two fluids. At the interface, the pressure in fluid (i) is

$$p^{(i)} = p'^{(i)} - \rho^{(i)} g z. \tag{2.58}$$

Gravity thus adds a pressure difference of

$$\Delta p_g = \left(\rho^{(2)} - \rho^{(1)}\right) g z,$$

which by definition of the stress tensor (2.2) implies a wall-normal surface stress of

$$\Delta \boldsymbol{f}_g = -\Delta\rho g z\cdot\boldsymbol{n}, \tag{2.59}$$

with $\Delta\rho := \rho^{(2)} - \rho^{(1)}$. Note here that the choice of the reference point $z = 0$ is arbitrary: Adding or subtracting a constant offset would increase or decrease the modified pressure $p'^{(2)}$ in the droplet domain Ω_2, but not change the velocity on the interface S or any values on the external surfaces S_B. General volume forces cannot be treated by the boundary element method, since the pressure term cannot account for an inhomogeneous force distribution.

2.4 Further Relevant Boundary Integrals

With the setup to evaluate boundary integrals in place, we want to use boundary integration to calculate further quantities of interest. From just the geometrical description of the free interface S of a droplet, we will calculate its volume (Section 2.4.1), center of mass (Section 2.4.2), and determine whether a given point $\boldsymbol{x}_0$ is inside a droplet (Section 2.4.3).

2.4.1 Volume of a Domain

Consider the domain Ω with surface $S := \partial\Omega$ and normal $\boldsymbol{n}$ pointing outwards. The volume V of Ω is

$$V := \int_\Omega 1 \, \mathrm{d}^3\boldsymbol{x}. \tag{2.60}$$

Using the divergence theorem (eq. 2.13) with function $\boldsymbol{F}(\boldsymbol{x}) := \frac{\boldsymbol{x}}{3}$ (with $\nabla \cdot \boldsymbol{F} = 1$), we calculate the volume V as

$$V = \int_\Omega \left(\nabla \cdot \frac{\boldsymbol{x}}{3}\right) \mathrm{d}^3\boldsymbol{x} = \frac{1}{3}\int_S \boldsymbol{x} \cdot \boldsymbol{n} \, \mathrm{d}^2\boldsymbol{x}. \tag{2.61}$$

In the numerical scheme, we use this calculation to verify that the volume of the droplets in the system does not change over the course of the forward time integration.

2.4.2 Center of Mass

At constant density, the center of mass $\boldsymbol{x}_{CM}$ of a fluid in the domain Ω (again with surface $S := \partial\Omega$ and outward normal $\boldsymbol{n}$) is given by

$$\boldsymbol{x}_{CM} := \frac{1}{V}\int_\Omega \boldsymbol{x} \, \mathrm{d}^3\boldsymbol{x}. \tag{2.62}$$

We compute the volume V as in Section 2.4.1 and use the divergence theorem with the identity $\boldsymbol{x} = \frac{1}{2}\nabla|\boldsymbol{x}|^2$ to obtain

$$\boldsymbol{x}_{CM} = \frac{1}{V}\int_S \frac{|\boldsymbol{x}|^2}{2} \boldsymbol{n} \, \mathrm{d}^2\boldsymbol{x}. \tag{2.63}$$

The center of mass is typically used to track the position of droplets.

2.4.3 Determine if a Point is Inside a Domain

In determining the velocity field in the bulk of a two-phase flow with an interface (Section 2.1.4), the boundary integral equation for the velocity $\boldsymbol{u}(\boldsymbol{x}_0)$ in domain Ω_2 has a different prefactor than in Ω_1, since the fluid viscosity is different. To write a combined bulk velocity field, we determine if $\boldsymbol{x}_0$ is in domain Ω_2, and rescale the velocity accordingly.

To find out whether $\boldsymbol{x}_0$ is in domain Ω_2, we solve the Laplace equation on Ω_2 as in Section 2.2.1, with $\varphi = 1$ and $E_{\boldsymbol{n}} = 0$ on the boundary S. The resulting boundary integral

$$\varphi(\boldsymbol{x}_0) = -\int_S T_{\boldsymbol{n}}(\boldsymbol{x} - \boldsymbol{x}_0) \, \mathrm{d}^2\boldsymbol{x} \tag{2.64}$$

(with $T_{\boldsymbol{n}}$ as in eq. (2.36a), $\boldsymbol{n}$ pointing into Ω_1), which is a simplification of equations (2.37) and

(2.38), takes the values

$$\varphi(\boldsymbol{x}_0) \;=\; \begin{cases} 1 & \boldsymbol{x}_0 \in \Omega_2 \\ 0 & \text{else.} \end{cases} \tag{2.65}$$

Thresholding this indicator value at $\frac{1}{2}$ gives the domain of $\boldsymbol{x}_0$.

2.5 Stokes Flow in a Rectangular Duct

In the simulations, we define a boundary condition for the flow inlet (Section 2.1.3). This reduces the numerical effort compared to simulating the flow far from regions of interest and letting it develop until it reaches the region of interest. The closer the prescribed inlet condition matches the asymptotic profile of the developed flow, the shorter the inlet domain can be chosen.

Typical ducts in microfluidic devices are either cylindrical or have a rectangular cross-section. In practice, rectangular ducts are most common, as they are easy to design and manufacture with soft lithography methods. In this section, we discuss the velocity profile for Stokes flow in a straight, rectangular duct. Unlike in the case of a cylindrical capillary, no simple mathematical expression exists for the downstream velocity or pressure gradient. Therefore, we discuss the accuracy of different approximations.

2.5.1 Series Representation for the Velocity

For the downstream velocity $u_x(y,z)$ in a straight rectangular duct of width W and height H, Spiga and Morino [1994] give the expression

$$u_x(y,z) \;=\; U^* \cdot \frac{16\beta^2}{\pi^4} \sum_{n\,\text{odd}} \sum_{m\,\text{odd}} \frac{\sin\left(\frac{n\pi y}{W} + \frac{n\pi}{2}\right)\sin\left(\frac{m\pi z}{H} + \frac{m\pi}{2}\right)}{nm(\beta^2 n^2 + m^2)}, \tag{2.66}$$

with the coordinates $y \in \left[-\frac{W}{2} : \frac{W}{2}\right]$ and $z \in \left[-\frac{H}{2} : \frac{H}{2}\right]$, and aspect ratio $\beta := \frac{W}{H}$, which follows from a finite Fourier transform. The cross-stream velocity is zero ($u_y \equiv u_z \equiv 0$), and the pressure only depends on the downstream coordinate x ($p \equiv p(x)$). The velocity scale U^* is given in terms of the downstream pressure gradient as

$$U^* \;:=\; \frac{W^2}{\mu} \cdot \left(-\frac{\partial p}{\partial x}\right), \tag{2.67}$$

and the mean velocity $U := \langle u_x \rangle_{y,z}$ is

$$U \;=\; U^* \cdot \frac{64\beta^2}{\pi^6} \sum_{n\,\text{odd}} \sum_{m\,\text{odd}} \frac{1}{n^2 m^2 (\beta^2 n^2 + m^2)}. \tag{2.68}$$

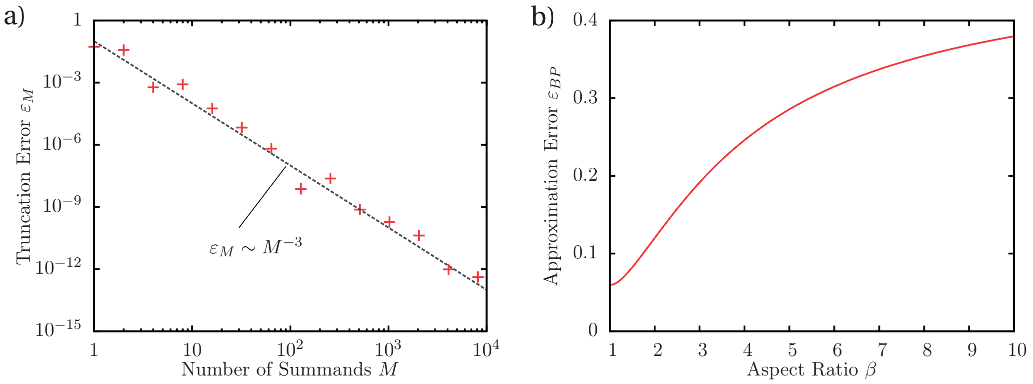

Figure 2.8: Errors of approximating the velocity in a rectangular duct. *a)* Relative local error ε_M of truncating the series expression for flow in a rectangular duct at $\beta = 1$ to the first M terms in both spatial directions. *b)* Relative mean error ε_{BP} of expressing the flow in a rectangular duct by a biparabolic profile u_{BP}. Since H and W can be exchanged, the errors for $1/\beta$ are identical to those for β.

Convergence of the Series

We estimate the error we incur when truncating the sums in eq. (2.66) and (2.68) to their first M terms. If we assume the series to be converged at $M = 2^{14}$, the relative local error

$$\varepsilon_M := \frac{|u_M(y,z) - u_\infty(y,z)|}{u_\infty(y,z)},$$

here evaluated at $(y,z) \approx (0.1858, 0.1858)$, decays with order $\mathcal{O}(M^{-3})$ (Figure 2.8a). With this convergence, an error of $\varepsilon_M < 10^{-6}$ is reached at $M = 64$, and we extrapolate that the error decays to machine precision ($\varepsilon_M \leq 10^{-16}$) at $M = 10^5$.

2.5.2 Approximation by a Biparabolic Profile

A more crude approximation for the downstream flow in a rectangular duct is given by the relation

$$u_{\mathrm{BP}}(y,z) := \frac{9U}{4} \cdot \left(\frac{4y^2}{W^2} - 1\right) \cdot \left(\frac{4z^2}{H^2} - 1\right), \tag{2.69}$$

which is a simple superposition of two parabolas. As can be seen in Figure 2.9a, this profile matches the analytic solution for a square channel close to the side walls, but significantly overestimates the velocity close to the center, in particular for ducts of high aspect radio (large or small β). The relative mean error

$$\varepsilon_{BP} := \frac{\sqrt{\langle [u_{\mathrm{BP}} - u]^2 \rangle_{y,z}}}{U} \tag{2.70}$$

is large even for aspect ratios near unity, and grows with β (Figure 2.8b).

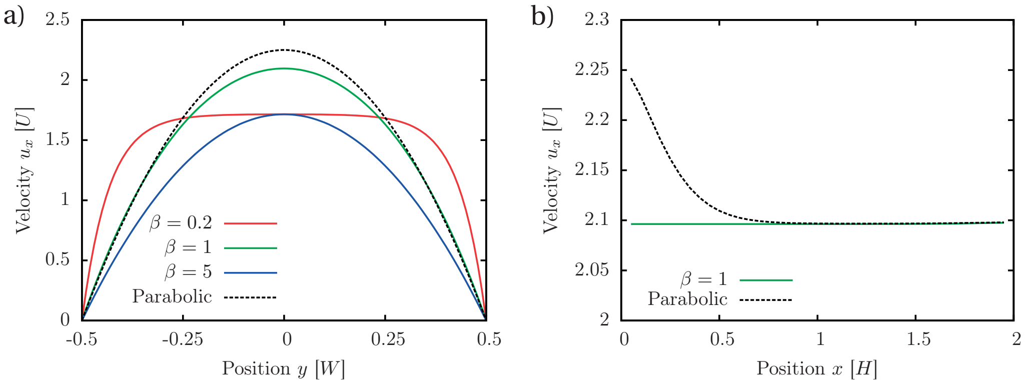

Figure 2.9: Accuracy of the paraboloid inlet boundary condition, in an empty, rectangular channel of height H and width W. *a)* Velocity profile for the converged series solution, and approximation, along a line through the channel center. *b)* In a square duct ($\beta = 1$), the center-line velocity converges towards the exact solution over a distance shorter than the channel height H. Data from the fully resolved numerical simulation.

Despite the deviation from the analytic solution, a biparabolic flow profile has properties that make it useful as a boundary condition for the flow into a rectangular duct: By construction, the mean flow through the system is exact up to numerical precision, and evaluating the function $u_{\mathrm{BP}}(y,z)$ is trivially easy.

With u_{BP} as boundary condition, the downstream flow in an empty rectangular duct quickly assumes the profile given by the converged analytic series (2.66): We find that the deviation between biparaboloid approximation and the full analytic solution goes to zero on a length scale $\Delta L \approx H$ (Figure 2.9b). In ducts with varying width or flows with droplets, where the profile (2.66) is not the analytic solution, we therefore define an inlet section of length $L \geq H$, in which the flow can adjust from any chosen inlet condition to an appropriate downstream profile.

2.5.3 Pressure Gradient in a Rectangular Duct

The stress that the side walls exert on a flow in a rectangular duct is compensated by a constant pressure gradient inside the fluid. From the series expression of the downstream velocity profile $u_x(y,z)$ (eq. 2.66), the relation between downstream pressure gradient and mean flow velocity is

$$\frac{\partial p}{\partial x} = -\frac{\pi^6}{64\beta^2} \cdot \frac{\mu U}{WH} \cdot \left[\sum_{n\,\mathrm{odd}} \sum_{m\,\mathrm{odd}} \frac{1}{n^2 m^2 (\beta^2 n^2 + m^2)} \right]^{-1}. \tag{2.71}$$

If instead we assume biparabolic flow with profile $u_{\mathrm{BP}}(y,z)$ (eq. 2.69), the resulting pressure

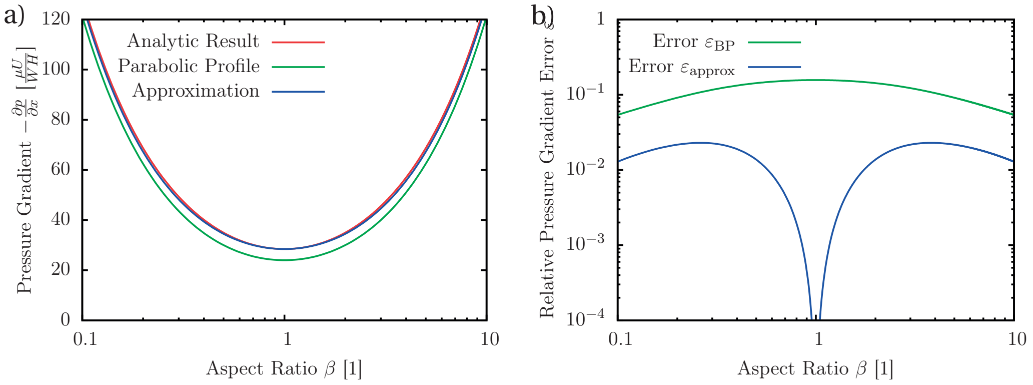

Figure 2.10: Approximations of the downstream pressure gradient in a rectangular duct. *a)* Pressure gradient (2.71) and approximations (2.72) and (2.73). *b)* Relative errors of the two approximations.

gradient is

$$\left.\frac{\partial p}{\partial x}\right|_{\mathrm{BP}} = -12\frac{\mu U}{WH}\left(\beta+\beta^{-1}\right). \tag{2.72}$$

As shown in Figure 2.10, this relation underestimates the true pressure gradient. From a least-squares-fit in the range [0.1 : 10] to the relation (2.71), constrained to match the analytic expression at $\beta = 1$, we get the approximation

$$\left.\frac{\partial p}{\partial z}\right|_{\mathrm{approx}} = -\left[4.256086 + 12.099034\cdot\left(\beta+\beta^{-1}\right)\right]\frac{\mu U}{WH}. \tag{2.73}$$

The relative error of this approximation stays below 10^{-2} for $\beta \in [0.6, 1.7]$, below 10^{-3} for $\beta \in [0.86, 1.16]$ and below 10^{-4} for $\beta \in [0.96, 1.04]$.

2.5.4 Poiseuille Flow

For a cylindrical capillary, *Poiseuille's law* gives a closed-form solution for the downstream velocity and the pressure gradient, which we note here for the sake of completeness. For flow in a cylindrical capillary of radius R, the downstream velocity is [Pozrikidis, 2011, p. 317]

$$u_x(r) = \frac{2U}{R^2}(R^2 - r^2) \tag{2.74}$$

and the pressure gradient is

$$\frac{\partial p}{\partial x} = -\frac{8\mu U}{R^2}. \tag{2.75}$$

2.6 Summary

The equations of Stokes flow (Section 2.1) are linear and have no local time derivative, so that in the absence of volume forces, the entire solution for the flow field in a 3D domain can be represented by the velocities and stresses on the boundary. The boundary integral equations (Section 2.1.2) relate the field at some point $\boldsymbol{x}_0$ in the domain to the flow solution on the boundary; by moving $\boldsymbol{x}_0$ onto the boundary, we get a closed set of equations that describe the full Stokes solution. In the presence of free surfaces — such as a droplet interface — the solutions in the two fluid domains are coupled by the stress jump $\Delta\boldsymbol{f}$ at the interface (Section 2.1.4), which is given by surface tension and other physical forces (Section 2.3).

One particular interface force is due to the jump in Maxwell stress, caused by the different electric polarization of the two fluids that form the interface (Section 2.2). Much like the equations for Stokes flow, the Laplace equation that describes the electric field can be expressed as a boundary integral equation (Section 2.2.1), and coupled between two domains (Section 2.2.2).

As an inlet boundary condition for Stokes flow in a rectangular duct, we use an approximation of the analytic flow profile (Section 2.5). From the analytic flow profile, we can approximate the streamwise pressure gradient with high accuracy.

Part I

Boundary Element Method for 3D Stokes Flow

The *Boundary Integral Equations* for Stokes flow describe Newtonian incompressible flow at small Reynolds numbers. We use the numerical *Boundary Element Method* to find a solution to these equations.

In computational fluid dynamics, a vast majority of computational resources is spent on simulating turbulent flows at high Reynolds numbers, dominated by the nonlinear material derivative $(\partial_t \boldsymbol{u} + \boldsymbol{u} \cdot \nabla \boldsymbol{u})$ which marks the difference between the nonlinear Navier-Stokes equations and the linear Stokes equations. In comparison, a set of linear partial differential equations like the Stokes equations appears almost trivial to solve. However, the presence of a free interface renders this problem complicated: While the Stokes equations itself are linear, the resulting flow deforms the free interfaces, which mark the domains on which the differential equations are defined. This coupling renders the whole problem nonlinear, which allows for the complex dynamics that make microfluidics such a versatile tool in applications.

In this part of the thesis, we develop the discretized numerical scheme that our *Droplet* code implements. The code provides a full 3D simulation for the deformation and interaction of one or more droplets in complex microchannel geometries. One particular novelty of our approach lies in the representation of interfaces in 3D (Section 3.4), where a higher-order interpolation scheme supports our efforts to reduce the total number of mesh vertices in the large geometry. Another important feature is the coupling between electric fields and the Stokes solver (Section 3.2), which we use to study droplet deformation and actuation in electric fields.

The description of the numerical scheme is separated into two chapters: In Chapter 3, we derive the discretized equations for the scheme and discuss the implemented algorithms. In Chapter 4, we show the results of the validation and testing that we performed against known numerical and analytic results.

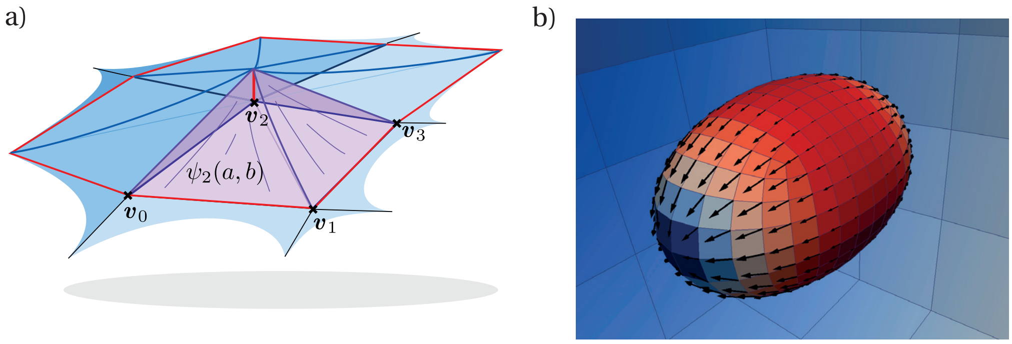

Boundary Element Method and its validation. *a)* The boundary integrals are evaluated by integrating over shape functions on a quadrilateral mesh (Section 3.3). *b)* The method determines the flow field on the droplet surface, here for a droplet in an extensional flow (Section 4.4).

3 Numerical Implementation

Contents

3.1 Boundary-Element Simulation of Stokes Flow . . . 37
  3.1.1 Discretizing the Boundary Integral Equations . . . 38
  3.1.2 Solving the Linear System . . . 39
3.2 Boundary-Element Simulation for Electrostatics . . . 40
3.3 Mesh and Surface Representation . . . 41
  3.3.1 Local Refinement . . . 42
  3.3.2 Treatment of Edges . . . 42
  3.3.3 Constraining Degrees of Freedom . . . 43
3.4 Smooth Surface Representation . . . 43
  3.4.1 Approximating the Normal Vector . . . 44
  3.4.2 Locally Fitting a Paraboloid . . . 44
  3.4.3 Interpolating Between Corner Vertices of a Cell . . . 46
  3.4.4 Properties of the Representation . . . 46
3.5 Numerical Integration . . . 49
  3.5.1 Nearly Singular Integration . . . 49
  3.5.2 Accuracy of the Numerical Quadrature . . . 50
3.6 Time Stepping . . . 53
  3.6.1 Stability of the Time Stepping . . . 53
  3.6.2 Mesh Regularization . . . 54
3.7 Implementation . . . 55
  3.7.1 Parallelization . . . 55
3.8 Summary . . . 57

In this chapter, we develop the numerical simulation scheme for 3D simulation of droplet dynamics. In Sections 3.1 and 3.2, we derive the discretized equations for Stokes flow and electrostatics. The discretized equations form a linear system, which we solve iteratively. In Section 3.3, we discuss the standard representation of surfaces in our geometry, and the correspondence between mesh vertices and degrees of freedom of the numerical scheme. Section 3.4 presents a special representation of smooth surfaces, with better approximation properties to free droplet interfaces than standard approaches. The quadrature schemes that we use to solve the surface integrals are discussed in Section 3.5. Section 3.6 discusses the approach to forward time integration. Details of the implementation are given in Section 3.7.

Physical Units and Nondimensionalization

While the solution of a physical problem is independent of the physical units in which it is expressed, the accuracy of a numerical implementation in single or double precision arithmetic increases if it operates on numbers near unity. We choose characteristic physical dimensions based on the typical flow situation of a droplet moving in a microchannel.

- **Lengths and distances** are measured in units of H, the height of the microchannel. Typical microchannel heights are on the order of $H \sim (50-100)\ \mu\mathrm{m}$.
- **Velocities** are measured in units of U, the mean flow velocity across the channel. In experiments, flow rates are easy to change, and vary in a range of $U \sim (10^{-3} - 10^{0})\,\frac{\mathrm{m}}{\mathrm{s}}$.
- **Viscosity** is measured in units of the viscosity μ of the continuous phase. A typical value for silicon oil is $\mu \approx 1.24 \cdot 10^{-3}\ \frac{\mathrm{kg}}{\mathrm{m\,s}}$.
- **Electric permittivity** is measured in units of the permittivity $\varepsilon_0\varepsilon_1$ of the outer phase. The vacuum permittivity is $\varepsilon_0 = 8.854 \cdot 10^{-12}\,\frac{\mathrm{C}^2\mathrm{s}^2}{\mathrm{kg\,m}^3}$, and the relative permittivity ε_1 for a non-polar oil is typically around unity.

From these physical base dimensions, we deduce other physical quantities:

- **Time** T is given in units $T_* := \frac{L}{U}$, with a characteristic time scale $T_* \sim (10^{-6} - 10^{-3})$ s.
- **Density** ρ has the units $\rho_* := \frac{\mu}{UL}$.
- **Electric Potential** φ is given in units $\varphi_* := \sqrt{\frac{\mu U L}{\varepsilon_0\varepsilon_1}}$.
- Consequently, the **Electric Field** $\boldsymbol{E}$ is given in units $E_* := \sqrt{\frac{\mu U}{\varepsilon_0\varepsilon_1 L}}$.

All other physical quantities can then be expressed by dimensionless numbers. We discuss dynamics in terms of the following dimensionless quantities:

- The **viscosity ratio** $\lambda := \frac{\mu_d}{\mu}$ between the droplet viscosity and the viscosity of the continuous phase.
- The **permittivity ratio** $\varepsilon := \frac{\varepsilon_2}{\varepsilon_1}$ between the relative permittivity of the droplet and that of the material surrounding it.
- The **capillary number** $Ca := \frac{\mu U}{\gamma}$, describing the relative strength of the viscous stresses compared to the surface tension γ of the droplet interface.
- The **Reynolds number** $Re := \frac{UL\rho}{\mu} = \frac{\rho}{\rho_*}$, describing the relative importance of inertial effects. For the Stokes formulation to hold, we require the Reynolds number to be small.
- The **Archimedes number** $Ar := \frac{\rho g L^3 \cdot \Delta\rho}{\mu^2}$, with $\Delta\rho := \rho_d - \rho$, and ρ_d and ρ the densities of the droplet and continuous phase, respectively, describing the relative strength of buoyancy forces compared to viscous forces. Unless mentioned otherwise, we assume the Archimedes number to be small and neglect the effect of gravity.
- The **electrical Bond number** $Bo_E := \frac{\varepsilon_0 \varepsilon_1 E^2 R}{\gamma}$, with R the droplet radius, describing the strength of an electric field relative to the surface tension of a droplet.

3.1 Boundary-Element Simulation of Stokes Flow

To find a solution for the Boundary Integral Equations for Stokes flow (eq. 2.23 and 2.24), we need to express the equations as a linear system, with the solution expressed through a finite number of scalar coefficients. The representation of the solution is reminiscent of that in the Finite-Element Method (FEM) (as described for example by Gresho and Sani [1998]), just on an embedded manifold: On some smooth manifold $\mathcal{M}$ (where $\mathcal{M}$ would be some boundary S or S_B of the flow), we define N basis functions $\psi_n(\boldsymbol{x})$ with the properties

$$0 \le \psi_n(\boldsymbol{x}) \le 1 \qquad \forall \boldsymbol{x} \in \mathcal{M}, \tag{3.1a}$$

$$\sum_{n=1}^{N} \psi_n(\boldsymbol{x}) = 1 \qquad \forall \boldsymbol{x} \in \mathcal{M}, \tag{3.1b}$$

with ψ_n having a compact support on $\mathcal{M}$. The solution $\boldsymbol{g}(\boldsymbol{x})$ on $\mathcal{M}$, with $g_i(\boldsymbol{x}) := u_i(\boldsymbol{x})$ for locations $\boldsymbol{x}$ where the velocity component u_i is unknown, and $g_i(\boldsymbol{x}) := f_i(\boldsymbol{x})$ where the stress component f_i is unknown, is then approximated by the expression

$$g_i(\boldsymbol{x}) \approx \sum_{n=1}^{N} g_i^n \psi^n(\boldsymbol{x}). \tag{3.2}$$

In three dimensions, the solution $\boldsymbol{g}(\boldsymbol{x})$ is represented by the $3N$ scalar coefficients g_i^n, which we call *degrees of freedom*. The lower index refers to the spatial direction ($i \in 1..3$), the upper index to the basis function ($n \in 1..N$). To account for the various boundary conditions on the outer boundary S_B (see Section 2.1.3), we denote with $S_{B,i}$ the part of S_B where velocity component u_i is unknown, and with $\tilde{S}_{B,i}$ the part where stress component f_i is unknown. On the droplet interface S, the unknown field is always $\boldsymbol{u}$.

3.1.1 Discretizing the Boundary Integral Equations

For $\boldsymbol{x}_0 \in (S \cup S_B)$, we express the BIEs (2.23) and (2.24) of Stokes flow as the combined BIE

$$\begin{aligned}\alpha(\boldsymbol{x}_0) \cdot \boldsymbol{u}(\boldsymbol{x}_0) \;=\; & -\frac{1}{\mu} \int\limits_{S_B} \hat{\boldsymbol{G}}(\boldsymbol{x}-\boldsymbol{x}_0) \cdot \boldsymbol{f}(\boldsymbol{x}) \, \mathrm{d}^2\boldsymbol{x} + \int\limits_{S_B} \boldsymbol{u}(\boldsymbol{x}) \cdot \hat{\boldsymbol{T}}(\boldsymbol{x}-\boldsymbol{x}_0) \cdot \boldsymbol{n} \, \mathrm{d}^2\boldsymbol{x} \\ & + \frac{1}{\mu} \int\limits_{S} \hat{\boldsymbol{G}}(\boldsymbol{x}-\boldsymbol{x}_0) \cdot \Delta \boldsymbol{f}(\boldsymbol{x}) \, \mathrm{d}^2\boldsymbol{x} + (1-\lambda) \int\limits_{S} \boldsymbol{u}(\boldsymbol{x}) \cdot \hat{\boldsymbol{T}}(\boldsymbol{x}-\boldsymbol{x}_0) \cdot \boldsymbol{n} \, \mathrm{d}^2\boldsymbol{x},\end{aligned} \tag{3.3}$$

with factor

$$\alpha(\boldsymbol{x}_0) := \begin{cases} 4\pi & \boldsymbol{x}_0 \in S_B \\ 4\pi(1+\lambda) & \boldsymbol{x}_0 \in S \end{cases} \tag{3.4}$$

and viscosity $\mu \equiv \mu_1$ (which is unity in the implementation due to our choice of units).

We implement the *collocation method* [Pozrikidis, 1992, p. 160], i.e. require the BIE (3.3) to hold at a finite number of *collocation points* $\boldsymbol{x}^m$ $(m \in 1..N)$. In our implementation, the collocation points are associated to the basis functions ψ^m and coincide with the vertices of our mesh. To aid our notation, we define the following integrals:

$$A_i^m := \sum_j \int\limits_{S_{B,j}} G_{ij}(\boldsymbol{x}-\boldsymbol{x}^m) f_j(\boldsymbol{x}) \, \mathrm{d}^2\boldsymbol{x} \tag{3.5a}$$

$$B_i^m := \sum_{j,k} \int\limits_{\tilde{S}_{B,j}} u_j(\boldsymbol{x}) T_{ijk}(\boldsymbol{x}-\boldsymbol{x}^m) n_k(\boldsymbol{x}) \, \mathrm{d}^2\boldsymbol{x} \tag{3.5b}$$

$$C_i^m := \sum_j \int\limits_{S} G_{ij}(\boldsymbol{x}-\boldsymbol{x}^m) \Delta f_j(\boldsymbol{x}) \, \mathrm{d}^2\boldsymbol{x} \tag{3.5c}$$

$$D_{ij}^{mn} := \int\limits_{\tilde{S}_{B,j}} G_{ij}(\boldsymbol{x}-\boldsymbol{x}^m) \psi^n(\boldsymbol{x}) \, \mathrm{d}^2\boldsymbol{x} \tag{3.5d}$$

$$E_{ij}^{mn} := \sum_k \int\limits_{S_{B,j}} \psi^n(\boldsymbol{x}) T_{ijk}(\boldsymbol{x}-\boldsymbol{x}^m) n_k(\boldsymbol{x}) \, \mathrm{d}^2\boldsymbol{x} \tag{3.5e}$$

$$F_{ij}^{mn} := \sum_k \int\limits_{S} \psi^n(\boldsymbol{x}) T_{ijk}(\boldsymbol{x}-\boldsymbol{x}^m) n_k(\boldsymbol{x}) \, \mathrm{d}^2\boldsymbol{x}. \tag{3.5f}$$

The evaluation of the boundary integrals is discussed in Section 3.5. With f_j^n the unknown stress coefficients on $\tilde{S}_{B,i}$ as per eq. (3.2), the first integral in eq. (3.3) is approximated as

$$\sum_j \int_{S_B} G_{ij}(\boldsymbol{x}-\boldsymbol{x}^m) f_j(\boldsymbol{x})\, \mathrm{d}^2\boldsymbol{x} \;\approx\; A_i^m + \sum_j \sum_n D_{ij}^{mn} \cdot f_j^n, \tag{3.6}$$

for component i, where the basis function ψ^n has remained inside the integral, but the coefficient f_j^n was pulled out of the integral.[1] The sum over n only sums up the terms where the stress component f_j is unknown. The other integrals of the BIE are approximated accordingly. With u_j^n the unknown velocity coefficients on $S_{B,i}$ as per eq. (3.2), identifying $u_j^m = u_j(\boldsymbol{x}^m)$, and defining $\alpha^m := \alpha(\boldsymbol{x}^m)$, the full BIE (3.3) is then approximated by the relation

$$\begin{aligned} \alpha^m u_i^m \;=\; & -\frac{1}{\mu}\left(A_i^m + \sum_j \sum_n D_{ij}^{mn} \cdot f_i^n\right) \;+\; \left(B_i^m + \sum_j \sum_n E_{ij}^{mn} \cdot u_i^n\right) \\ & + \frac{1}{\mu} C_i^m + (1-\lambda)\left(\sum_j \sum_n F_{ij}^{mn} \cdot u_i^n\right). \end{aligned} \tag{3.7}$$

With $i \in 1..3$ and $m \in 1..N$, equation (3.7) describes a linear system of $3N$ equations for the $3N$ degrees of freedom g_i^n (each of which is either u_i^n or f_i^n); the number of degrees of freedom is $n_{DoF} = 3N$. The linear system can be written as

$$\hat{\boldsymbol{A}} \cdot \vec{g} = \vec{R}, \tag{3.8}$$

with $\vec{g} \in \mathbb{R}^{3N}$ the vector of all degrees of freedom g_i^n, a full matrix $\hat{\boldsymbol{A}} \in \mathbb{R}^{3N \times 3N}$ and a right hand side $\vec{R} \in \mathbb{R}^{3N}$. To determine all coefficients A_i^m, B_i^m, C_i^m, we require $3N$ integrations over the whole boundary, one for each value of i and m. Since the basis functions ψ^n have compact support, calculating the values for the coefficients D_{ij}^{mn}, E_{ij}^{mn} and F_{ij}^{mn} is a $\mathcal{O}(1)$-operation for each coefficient, such that the effort for calculating the matrix $\hat{\boldsymbol{A}}$ is $\mathcal{O}(N^2)$.

3.1.2 Solving the Linear System

To solve the linear system (3.7), we can choose from a number of matrix solvers. A direct solver is not practical for the number of degrees of freedom typically used ($n_{DoF} \sim 10^5 - 10^6$). Since our matrix $\hat{\boldsymbol{A}}$ is not symmetric, but diagonally dominant, we employ the iterative *Generalized Minimal Residual Method* (GMRES, developed by Saad and Schultz [1986]) with *Jacobi Preconditioning*. The $\mathcal{O}(N^2)$-operation of assembling the matrix $\hat{\boldsymbol{A}}$, and the $\mathcal{O}(N^2 \log N)$-runtime of the GMRES-solver, take a similar computational time, which dominates the total solution time of our method. Both steps can be efficiently parallelized, we discuss this parallelization in Section 3.7.1.

---

[1] So far, the approximation purely lies in writing the solution $\boldsymbol{g}$ as the series (3.2). Approximating the integrals (3.5a)-(3.5f) will add another layer of approximation.

3.2 Boundary-Element Simulation for Electrostatics

Solving the boundary integral equations of electrostatics uses the same approach as the solution of the Stokes equations in Section 3.1, but is easier to note down. The (scalar) solution $E_{\boldsymbol{n}}(\boldsymbol{x})$, which is the normal field on both the outer boundary S_E and the free droplet surface S, is represented by a finite number of N coefficients $E^n_{\boldsymbol{n}}$,

$$E_{\boldsymbol{n}}(\boldsymbol{x}) \approx \sum_{n=1}^{N} E^n_{\boldsymbol{n}} \psi^n(\boldsymbol{x}), \tag{3.9}$$

with finite-support basis functions ψ^n as in Section 3.1. We expect the BIEs to hold on a finite number of N collocation points $\boldsymbol{x}^m$ associated to the basis functions ψ^m. For $\boldsymbol{x}^m \in S_E$, we use equation (2.47) with $\boldsymbol{x}_0 = \boldsymbol{x}^m$, which reads

$$\begin{aligned}\frac{1}{2}\varphi(\boldsymbol{x}^m) &= \int_{S_E}^{PV} \left[\varphi(\boldsymbol{x})\,T_{\boldsymbol{n}}(\boldsymbol{x}-\boldsymbol{x}^m) + E_{\boldsymbol{n}}(\boldsymbol{x})G(\boldsymbol{x}-\boldsymbol{x}^m)\right] \mathrm{d}^2\boldsymbol{x} \\ &\quad + \int_{S} \left(1-\frac{1}{\varepsilon}\right) E_{\boldsymbol{n}}(\boldsymbol{x})G(\boldsymbol{x}-\boldsymbol{x}^m)\,\mathrm{d}^2\boldsymbol{x}.\end{aligned} \tag{3.10}$$

For $\boldsymbol{x}^m \in S$, we write equation (2.50) as

$$\begin{aligned}\frac{1}{2}\left(1+\frac{1}{\varepsilon}\right)E^m &= \int_{S_E} \left[\varphi(\boldsymbol{x})\boldsymbol{\Pi}_{\boldsymbol{n}}(\boldsymbol{x}-\boldsymbol{x}^m)\cdot\boldsymbol{n}^m + E_{\boldsymbol{n}}(\boldsymbol{x})\boldsymbol{T}(\boldsymbol{x}-\boldsymbol{x}^m)\cdot\boldsymbol{n}^m\right] \mathrm{d}^2\boldsymbol{x} \\ &\quad + \int_{S}^{PV} \left(1-\frac{1}{\varepsilon}\right) E_{\boldsymbol{n}}(\boldsymbol{x})\boldsymbol{T}(\boldsymbol{x}-\boldsymbol{x}^m)\cdot\boldsymbol{n}^m\,\mathrm{d}^2\boldsymbol{x},\end{aligned} \tag{3.11}$$

with $E^m_{\boldsymbol{n}} := E_{\boldsymbol{n}}(\boldsymbol{x}^m)$ and $\boldsymbol{n}^m := \boldsymbol{n}(\boldsymbol{x}^m)$. As in the previous section, before entering the series approximation (3.9) into the boundary integral equation, we simplify our notation by defining the following integrals:

$$A^m := \int_{S_E}^{PV} \varphi(\boldsymbol{x})\,T_{\boldsymbol{n}}(\boldsymbol{x}-\boldsymbol{x}^m)\,\mathrm{d}^2\boldsymbol{x} \tag{3.12a}$$

$$B^m := \int_{S}^{PV} \varphi(\boldsymbol{x})\boldsymbol{\Pi}_{\boldsymbol{n}}(\boldsymbol{x}-\boldsymbol{x}^m)\cdot\boldsymbol{n}^m\,\mathrm{d}^2\boldsymbol{x} \tag{3.12b}$$

$$C^{mn} := \int_{S_E}^{PV} \psi^n(\boldsymbol{x})G(\boldsymbol{x}-\boldsymbol{x}^m)\,\mathrm{d}^2\boldsymbol{x} \tag{3.12c}$$

$$D^{mn} := \int_{S} \psi^n(\boldsymbol{x})G(\boldsymbol{x}-\boldsymbol{x}^m)\,\mathrm{d}^2\boldsymbol{x} \tag{3.12d}$$

$$E^{mn} := \int_{S_E} \psi^n(\boldsymbol{x})\boldsymbol{T}(\boldsymbol{x}-\boldsymbol{x}^m)\cdot\boldsymbol{n}^m\,\mathrm{d}^2\boldsymbol{x} \tag{3.12e}$$

$$F^{mn} := \int_{S}^{PV} \psi^n(\boldsymbol{x})\boldsymbol{T}(\boldsymbol{x}-\boldsymbol{x}^m)\cdot\boldsymbol{n}^m\,\mathrm{d}^2\boldsymbol{x} \tag{3.12f}$$

With these integrals, we express equations (3.10) and (3.11) as

$$\frac{1}{2}\varphi^m = A^m + \sum_{n\in N_{S_E}} C^{mn}\cdot E^n_{\boldsymbol{n}} + \left(1-\frac{1}{\varepsilon}\right)\sum_{n\in N_S} D^{mn}\cdot E^n_{\boldsymbol{n}}, \tag{3.13a}$$

$$\frac{1}{2}\left(1+\frac{1}{\varepsilon}\right)E^m_{\boldsymbol{n}} = B^m + \sum_{n\in N_{S_E}} E^{mn}\cdot E^n_{\boldsymbol{n}} + \left(1-\frac{1}{\varepsilon}\right)\sum_{n\in N_S} F^{mn}\cdot E^n_{\boldsymbol{n}}, \tag{3.13b}$$

with $\varphi^m := \varphi(\boldsymbol{x}^m)$, and N_{S_E} and N_S the sets of all n with $\boldsymbol{x}^n \in S_E$ and S, respectively. For the N degrees of freedom $E^n_{\boldsymbol{n}}$, equations (3.13a) and (3.13b) define N linear equations. Like for the linear system in Section 3.1.1, we write this system as a matrix-vector-equation and solve it using the GMRES algorithm.

3.3 Mesh and Surface Representation

The surface of the microchannel geometry S_B and droplet S is defined by a set of vertices, and quadrilateral cells between them. Each mesh cell is defined by its four corner vertices and an interpolation rule for the surface between those corners. The interpolation is a mapping from a two-dimensional reference element, $(a,b)\in[0,1]\times[0,1]$, where the corners map to the four corner vertices. One such interpolation is the bilinear mapping,

$$\boldsymbol{x}_b(a,b) := (1-a)(1-b)\boldsymbol{v}_0 + a(1-b)\boldsymbol{v}_1 + (1-a)b\boldsymbol{v}_2 + ab\boldsymbol{v}_3, \tag{3.14}$$

with $\boldsymbol{v}_{i_c}$ ($i_c = 0..3$) the corner vertices, locally numbered in the order shown in Figure 3.1a. For representing the droplet surface, we use a more elaborate, smooth surface representation, which we discuss in Section 3.4.

The basis functions ψ^n for the degrees of freedom $\vec{g}$ of the Stokes- and electrostatic solution use the same bilinear interpolation on each cell. With g_{i_c} the local degree of freedom on cell

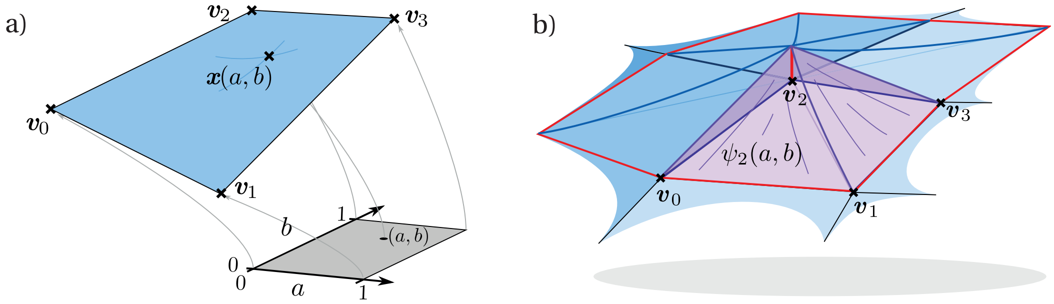

Figure 3.1: Mesh representation with quadrilateral cells. *a)* For each cell, there is a mapping $\boldsymbol{x}(a,b)$ which maps coordinates on the unit element $[0,1]\times[0,1]$ to the surface. The corners of the unit element are mapped to the mesh vertices. *b)* The bilinear basis function ψ^n spans all cells adjacent to a vertex $\boldsymbol{v}^n$. Consequently, a mesh cell hosts four basis functions ψ_{i_c}, one for each corner.

corner i_c, the interpolated value at $\boldsymbol{x}(a,b)$ on the cell is

$$g(a,b) = \psi_0(a,b)g_0 + \psi_1(a,b)g_1 + \psi_2(a,b)g_2 + \psi_3(a,b)g_3, \tag{3.15}$$

with

$$\psi_0(a,b) := (1-a)(1-b) \qquad \psi_1(a,b) := a(1-b)$$
$$\psi_2(a,b) := (1-a)b \qquad \psi_3(a,b) := ab.$$

The basis function ψ^n is constructed from one local basis function ψ_{i_c} on each cell adjacent to the global vertex $\boldsymbol{v}^n$ (Figure 3.1b).

3.3.1 Local Refinement

The accuracy of the numerical solution depends on the resolution of the mesh, which is inverse to the size of the mesh cells. With smaller mesh cells, the approximation of the solution $\boldsymbol{g}(\boldsymbol{x})$ by a finite number of scalar coefficients $\vec{g}$ (eq. 3.2) is more accurate. To minimize computational cost, we use a local mesh refinement, which increases the mesh resolution in places where either the solution or the surface shape vary quickly. These locations include narrow gaps, for example between a confined droplet in a microchannel and the channel wall, where even small variations in the gap width modify the lubrication flow. Other examples are interfaces with high curvature, where strong surface stresses require an accurate representation of surface shape and curvature.

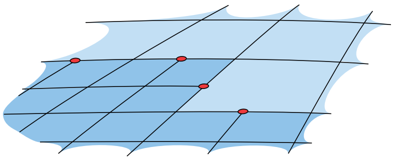

Figure 3.2: The mesh is refined locally by splitting cells. *Hanging nodes* (highlighted) appear between regions of different refinement level and need to be treated with care.

We refine the mesh locally by splitting a parent cell into four daughter cells. This local process leaves the global mesh topology untouched. Iterative refinement creates a quadtree-like hierarchical mesh structure, which can be reversed if lower resolution is sufficient. A downside of the approach is that *hanging nodes* are created between regions of different refinement level, which lie on the corner of two neighbor cells, but on the edge of a third (Figure 3.2). To ensure continuity of the solution $\boldsymbol{g}$, we constrain the degree(s) of freedom g^n (or g_i^n) to a linear interpolation between the values on the end of the edge.

3.3.2 Treatment of Edges

Microchannels S_B and electrodes S_E often have edges and corners, on which the boundary is not smooth. These features can be well represented by the quadrilateral mesh, but pose a problem to the discretized equations, which require smooth boundaries and a well-defined normal vector on the mesh nodes.

In a first step, we establish a well-defined normal vector by meshing the two faces adjacent to the edge separately, with coinciding vertices but separate degrees of freedom for either face (Figure 3.3). Then, we constrain the degrees of freedom on the edge to a linear extrapolation of corresponding values at two nodes inward from the edge. This reduces the effective resolution of the mesh close to edges and corners, but leads to a well-determined system of equations, with a lower number of degrees of freedom to solve.

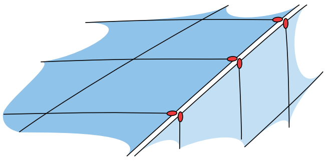

Figure 3.3: On edges and corners, vertices of different faces coincide. The degrees of freedom are constrained to their respective neighboring inward nodes' values.

3.3.3 Constraining Degrees of Freedom

The constraints on the degrees of freedom on hanging nodes (Section 3.3.1), edges and corners (Section 3.3.2) are implemented when setting up the linear system of matrix $\hat{\boldsymbol{A}}$ and right hand side $\vec{R}$ (eq. 3.8). Each constraint is a linear relation between just two or three degrees of freedom, which creates a sparse line in the matrix $\hat{\boldsymbol{A}}$. We eliminate the affected line and corresponding column from the linear system. This reduces the size of the system and speeds up the solution. After solving the linear system, the constrained degree of freedom is added again to the solution vector $\vec{g}$.

3.4 Smooth Surface Representation

The bilinear interpolation $\boldsymbol{x}_b$ that we use on the outer surfaces of the microchannel S_B and electrodes S_E is a poor choice for the droplet surface S: The planar faces of the cells will usually meet at an angle, such that neither the normal vectors nor the surface curvature are well-defined at the vertices, which are our collocation points. For this reason, surfaces are often represented through higher-order interpolation schemes with more degrees of freedom, more complex surface descriptions like the description with non-uniform rational B-splines [Heltai et al., 2014], or interpolate curvature and normal vectors from multiple neighboring cells [Zinchenko et al., 1997].

In this section, we present a novel interpolation scheme that is **independent of the chosen frame of reference**, gives a **continuous** surface that goes through all mesh points, and is **smooth** inside the cells and at the vertices (though not on the edges). Unlike with other traditionally used representations, this allows us to directly evaluate the mean curvature and normal direction from the representation.

Creating the representation consists of three steps: First, we define normal vectors at the mesh vertices (Section 3.4.1). Then, in a local coordinate system defined by the normal vector and two in-plane directions, we fit a paraboloid through the neighbor vertices (Section 3.4.2). These first two steps are performed before the surface integration. In a third step, we use the precomputed values on the vertices to interpolate the surface on each cell (Section 3.4.3).

3.4.1 Approximating the Normal Vector

We determine an initial guess for the normal vector $\boldsymbol{n}$ at vertex $\boldsymbol{v}$ from all cells adjacent to $\boldsymbol{v}$. Consider all cells C_j that have vertex $\boldsymbol{v}$ as a corner (with $j = 1..n_C$, n_C the number of such cells). Let $\boldsymbol{e}_j^{l,r}$ be the (left and right) edge vectors in the cell C_j and $\boldsymbol{d}_j$ the diagonal vector, all starting from vertex $\boldsymbol{v}$. For cell C_j, we define a local normal vector at the corner vertex $\boldsymbol{v}$ as

$$\boldsymbol{n}_j := \boldsymbol{e}_j^r \times \boldsymbol{e}_j^l \tag{3.16}$$

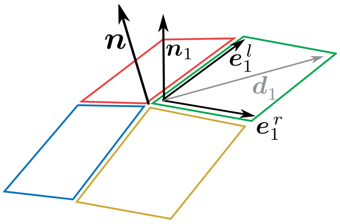

Figure 3.4: The normal vector $\boldsymbol{n}$ is constructed from the normal vectors of all adjacent cells.

The direction of the normal vector is then calculated as a weighted average of the cells' unit normal vectors with weight w_j,

$$\boldsymbol{n} := \sum_j w_j \hat{\boldsymbol{n}}_j, \tag{3.17}$$

with the weight

$$w_j := \frac{1}{\sqrt{|\boldsymbol{n}_j|}} \tag{3.18}$$

to give larger weight to cells of smaller diameter. The hat ($\hat{\boldsymbol{n}}_j$) refers to the normalized vector, $\hat{\boldsymbol{n}}_j := \frac{\boldsymbol{n}_j}{|\boldsymbol{n}|_j}$. The normalized vector $\hat{\boldsymbol{n}}$ is then used as an initial guess for the normal vector at $\boldsymbol{v}$.

Creating the Local Coordinate System

Based on the normal direction $\hat{\boldsymbol{n}}$, we now create a local coordinate system at $\boldsymbol{v}$ by defining

$$\begin{aligned}
\boldsymbol{a}_1 &:= \boldsymbol{e}_1^r && \text{(a vector not pointing along } \boldsymbol{n}\text{),}\\
\boldsymbol{e}_x &:= \boldsymbol{a}_1 - (\boldsymbol{a}_1 \cdot \hat{\boldsymbol{n}})\hat{\boldsymbol{n}} && \text{(a vector perpendicular to } \boldsymbol{n}\text{), and}\\
\boldsymbol{e}_y &:= \hat{\boldsymbol{n}} \times \boldsymbol{e}_x && \text{(a unit vector perpendicular to } \boldsymbol{n} \text{ and } \boldsymbol{e}_x\text{).}
\end{aligned}$$

The unit vectors $(\hat{\boldsymbol{e}}_x, \hat{\boldsymbol{e}}_y, \hat{\boldsymbol{n}})$ span a right-handed coordinate system.

3.4.2 Locally Fitting a Paraboloid

In the local coordinate system $(\hat{\boldsymbol{e}}_x, \hat{\boldsymbol{e}}_y, \hat{\boldsymbol{n}})$ centered at $\boldsymbol{v}$, we fit a paraboloid of the form

$$z(x, y) = \alpha x^2 + \beta y^2 + \gamma xy + \delta x + \varepsilon y \tag{3.19}$$

through the set of neighbor vectors,

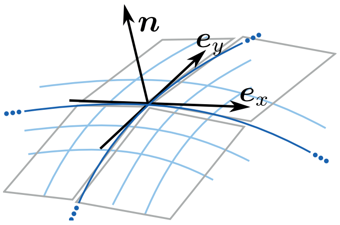

Figure 3.5: At each vertex $\boldsymbol{v}$, the surface locally resembles a paraboloid, with the precomputed normal $\boldsymbol{n}$ and coefficients that minimize the surface's distance to all neighbor vertices.

$$\boldsymbol{N} := \{\boldsymbol{e}_1^l, \boldsymbol{e}_1^r, \boldsymbol{d}_1, \boldsymbol{e}_2^l, \boldsymbol{e}_2^r, \boldsymbol{d}_2, \ldots, \boldsymbol{d}_{n_C}\}, \tag{3.20}$$

which point from vertex $\boldsymbol{v}$ to all its direct and diagonal neighbors. Edge vectors typically appear twice in the list, as they are parts of two neighbor cells. The local coordinates of neighbor $\boldsymbol{a}_k \in \boldsymbol{N}$ are given by $(x_k, y_k, z_k) = (\boldsymbol{a}_k \cdot \hat{\boldsymbol{e}}_x, \boldsymbol{a}_k \cdot \hat{\boldsymbol{e}}_y, \boldsymbol{a}_k \cdot \hat{\boldsymbol{n}})$. For these neighbors, we write the paraboloid equation (3.19) as

$$w_k \cdot \begin{pmatrix} x_k^2 & y_k^2 & x_k y_k & x_k & y_k \end{pmatrix} \cdot \begin{pmatrix} \alpha \\ \beta \\ \gamma \\ \delta \\ \varepsilon \end{pmatrix} = w_k z_k, \tag{3.21}$$

with $w_k > 0$. With 5 degrees of freedom $(\alpha, \beta, \gamma, \delta, \varepsilon)$, but usually 9-12 equations, the system is overdetermined. We therefore solve the system in a least-squares sense. The relative weight of each row is determined by the factor

$$w_k = \begin{cases} \frac{1}{x_k^2 + y_k^2} & \text{for edges } \boldsymbol{a}_k = \boldsymbol{e}^{l,r} \\ \frac{0.1}{(x_k^2 + y_k^2)} & \text{for diagonals } \boldsymbol{a}_k = \boldsymbol{d}, \end{cases} \tag{3.22}$$

which gives a high weight to nearby neighbors. We write (3.21) for all k as a linear system $\hat{\boldsymbol{P}} \cdot \boldsymbol{\alpha} = \boldsymbol{b}$ for the coefficient vector $\boldsymbol{\alpha} := (\alpha, \beta, \gamma, \delta, \varepsilon)$. The least-squares solution to this linear system is given by [Bronstein et al., 2008, p. 317f]

$$\boldsymbol{\alpha} = (\hat{\boldsymbol{P}}^T \cdot \hat{\boldsymbol{P}})^{-1} \cdot (\hat{\boldsymbol{P}}^T \cdot \boldsymbol{b}). \tag{3.23}$$

We invert the 5×5-matrix $(\hat{\boldsymbol{P}}^T \cdot \hat{\boldsymbol{P}})$ with a direct method. The position of a point on the paraboloid, seen in the global coordinate system, is then given by

$$\boldsymbol{x} = \boldsymbol{v} + x\hat{\boldsymbol{e}}_x + y\hat{\boldsymbol{e}}_y + (\alpha x^2 + \beta y^2 + \gamma x y + \delta x + \varepsilon y)\hat{\boldsymbol{n}}. \tag{3.24}$$

Re-Estimating the Normal Vector

The surface normal of the fitted paraboloid (3.24) does not necessarily coincide with the vector $\hat{\boldsymbol{n}}$ of the local coordinate system. We calculate the local surface normal

$$\boldsymbol{n}^* := \hat{\boldsymbol{n}} - \delta\hat{\boldsymbol{e}}_x - \varepsilon\hat{\boldsymbol{e}}_y \tag{3.25}$$

as a new guess for the surface normal at $\boldsymbol{v}$. Based on this new guess for the normal vector, we fit the paraboloid surface a second time. By setting the coefficients $\delta = \varepsilon = 0$, we ensure that the surface normal is aligned with the normal of the local coordinate system. The accuracy of this approach is shown in Section 3.4.4 (Figure 3.6).

3.4.3 Interpolating Between Corner Vertices of a Cell

From the surface shape at each of the four corner vertices $\boldsymbol{v}_i$ $(i = 0..3)$ of a cell, we interpolate the surface on the cell. This happens in three steps: First we create an initial guess for the point by bilinear interpolation. Then we project that initial guess onto the paraboloid surfaces of each corner vertex. From the four projections, we finally interpolate the surface position.

With $(a, b) \in [0,1] \times [0,1]$ the coordinates on the reference element, we use the bilinear interpolation (3.14) to get the point $\boldsymbol{x}_b$, which is an initial guess for the surface location. We project this point to the x-y-plane of each of the corner vertices' local coordinate systems $(\hat{\boldsymbol{e}}_{x,i}, \hat{\boldsymbol{e}}_{y,i}, \hat{\boldsymbol{n}}_i)$, and calculate the z-position on the local paraboloid. The point's position $\boldsymbol{x}_i$ on the paraboloid of $\boldsymbol{v}_i$ is calculated as

$$\begin{aligned} x_i &:= (\boldsymbol{x}_b - \boldsymbol{v}_i) \cdot \hat{\boldsymbol{e}}_{x,i} \\ y_i &:= (\boldsymbol{x}_b - \boldsymbol{v}_i) \cdot \hat{\boldsymbol{e}}_{y,i} \\ \Rightarrow \boldsymbol{x}_i &:= \boldsymbol{v}_i + x_i \hat{\boldsymbol{e}}_{x,i} + y_i \hat{\boldsymbol{e}}_{y,i} + (\alpha_i x_i^2 + \beta_i y_i^2 + \gamma_i x_i y_i) \hat{\boldsymbol{n}}_i \end{aligned} \tag{3.26}$$

To interpolate between the values $\boldsymbol{x}_i$, we use the third-order polynomials

$$\psi_0(a) = 1 - 3a^2 + 2a^3, \tag{3.27a}$$

$$\psi_1(a) = 3a^2 - 2a^3, \tag{3.27b}$$

to get the final expression for the surface location,

$$\boldsymbol{x}(a, b) := \psi_0(a)\psi_0(b)\boldsymbol{x}_0 + \psi_1(a)\psi_0(b)\boldsymbol{x}_1 + \psi_0(a)\psi_1(b)\boldsymbol{x}_2 + \psi_1(a)\psi_1(b)\boldsymbol{x}_3. \tag{3.28}$$

3.4.4 Properties of the Representation

The interpolation scheme has several properties that are relevant to its application. The surface representation is **independent of the reference frame**, as the local coordinate points $\boldsymbol{x}_i$ are found from the bilinear interpolation (which itself does not depend on the chosen reference frame) and we have $\psi_0(a) + \psi_1(a) = 1$.

The representation is **continuous** from one cell to the next, since the $\boldsymbol{x}_b$ are continuous, the local paraboloid of the vertex $\boldsymbol{v}_i$ is shared between neighboring cells, and the position on the cell's edge ($a = 0, 1$ or $b = 0, 1$) only depends on the end vertices of that edge because

$$\psi_1(0) = \psi_0(1) = 0 \quad \text{and} \quad \psi_0(0) = \psi_1(1) = 1. \tag{3.29}$$

Note here that the representation is not necessarily continuous for a partially refined mesh, where the location of hanging nodes can be fixed to lie on the surface of the adjacent larger cell, but the interpolation along the edge may vary across the cell boundary.

The representation is **smooth** in the interior of the cell, and also at the vertices, where the surface is perpendicular to the vertex normal $\hat{\boldsymbol{n}}_i$, and where we have

$$\psi_0'(a)\big|_{a=0,1} = \psi_1'(a)\big|_{a=0,1} = 0, \tag{3.30}$$

such that the surface normal of the interpolation (3.28) is that of the local paraboloid. The representation is not necessarily smooth on the edge of the cells: The normal on the edge is defined by the tangent vectors. While the tangent vector along the edge will be the same on both sides, the tangent perpendicular to the edge does depend on the other two vertices of each cell. At higher refinement, the discontinuity in the normal vector goes to zero.

For the interpolation (3.28), there are direct expressions for the Jacobian of the mapping, the local surface normal vector, and the mean curvature. These expressions are given in Appendix A.

Accuracy of the Representation

We estimate the accuracy of the smooth surface representation by representing a sphere of radius R by a mesh of n_v vertices. We quantify the deviation of the surface shape from an ideal sphere by the relative shape error

$$\varepsilon_{\boldsymbol{x}} := \left\langle \left(\frac{|\boldsymbol{x}| - R}{R} \right)^2 \right\rangle_S^{1/2},$$

with the average over the sphere surface S defined as $\langle \ldots \rangle_S := \frac{1}{A} \int_S (\ldots)\, \mathrm{d}^2\boldsymbol{x}$. From the surface shape, we calculate the volume of the sphere (Section 2.4.1). The relative error of the volume is

$$\varepsilon_V := \frac{|V - V_\mathrm{sphere}|}{V_\mathrm{sphere}},$$

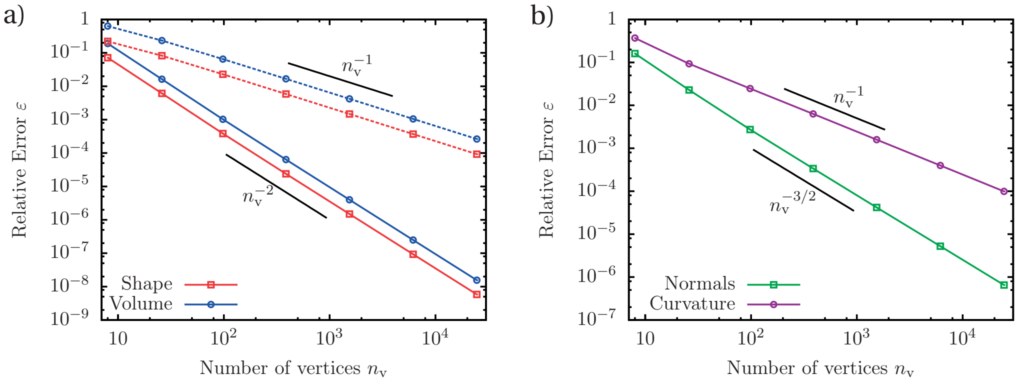

Figure 3.6: Accuracy of the smooth surface representation, for a sphere of unity radius represented by a mesh of n_v vertices. a) Relative errors for the surface position $\varepsilon_{\boldsymbol{x}}$ and volume ε_V. Dashed lines show the errors for the bilinear surface representation. b) Relative errors for the surface normals $\varepsilon_{\boldsymbol{n}}$ and mean curvature ε_κ.

with $V_{\text{sphere}} := \frac{4\pi}{3} R^3$. We find that both the shape error $\varepsilon_{\boldsymbol{x}}$ and the volume error ε_V converge quadratically with the number of vertices, which is one convergence order faster than the bilinear interpolation (Figure 3.6a). Figure 3.7 shows the different surface representations of the mesh, and the local error of the surface shape.

In the numerical scheme, the surface normals $\boldsymbol{n}$ and surface curvature κ determine the surface stresses, particularly the Young-Laplace stress due to surface tension. We quantify the relative error of normal orientation and curvature by

$$\varepsilon_\kappa := \left\langle \left(\frac{\kappa - \kappa_{\text{sphere}}}{\kappa_{\text{sphere}}} \right)^2 \right\rangle_S^{1/2} \qquad \text{and} \qquad \varepsilon_{\boldsymbol{n}} := \left\langle \| \boldsymbol{n} - \boldsymbol{e}_r \|^2 \right\rangle_S^{1/2},$$

with $\kappa_{\text{sphere}} := 1/R$ and $\boldsymbol{e}_r$ a unit vector in radial direction. We find that the errors converge quickly to zero, with the normal direction having a somewhat smaller error than the curvature (Figure 3.6b).

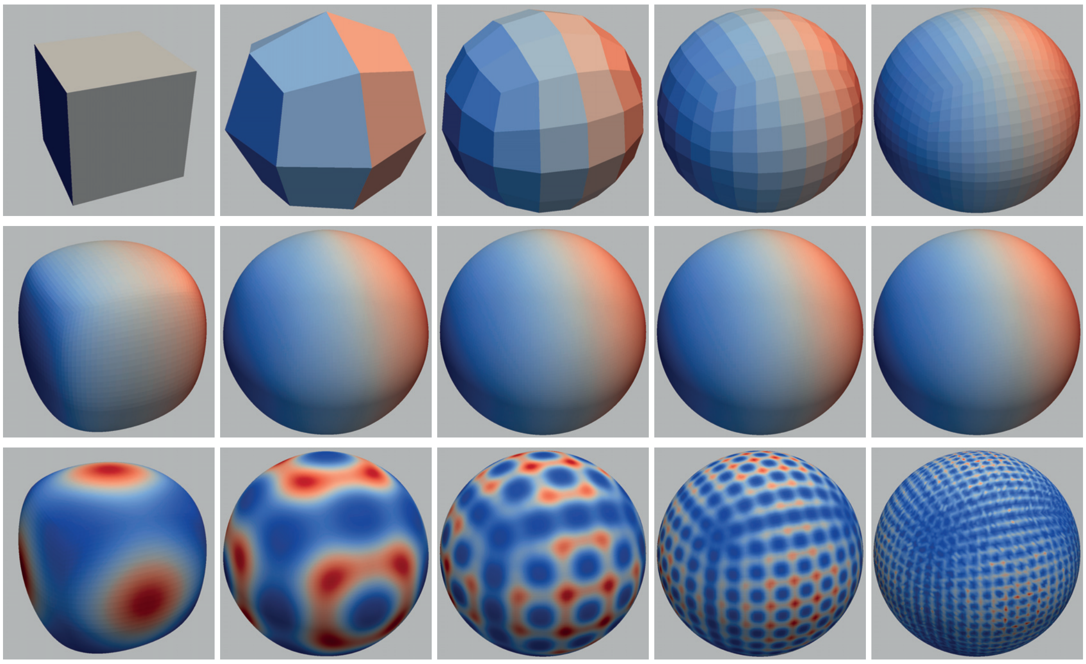

Figure 3.7: Representation of a spherical surface, at different stages of refinement. While the vertices lie on a sphere, the surface between them is constructed locally and with no assumptions about the global geometric shape. *Top:* Surfaces constructed from a bilinear interpolation between the mesh points, with colors denoting surface orientation. *Middle:* Surfaces constructed from the smooth surface representation, with colors denoting surface orientation. *Bottom:* Surfaces constructed from the smooth surface representation. The color scheme marks the deviation of the surface shape from an ideal sphere. The maximum error of the representation (red) ranges from $1.8 \cdot 10^{-2}$ (at $n_{\text{v}} = 6$) to $1.1 \cdot 10^{-11}$ (at $n_{\text{v}} = 1538$).

3.5 Numerical Integration

The boundary integrals that appear in the discretized equations cannot be solved analytically. We use numerical quadrature, which expresses each integral as a sum over a finite number of points.

Quadrature rules are defined on the reference element $[0,1]\times[0,1]$. A quadrature is given by a set of n_{qp} quadrature points $\vec{q}_i \in [0,1]\times[0,1]$ and associated weights $w_i \in [0,1]$, with $\sum_i w_i = 1$ [Engels, 1980]. With $\boldsymbol{x}(a,b)$ the mapping from the reference element to cell C, the integral over the integrand $f(\boldsymbol{x})$ is approximated by

$$\int_C f(\boldsymbol{x})\,\mathrm{d}^2\boldsymbol{x} \simeq \sum_{i=1}^{n_{qp}} f(\boldsymbol{x}_i)\cdot J_i \cdot w_i, \tag{3.31}$$

where $\boldsymbol{x}_i := \boldsymbol{x}(\vec{q}_i)$ is the surface position of the ith quadrature point, and

$$J_i := \left\| \frac{\partial \boldsymbol{x}}{\partial a} \times \frac{\partial \boldsymbol{x}}{\partial b} \right\|_{(a,b)=\vec{q}_i} \tag{3.32}$$

is the Jacobian of the mapping from the reference element.

We use Gauss-Legendre quadrature, which defines quadrature points $\vec{q}_i$ and weights w_i such that expression (3.31) is exact for integrating polynomials up to a certain order. In each dimension, N quadrature points are sufficient to exactly represent a polynomial of order $2N-1$. A quadrature of order N has $n_{qp} = N^2$ quadrature points.

3.5.1 Nearly Singular Integration

Both the integrand $f(\boldsymbol{x})$ and the mapping $\boldsymbol{x}(a,b)$ are typically smooth, so that they can be well approximated by polynomials, and the Gauss-Legendre quadrature yields accurate results even at a moderate number of quadrature points. This is not the case for the singular (or nearly singular) integrals, which appear in the Boundary Element formulation when the integration variable $\boldsymbol{x}$ passes a collocation point $\boldsymbol{x}^m$. Here the integrand diverges, and cannot be described even by high order polynomials.

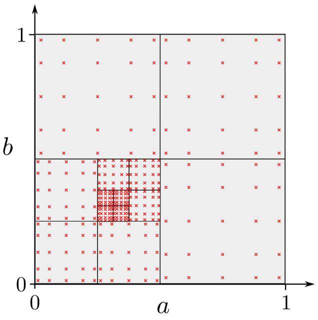

Figure 3.8: Quadrature formula for nearly singular integration, based on a Gauss-Legendre formula with $N=5$.

For singular integrals, we use a quadrature rule that removes one factor $1/r$ from the integration by integrating in polar coordinates. This renders integrals over the Stokeslet (2.7) and electrostatic Green's function (2.33) regular. For the stresslet (2.10) and normal derivative of the electrostatic Green's function (2.36a), a singularity with $1/r$ remains, which we evaluate with high-accuracy Gauss quadrature.

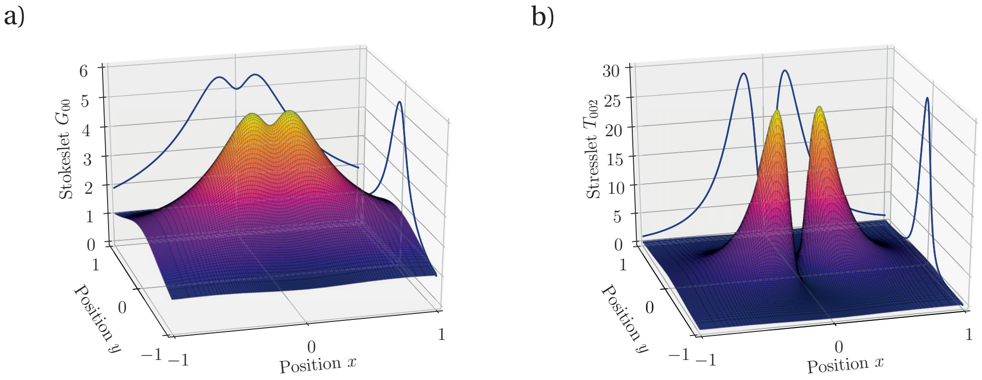

Figure 3.9: Magnitude of Stokeslet and stresslet in the x-y-plane, for a source at $\boldsymbol{x}_0 := (0,0,a)$, with $a = 0.2$. The amplitude of the peaks diverges for $a \to 0$, which makes accurate integration increasingly difficult. *a)* Magnitude of the Stokeslet component G_{00}. *b)* Magnitude of the stresslet component T_{002}.

For nearly singular integrals, which typically appear when two surfaces of the geometry come close, we subdivide the cell and perform Gauss-Legendre integration on the subdomains (Figure 3.8). This strongly increases the number of quadrature points, but since nearly singular quadrature is only required on a small number of cells and for few degrees of freedom, the overall impact on runtime is small.

3.5.2 Accuracy of the Numerical Quadrature

We investigate the accuracy of the numerical quadrature by comparing the numerical integral to the analytical result from integrating the Stokeslet and stresslet Green's functions over a simple unit cell $[0,1] \times [0,1]$. With the integration domain of unit length scale, the accuracy of the integration depends on the parameter a, which is the distance between the unit cell and the Green's functions' origin $\boldsymbol{x}_0$. In the boundary integral equations, the Green's functions are modulated by shape functions and the mapping from the reference cell onto the boundary, but the divergence behavior of the Stokeslet and stresslet dominates the quadrature error. Figure 3.9 shows the magnitude of two components of the Stokeslet and stresslet, at parameters at which they are nearly singular.

Stokeslet

The Stokeslet (defined in Section 2.1, eq. 2.7) has the form

$$G_{ij}(\boldsymbol{r}) = \frac{\delta_{ij}}{|\boldsymbol{r}|} + \frac{r_i r_j}{|\boldsymbol{r}|^3}, \tag{3.33}$$

with vector $\boldsymbol{r} := \boldsymbol{x} - \boldsymbol{x}_0$ describing the relative distance between a point $\boldsymbol{x}$ and the Stokeslet source $\boldsymbol{x}_0$. The singularity for $|\boldsymbol{r}| \to 0$ diverges with $|\boldsymbol{r}|^{-1}$. For $\boldsymbol{x} := (x, y, 0)$ on a unit element

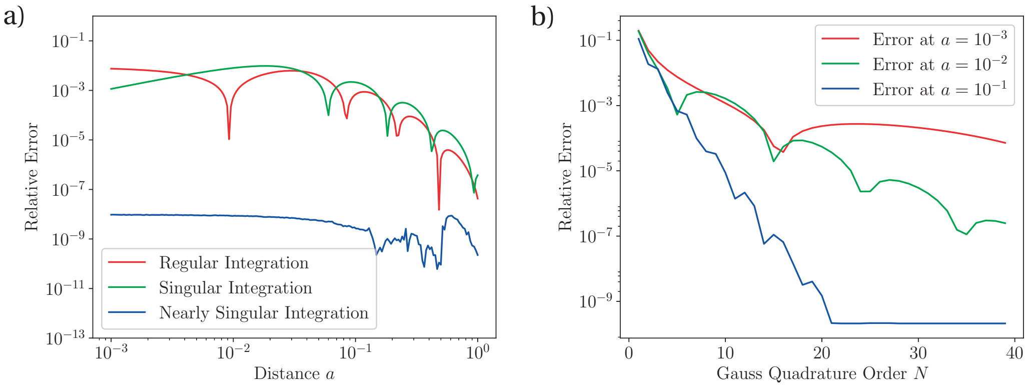

Figure 3.10: Integration accuracy for the Stokeslet. *a)* Relative error of the numerical quadrature at quadrature order $N = 5$, against the distance a between Stokeslet and integration domain. *b)* Relative error of the Gauss-Legendre quadrature for varying integration order N, at fixed distance a. The numerical integration result fluctuates around the analytic value for the integral, creating spikes in the data when the error vanishes. The iterative refinement of the nearly singular integration creates a periodic pattern that stays below an error of 10^{-6}.

$E := [0,1] \times [0,1]$ in the x-y-plane, we evaluate the Stokeslet relative to the point $\boldsymbol{x}_0 := (0,0,a)$. We perform the quadrature for the integral

$$I_G := \iint_E G_{00}(\boldsymbol{x} - \boldsymbol{x}_0)\,\mathrm{d}x\,\mathrm{d}y, \tag{3.34}$$

which has the analytical solution

$$\begin{aligned} I_G &= \int_0^1 \int_0^1 \frac{1}{(x^2+y^2+a^2)^{1/2}} + \frac{x^2}{(x^2+y^2+a^2)^{3/2}}\,\mathrm{d}x\,\mathrm{d}y \\ &= \log\left(\frac{1+\sqrt{2+a^2}}{\sqrt{1+a^2}}\right) + 2\sinh^{-1}\left(\frac{1}{\sqrt{1+a^2}}\right) - 2a\cdot\tan^{-1}\left(\frac{1}{a\sqrt{2+a^2}}\right). \end{aligned}$$

For $a \ll 1$, the integration formulas for Gauss-Legendre and singular quadrature have an increasingly large error, whereas the error of the nearly singular integration formula stays at 10^{-8} (Figure 3.10a). This increased accuracy is at the cost of a higher number of quadrature points, with $n_{qp} = \mathcal{O}(10^3)$ for the nearly singular integration at small a (compared to $n_{qp} = 25$ for the Gauss-Legendre quadrature). Increasing the order of the regular Gauss-Legendre quadrature successfully decreases the error at larger a, but fails to do so at small a (Figure 3.10b). Around $a = \mathcal{O}(10^{-2})$, nearly singular quadrature uses less quadrature points than high-order Gauss-Legendre quadrature to reach the same integration accuracy,

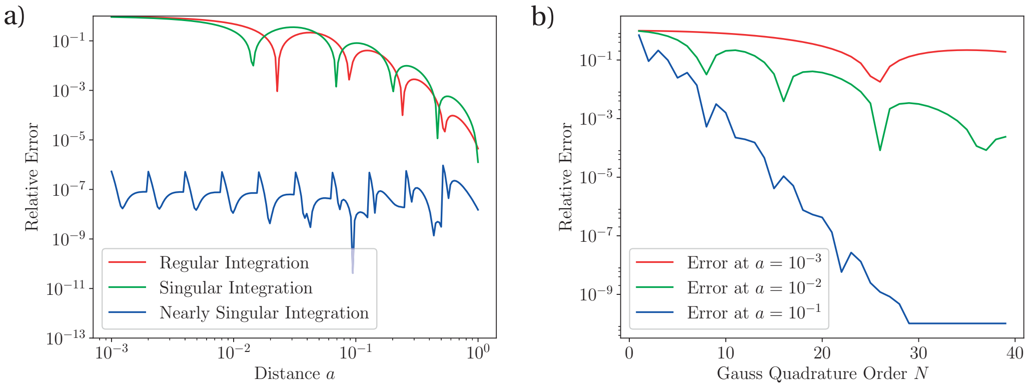

Figure 3.11: Integration accuracy for the stresslet. *a)* Relative error of the numerical quadrature at quadrature order $N = 5$, against the distance a between stresslet and integration domain. *b)* Relative error of the Gauss-Legendre quadrature for varying integration order N, at fixed distance a.

Stresslet

The stresslet (defined in Section 2.1, eq. 2.10) is

$$T_{ijk}(\boldsymbol{r}) = -6\frac{r_i r_j r_k}{|\boldsymbol{r}|^5}, \tag{3.35}$$

with the singularity for $|\boldsymbol{r}| \to 0$ diverging with $|\boldsymbol{r}|^{-2}$. On the unit element E, we perform the quadrature for the integral

$$I_T := \iint_E T_{002}(\boldsymbol{x} - \boldsymbol{x}_0)\,\mathrm{d}x\,\mathrm{d}y. \tag{3.36}$$

This integral has the analytical solution

$$\begin{aligned} I_T &= \int_0^1 \int_0^1 \frac{6ax^2}{(x^2 + y^2 + a^2)^{5/2}}\,\mathrm{d}x\,\mathrm{d}y \\ &= 2\tan^{-1}\left(\frac{1}{a\sqrt{2 + a^2}}\right) - \frac{2a}{(1 + a^2)\sqrt{2 + a^2}}. \end{aligned}$$

The accuracy of the quadrature rules for small a (Figure 3.11a) and the convergence of Gauss-Legendre quadrature for large quadrature orders (Figure 3.11b) show the same characteristic behavior as for the Stokeslet. However, the error is larger by one order of magnitude. At $a < 10^{-1}$, the Gauss-Legendre integration typically has a relative error on the order of 10%. For the stresslet, using an appropriately high quadrature order and switching to the nearly singular integration formula is therefore even more important.

3.6 Time Stepping

From solving the boundary integral equations for Stokes flow (Section 3.1), we get the flow velocity $\boldsymbol{u}(\boldsymbol{x})$ on the droplet interface S. This flow velocity advects the interface, which deforms the droplet and leads to the nonlinear dynamics that we want to study. To simulate the advection and deformation of the droplet interface, we perform a forward time integration using the explicit Euler method.

At time t, the location of the interface S is defined by the positions of the interface vertices $\boldsymbol{v}_i^t$ and the mesh between them. Solving the boundary integral equations gives the instantaneous flow velocity $\boldsymbol{u}_i^t$ at these vertices. For a time step $\mathrm{d}t \ll 1$, the location of the interface vertex is then approximated by

$$\boldsymbol{v}_i^{t+\mathrm{d}t} \simeq \boldsymbol{v}_i^t + \mathrm{d}t \cdot \boldsymbol{u}_i^t. \tag{3.37}$$

After each such time step, we redistribute the vertices on the mesh to avoid mesh distortions (Section 3.6.2) before calculating the flow solution in this updated geometry. The resulting iterative simulation loop for the forward time integration is sketched in Figure 3.12. If the electrostatic solver is active, it is evaluated directly before the Stokes solver.

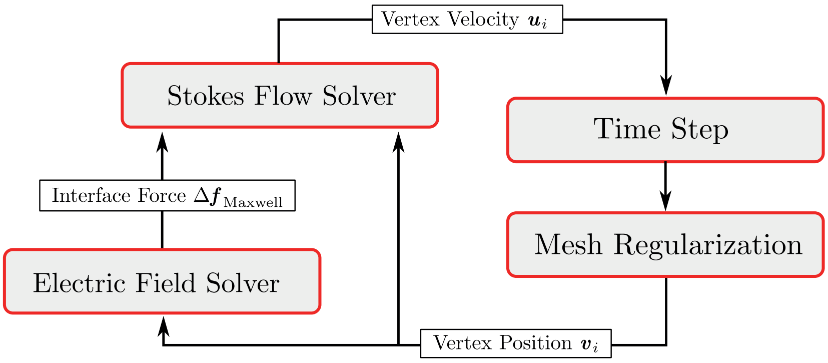
Vertex Velocity $\boldsymbol{u}_i$
Stokes Flow Solver
Time Step
Interface Force $\Delta \boldsymbol{f}_{\text{Maxwell}}$
Mesh Regularization
Electric Field Solver
Vertex Position $\boldsymbol{v}_i$

Figure 3.12: Loop for advancing the simulation forward in time: The vertex positions $\boldsymbol{v}_i$, together with the mesh between them, describe the system geometry. If an electrode is present in the system, the electric field solver (Section 3.2) calculates the surface field on the free interface, which determines the Maxwell stress. Using the mesh geometry and possibly the Maxwell stresses, the Stokes solver (Section 3.1) calculates the velocity $\boldsymbol{u}_i$ at the vertex positions $\boldsymbol{v}_i$. These vertex velocities determine the deformation of the free interface. The surface is first deformed, then mesh nodes are redistributed to avoid distorted cells (Section 3.6.2).

3.6.1 Stability of the Time Stepping

The explicit Euler scheme is unstable for large time steps. When the time steps are too large, small perturbations on the droplet surface grow, causing non-physical mesh distortions [Dai and Shelley, 1993; Nagel, 2014]. Perturbations grow because the surface tension forces, which normally smooth out capillary waves at small wavelength, cause an overshoot and amplification of surface distortions.

The restoring motion of a perturbed interface is driven by surface tension γ and slowed by fluid viscosity μ, giving a characteristic velocity scale $U_C := \frac{\gamma}{\mu}$ at which the interface returns to a planar shape. This characteristic velocity defines the ratio between the smallest mesh width in the geometry, $h_{\min}$, and the time step $\mathrm{d}t$, at which the time stepping method becomes unstable. We therefore adapt the time step to

$$\mathrm{d}t := \frac{\mu h_{\min}}{\gamma}. \tag{3.38}$$

This choice of time step renders the time stepping scheme stable, but requires a high temporal resolution, particularly at low capillary numbers. Higher order schemes like the Adams-Bashforth or Runge-Kutta scheme [Bronstein et al., 2008, pp. 975f] could alleviate the stability problem and allow for larger time steps. However, we found that in geometries with very narrow gaps, and together with the mesh stabilization and refinement algorithms, these solution algorithms did not give reliable results. An alternative approach to the stability problem would be adopting a mesh stabilization scheme like the one suggested by Nagel and Gallaire [2015]. In situations where the droplet reaches a steady shape, we accelerate the simulation by calculating the center-of-mass velocity of the droplet. We then translate the droplet according to this velocity vector, instead of moving each vertex with the local velocity.

3.6.2 Mesh Regularization

Advection of the droplet interface can lead to the distortion of mesh cells and an uneven mesh resolution. To maintain a regular mesh with an even spacing between adjacent vertices, we regularize the mesh after each time step. For each mesh vertex, we calculate a weighted average of its neighbor vertices, taking into account the different refinement levels of the neighbor cells. We project this mean vertex to the surface expressed by the surface representation. After finding such new vertex positions for all vertices on the droplet interface, we update the old vertex positions to these new coordinates, and repeat. The iteration ends if the L_2-norm of the vertex position increments drops below the threshold of $10^{-4}H$, with H the channel height that sets the characteristic length scale.

Since vertices are only moved on the surface, and usually only by small distances, this redistribution does not change the shape of the interface, and leads to a regular mesh. Typical alternative approaches, like the introduction of new mesh cells or local refinement, are more difficult to implement for the quadrilateral mesh that we use. After regularizing the mesh, we ensure that the hanging nodes are relocated to the center of their parent edge, and adjust the mesh resolution by coarsening or refining cells where necessary (Section 3.3.1). In regions where two boundaries are very close, we enforce a minimum distance of $10^{-2}H$ between the boundaries. This is to avoid singularities in the surface integrals (see Section 3.5.1) and mimics the effect of steric repulsion due to surfactants.

3.7 Implementation

The simulation was implemented in the programming language `C++`. The object-oriented code comprises 130 classes on 32 036 lines of code. The data structures for the mesh and its refinement, Gauss-Legendre integration rules and iterative GMRES-solver use the finite-element library `deal.ii` in version 8.3.0 by Bangerth et al. [2007, 2016]. The library `deal.ii` was originally designed for 2D and 3D finite-element simulations, but was versatile enough to be repurposed for solving the boundary integral equations on codimension-one manifolds.

For creating the mesh for the droplets and surrounding microchannel, we implemented an automated mesh generation algorithm. Complex microchannel or electrode geometries are represented with Bézier curves in the W3C `svg` standard [Dahlström et al., 2011], which is supported by common vector graphics editors. Output of the geometries and solutions uses the `vtk` file format. Snapshots of the runtime state are stored in binary files, from which a simulation can be continued.

The implementation uses `C++` templates for a possible extension to 2D flow. Besides the explicit Euler time stepping algorithm that we use in this work (Section 3.6), the Adams-Bashforth and 2nd order Runge-Kutta schemes are implemented. The two BEM solvers, `StokesSolver` and `ElectroSolver` (Sections 3.1 and 3.2), are encapsulated in separate classes and can be activated independently of each other (or coupled, as described in Section 3.6). The code is parallelized with MPI or multithreading, see Section 3.7.1. Correctness of the individual parts of the code is tested with a suite of unit tests.

3.7.1 Parallelization

While the computing power of a single processor core has not seen much speedup in recent years, new processor generations come with an ever increasing number of cores. For utilizing these increasing computational resources, we parallelized the most time-consuming sections of the code. Our parallelization based on the *Message Passing Interface* (MPI), which is commonly used on computing clusters. As a fallback option for single-processor machines when MPI is not available, we implemented `pthread`-based multithreading for parts of the code.

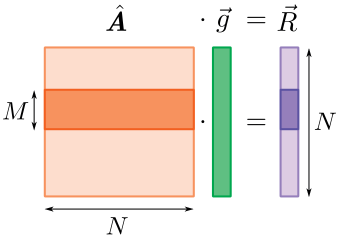

Figure 3.13: Calculating the linear system (3.8) is distributed between processes: Each process calculates and stores part of the matrix $\hat{\boldsymbol{A}}$ and residual $\vec{R}$.

The majority of computing time in the simulation is spent in calculating the matrix $\hat{\boldsymbol{A}}$ for the linear system, and solving this system. This holds both for the solver for electrostatics, and for the solver for Stokes flow. For each solver, at 10^4 degrees of freedom, calculating the system matrix (which is an $\mathcal{O}(N^2)$-operation in the number of degrees of freedom) and solving it iteratively with GMRES (which is $\mathcal{O}(N^2 \log N)$) takes a similar amount of time. We parallelized both of these steps.

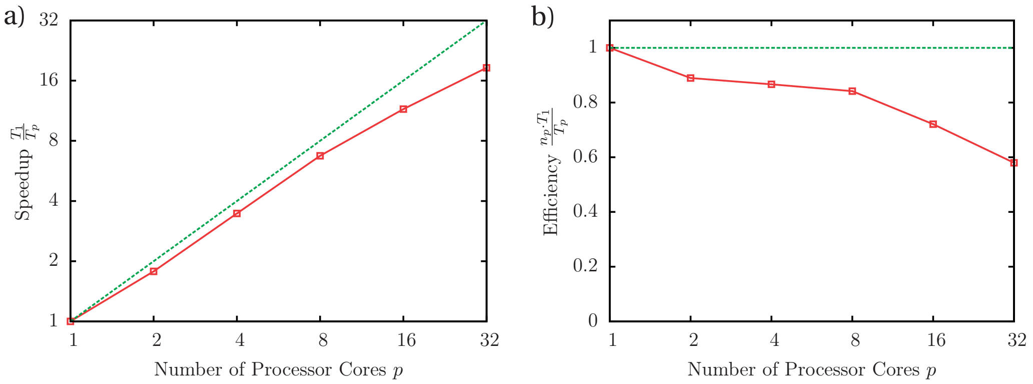

Figure 3.14: Scaling of the parallelization with the number of processor cores p, for a simulation of approximately 50 000 degrees of freedom. *a)* Speedup of using multiple cores. *b)* Efficiency per core when using multiple cores. Green dashed lines mark the linear speedup and the corresponding efficiency.

Since the boundary integral equations represent the 3D field by values on the 2D boundaries of the geometry, the memory required for storing the entire system geometry and solution vector is just on the order of 10 MB even for large systems of 10^5 degrees of freedom. Every process can therefore store the full simulation state in memory. In assembling the matrix $\hat{\boldsymbol{A}}$ and residual vector $\vec{R}$ for the linear system, every row of the matrix and entry of the solution vector corresponds to one degree of freedom m. Each process is assigned a fixed range of M degrees of freedom for which it computes the corresponding rows of the system matrix and residual entries (Figure 3.13). The $M \times N$-matrix of process-local rows of $\hat{\boldsymbol{A}}$ remains in local memory only, whereas the residual vector $\vec{R}$ is communicated to all processes.

The GMRES algorithm iterates over matrix-vector products with the system matrix $\hat{\boldsymbol{A}}$. In this iteration, every process computes a part of the matrix-vector product from its local $M \times N$-matrix. The result is broadcasted to all processes and the iteration continues. Other parts of the code, such as the computation of boundary integrals in the volume, are shared between processes in a similar fashion.

The parallelization requires little overhead work or communication, such that the speedup scales well with the number of cores (Figure 3.14). In the test we performed, the efficiency stays around 90% for up to 8 cores, and drops to 60% at 32 cores (where $M = \mathcal{O}(10^3)$ on each core). The number of cores does not have to be a power of two. With the changing number of degrees of freedom at each time step, we adapt the distribution of degrees of freedom across the cores.

3.8 Summary

We implemented a 3D boundary element scheme to simulate droplet dynamics in microchannels, under the effect of Young-Laplace surface tension, gravity and dielectric stresses on the interface. A particular focus lies on the representation of surfaces and surface integration: With an accurate representation of a smooth droplet surface, and a genuine way to determine the surface curvature needed to calculate the Young-Laplace stress, boundary integrals can be evaluated at high precision. In integration, we devote special attention to nearly singular integrals, where the integrand varies quickly an classical quadrature approaches fail. Time stepping uses an explicit low-order method, which requires a small time step. This limits the performance of the simulation. The implementation is parallelized, and scales well with the number of processor cores.

4 Code Validation

Contents

4.1 Flow Past a Moving Sphere . . . 60
4.2 Flow in a Cuboid Duct . . . 62
4.3 Sphere Moving Past a Plane Wall . . . 64
4.4 Droplet in Extension Flow . . . 65
4.5 Droplet in a Cylindrical Capillary . . . 66
4.6 Rising Droplet under Gravity . . . 69
4.7 Dielectric Sphere in a Uniform Electric Field . . . 70
4.8 Droplet in a Uniform Electric Field . . . 71
4.9 Summary . . . 74

To verify the correctness and determine the accuracy of our numerical code, we validate it against known results from analytic calculations and simulations.

The first three validation cases (Sections 4.1-4.3) test the numerical solver in systems with rigid boundaries. By calculating the flow field around a rigid sphere moving in quiescent flow (Section 4.1), we test the accuracy of the BEM scheme and the exterior solver for Dirichlet boundary conditions. Calculating the flow profile in a cuboid duct (Section 4.2) serves to test the combination of Dirichlet and Neumann boundary conditions, in particular for the mixed-type channel outlet. The drag force on a sphere that moves past a planar wall (Section 4.3) gives an estimate for the numerical accuracy of the solver in narrow gaps.

The next two validation cases introduce free surfaces, with the simple Young-Laplace surface tension model. By calculating the deformation of a droplet in an extensional flow (Section 4.4), we validate the surface tension model far from boundaries. Studying the droplet shape in a cylindrical capillary (Section 4.5) highlights the simulation accuracy for the interaction between the droplet and the rigid channel walls.

Even though the effect of gravity can be neglected in most of the applications we consider, we validate our buoyancy model for the case of a buoyancy-driven spherical droplet (Section 4.6).

The final set of validation cases (Sections 4.7 and 4.8) covers the Laplace-solver for the electric field. We test the accuracy of the solver by considering a dielectric sphere in a uniform, exterior field (Section 4.7). In a somewhat similar setting, the deformation of a nearly-spherical dielectric droplet in an external field validates the coupling between the electric solver and the Stokes-solver (Section 4.8), which is implemented as an extension to the surface tension model on the free surface.

4.1 Flow Past a Moving Sphere

The flow field around a sphere moving with constant velocity in otherwise quiescent flow is a standard application of Stokes flow, and has a simple analytic solution against which we can compare. This test serves as a validation of the integration over curved surfaces, and the precision of integration for Dirichlet boundary conditions.

A sphere of radius a is placed at the origin, with the fluid volume Ω outside the sphere. Dirichlet boundary conditions are imposed by setting a constant velocity $\boldsymbol{u}_S$ at the sphere's surface. Implicitly, the flow goes to zero for $|\boldsymbol{x}| \to \infty$. Since the sphere is solid and not rotating, the velocity is constant on the whole surface,

$$\boldsymbol{u}_S = \boldsymbol{U} = const. \tag{4.1}$$

We use this test case to validate the boundary integration for Dirichlet boundary conditions in a simple setting, that is without high curvatures in the mesh, without thin gaps and without time dependence.

Stokes Drag

The *Stokes Law* gives a result for the hydrodynamic traction force (Stokes drag) on the sphere (Pozrikidis [2011]). On the sphere of radius a, which has a velocity $\boldsymbol{U}$ relative to the surrounding fluid (of viscosity μ), the traction force is

$$\boldsymbol{F}_{\text{Stokes}} = -6\pi\mu a\boldsymbol{U}. \tag{4.2}$$

We compare this analytic result to the surface integral

$$\boldsymbol{F}_D = \iint_S \boldsymbol{f}\,\mathrm{d}S, \tag{4.3}$$

which is the hydrodynamic drag on the sphere due to the normal stress $\boldsymbol{f}$ that the boundary integral method computes. The relative error between these two quantities is shown in Fig.

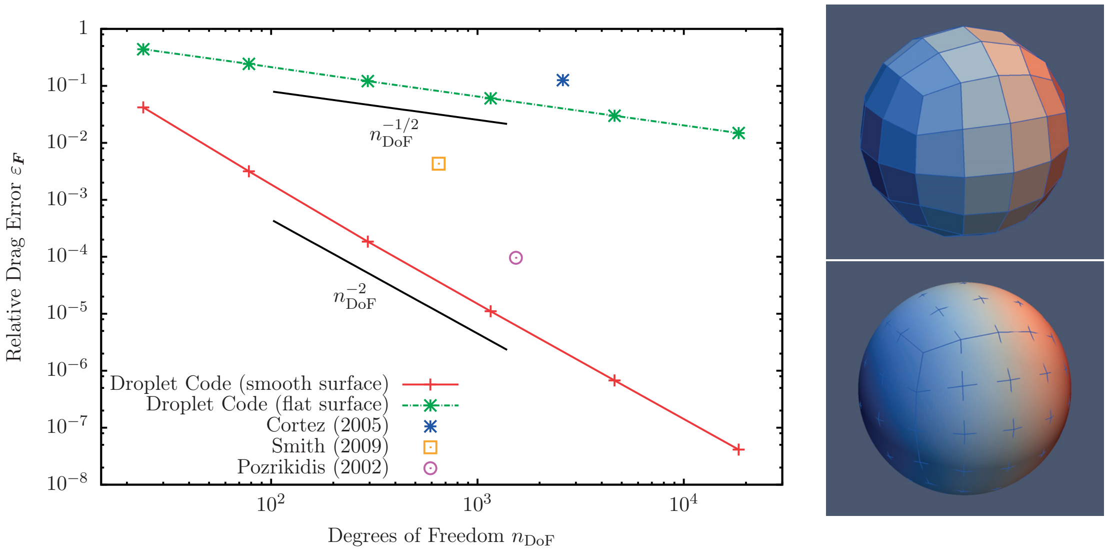

Figure 4.1: Relative error of the Stokes drag $\boldsymbol{F}_D$, $\varepsilon_F = |\boldsymbol{F}_D - \boldsymbol{F}_{\text{Stokes}}|/|\boldsymbol{F}_{\text{Stokes}}|$, for the smooth surface representation compared to the bilinear (flat) surface representation and selected other publications.

4.1. For the smooth surface representation presented in Section 3.4, the error of the drag converges with $\mathcal{O}(n_{\mathrm{DoF}}^{-2})$. Here, the accuracy benefits from the second-order surface shape representation, and the fact that the resulting surface stress is constant over the surface and can therefore be well represented by the linear finite elements and Gaussian quadrature. In the traditional surface representation with bilinear interpolation, the inaccurately represented surface location dominates the error.

The Dirichlet boundary conditions presented in this chapter are common for the side walls of the flow geometry rather than the droplet surface, at which the surface velocity is usually not known (Neumann boundary conditions).

External Flow Field

From velocity $\boldsymbol{u}_S$ and normal stress $\boldsymbol{f}$ on the sphere's surface, the velocity field for any point in the fluid volume can be constructed. We can compare this solution to the analytic result (Pozrikidis [2011]),

$$u_i(\boldsymbol{x}) = \frac{1}{4}\frac{a}{r}\left(3 + \frac{a^2}{r^2}\right)U_i + \frac{3}{4}\frac{a}{r}\left(1 - \frac{a^2}{r^2}\right)\frac{x_i x_j}{r^2}U_j, \tag{4.4}$$

to verify that the calculation of the external flow field in Ω has a desired accuracy. We evaluate the external velocity field at $\sim 10^3$ points in the vicinity of the sphere, and find that the mean deviation from the analytic solution converges like the relative error in the Stokes drag, namely with $\mathcal{O}(n_{\mathrm{DoF}}^{-2})$ (Figure 4.2).

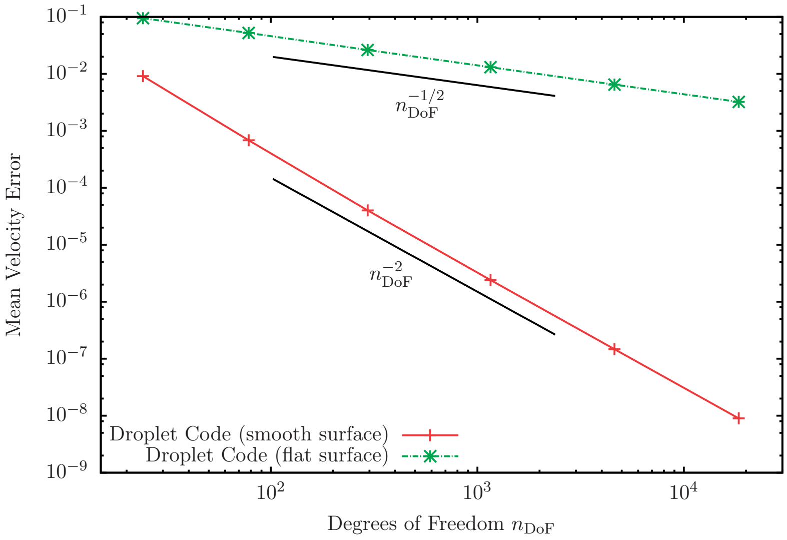

Figure 4.2: Mean error of the exterior velocity field, against the number of degrees of freedom n_{DoF}, for the smooth surface representation compared to the bilinear (flat) surface representation.

4.2 Flow in a Cuboid Duct

To simulate droplets in a microchannel, the solver combines Dirichlet boundary conditions on the microchannel inlet and side walls with mixed outlet boundary conditions, where the downstream stress (outlet pressure) and the cross-stream velocity are set to zero (Section 2.1.3). To determine the accuracy of these mixed boundary conditions, we investigate the flow solution in a cuboid fluid volume of downstream length $L_x = 2$ and cross-stream lengths $L_y = L_z = 1$ (Figure 4.3).

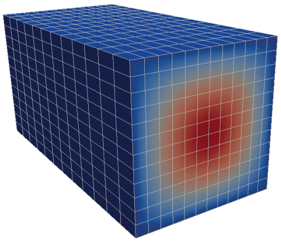

Figure 4.3: Downstream velocity for flow in a square duct, at $n_{DoF} \approx 3000$.

As a measure for the accuracy of the solution, we take the integral of the wall-normal velocity,

$$I_V = \iint_S (\boldsymbol{u} \cdot \boldsymbol{n}) \,\mathrm{d}S, \tag{4.5}$$

and of the stress over the surface,

$$I_S = \iint_S \boldsymbol{f} \,\mathrm{d}S. \tag{4.6}$$

Since the flow is incompressible and no external forces are present, both should be zero. These non-local conservation laws follow from the Stokes description, but are not used in the numerical scheme. The deviations of these two measures from zero comprises the error of the initial boundary integration, the solution of the linear system, and the surface integration (4.5) resp. (4.6).

Two flow conditions are studied: A plane Couette flow with downstream velocities ranging between $1.5U$ at the bottom surface and $2.5U$ at the top surface, and the flow in a square duct, with a biparabolic inlet boundary condition (defined in Section 2.5.2).

The velocity and stress solution of the simple shear flow can be precisely represented by the bilinear finite elements, and the fifth-order Gaussian integration scheme accurately performs the final surface integral. Consequently, the resulting relative error lies below 10^{-5} for the stress, and well below 10^{-6} for the velocity, even with few degrees of freedom (Figure 4.4a). The tolerance of the GMRES solver was set to 10^{-8}.

Next, we consider flow through a square duct, which is the prototype for any microfluidic application. The velocity profile on the inlet and outlet, and the stress on the side walls, can be approximated by parabolas or higher order polynomials. Linear elements are unable to represent the full analytic solution. For this reason, the relative velocity and stress error is orders of magnitude larger than in a shear flow (Figure 4.4b), surpassing 1% for less than $\sim 10^3$ degrees of freedom. We estimate the error of the bilinear discretization by evaluating the biparaboloid inflow profile (Eq. 2.69) on the discrete mesh vertices and integrating over the bilinear interpolation of these values. The error of this interpolation converges with $\mathcal{O}(n_{DoF}^{-1})$. In the simulation, this error appears to be superimposed with another error of order $\mathcal{O}(n_{DoF}^{-3/2})$, which happens to cancel the discretization error at $n_{DoF} \approx 10^4$, but this cancellation is coincidental and cannot be exploited to increase the simulation accuracy in the general case.

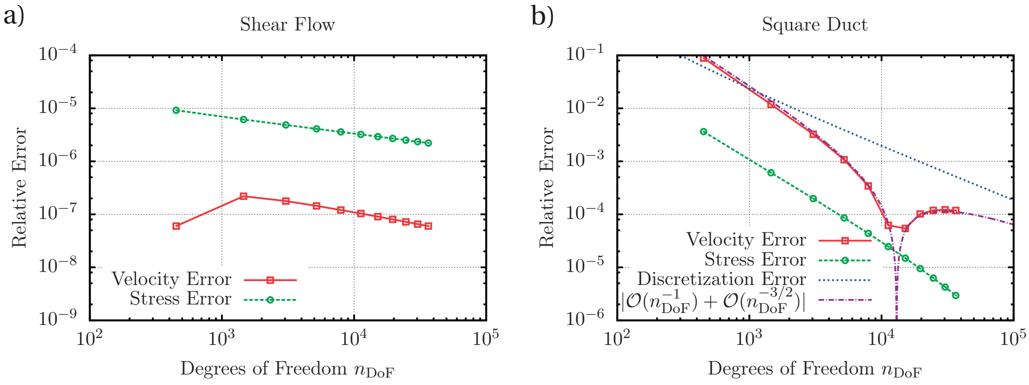

Figure 4.4: Relative error of the integrated wall-normal velocity I_V, and integrated stress I_S, for *a)* a Couette flow, and *b)* the flow through a short, square duct. We compare the velocity error in the square duct to the error of the bilinear discretization, which matches quantitatively.

4.3 Sphere Moving Past a Plane Wall

Particular challenges to the numerical scheme arise when two surfaces come very close to each other: Flow and stress vary on very small length scales, and the associated Green's functions diverge (see also Section 3.5.2). O'Neill [1967] reports an analytic solution to the drag force and torque on a sphere that moves parallel and close to a plane wall. Numeric values of that solution have been calculated by Goldman et al. [1967]. When the distance δ between the sphere and the wall becomes small, the stress on sphere and wall diverges in the gap.

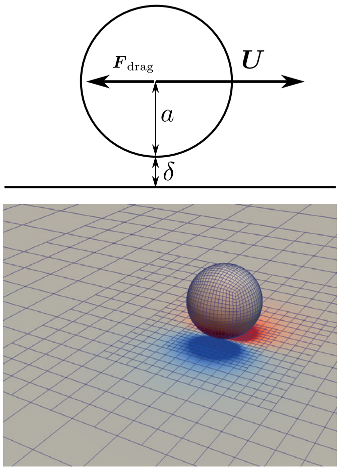

Figure 4.5: Geometry of a sphere that moves parallel to a plane no-slip wall, with the refined mesh color-coded with the wall-normal stress (*bottom*).

We approximate the infinite plane wall by a plane of edge length $10^4 a$ (where a is the radius of the sphere) and no-slip boundaries. We refine the mesh in the gap down to a resolution of $0.07a$, creating a mesh of 5000 cells. For distances $\delta > 10^{-1}a$, the simulation matches the analytic solution closely, with a drag error on the order of 10^{-3} (Figure 4.6). For large δ, the torque approaches zero, so that the relative error in the torque stays large. For smaller distances, the numerical results start to diverge from the expectations, with the relative error of the torque reaching 45% at $\delta = 0.003202a$. Here, the gap width is much smaller than the mesh spacing, so that the linear elements cannot represent the solution well.

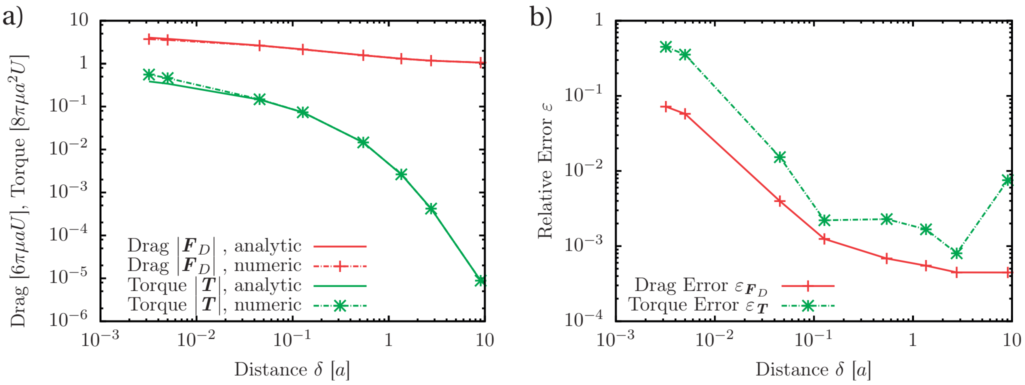

Figure 4.6: Drag $\boldsymbol{F}_D$ and torque $\boldsymbol{T}$ acting on a sphere of radius a, moving at speed U in distance δ of a fixed plate. *a)* Absolute values of drag and torque, from the analytic expression in O'Neill [1967] and the simulation results. Following Goldman et al. [1967], we give drag in units of the Stokes drag $6\pi\mu a U$ (Eq. 4.2) and torque in units $8\pi\mu a^2 U$. *b)* Relative error of the numerical result. We find a strong dependence of the error on the mesh resolution at the narrow gap.

4.4 Droplet in Extension Flow

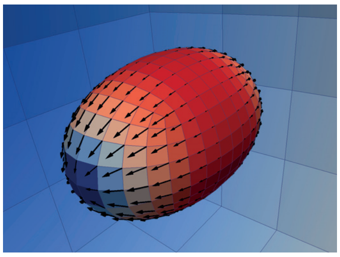

Figure 4.7: Steady-state shape of a droplet in an extensional flow at $\lambda = 1$, $Ca = 0.1$. Droplet surface colored by the divergence of the in-plane velocity.

When a free droplet interface is present, our Stokes solver couples the flow solutions on both sides of the interface. We test this coupling by comparing the equilibrium shape of a droplet in an extensional flow to known analytical and numerical results. Stone and Leal [1989b] present numerical results for the deformation of a spherical droplet of radius R in an extensional flow field of the form

$$\boldsymbol{u}(\boldsymbol{x}) = \frac{U}{2R}\begin{pmatrix} 2 & 0 & 0 \\ 0 & -1 & 0 \\ 0 & 0 & -1 \end{pmatrix}\boldsymbol{x}, \tag{4.7}$$

with U a characteristic velocity scale that defines the capillary number $Ca := \frac{\mu U}{\gamma}$. Assuming radial symmetry around the $\boldsymbol{e}_x$-axis, Stone and Leal use a 2D boundary element method to

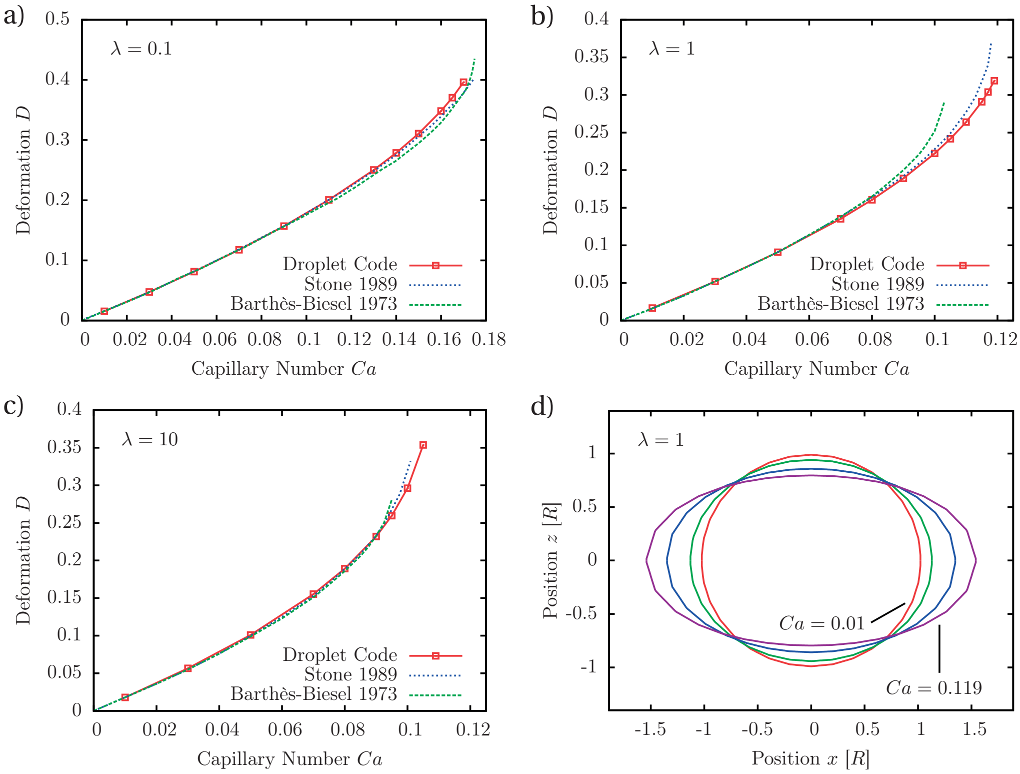

Figure 4.8: Deformation of a droplet in an extensional flow, compared to the second-order analytic approximation by Barthès-Biesel and Acrivos [1973] and the 2D-BEM-solution by Stone and Leal [1989b], at a viscosity ratio of *a)* $\lambda = 0.1$, *b)* $\lambda = 1$ and *b)* $\lambda = 10$. *d)*: Droplet cross-section at $\lambda = 1$ and $Ca = 0.01, 0.05, 0.1, 0.119$.

retrieve the equilibrium droplet shape, and describe this shape by the deformation

$$D := \frac{l_x - l_z}{l_x + l_z}, \tag{4.8}$$

where l_x and l_z are the maximum lengths in the axial x- and radial z-direction, respectively. Analytic results on the droplet shape have been derived by Barthès-Biesel and Acrivos [1973] in an approximation that is second-order in the capillary number Ca.

Unlike Stone and Leal, who prescribed the unperturbed background flow field (4.7) directly on the droplet interface, we test the coupling of exterior and interior flow solver by prescribing the flow as Dirichlet boundary conditions on a sphere of radius $10R$ around the radius-R-droplet. The resulting mesh (Figure 4.7) has ~ 2300 degrees of freedom, evenly distributed between droplet and outer boundary, and is integrated forward in time until a steady droplet shape has been reached.

The resulting droplet deformation (Figure 4.8) is in good agreement with the results by Stone and Leal, for viscosity ratios between droplet and exterior viscosity of $\lambda = 0.1, 1, 10$. For large capillary numbers ($Ca \geq 0.1$) and correspondingly high deformations ($D \geq 0.25$), we see a deviation from the expected result.

4.5 Droplet in a Cylindrical Capillary

A droplet moving in a cylindrical capillary generally takes on a rotationally symmetric shape. When rotational symmetry is assumed, the free-surface Stokes problem is reduced to a 2D problem in the axial and radial plane. This reduces the complexity of the problem to an extent that both analytical solutions (for example the asymptotic shape of an inviscid bubble by Bretherton [1961]) and reliable numerical results can be found.

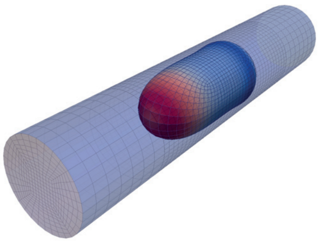

Figure 4.9: Refined mesh for the steady-state droplet in a cylindrical capillary, at $Ca = 0.05$, $a = 1.2R$. Droplet surface colored by the downstream velocity.

Lac and Sherwood [2009] present numerical results for the equilibrium shape of viscous droplets in a rotationally symmetric capillary, which they achieved with a highly resolved 2D boundary element solver. We compare the results of our 3D simulation to these results. The 3D solver faces two particular challenges in representing the mesh of the capillary: First, since we represent the outer surface of the capillary with bilinear elements, the normal vector on the cell differs from the interpolated normal at a vertex, where the degrees of freedom are defined. Thus, the wall-normal component of the stress tensor, which enters the boundary integral equation, is inaccurately represented by the interpolation between its values at the vertices. Second, since we dynamically adjust the refinement of the channel boundary and move hanging nodes to the cylindrical surface, small gaps exist between the inlet and outlet plane and the cylindrical outer surface. We find that, even in an empty capillary,

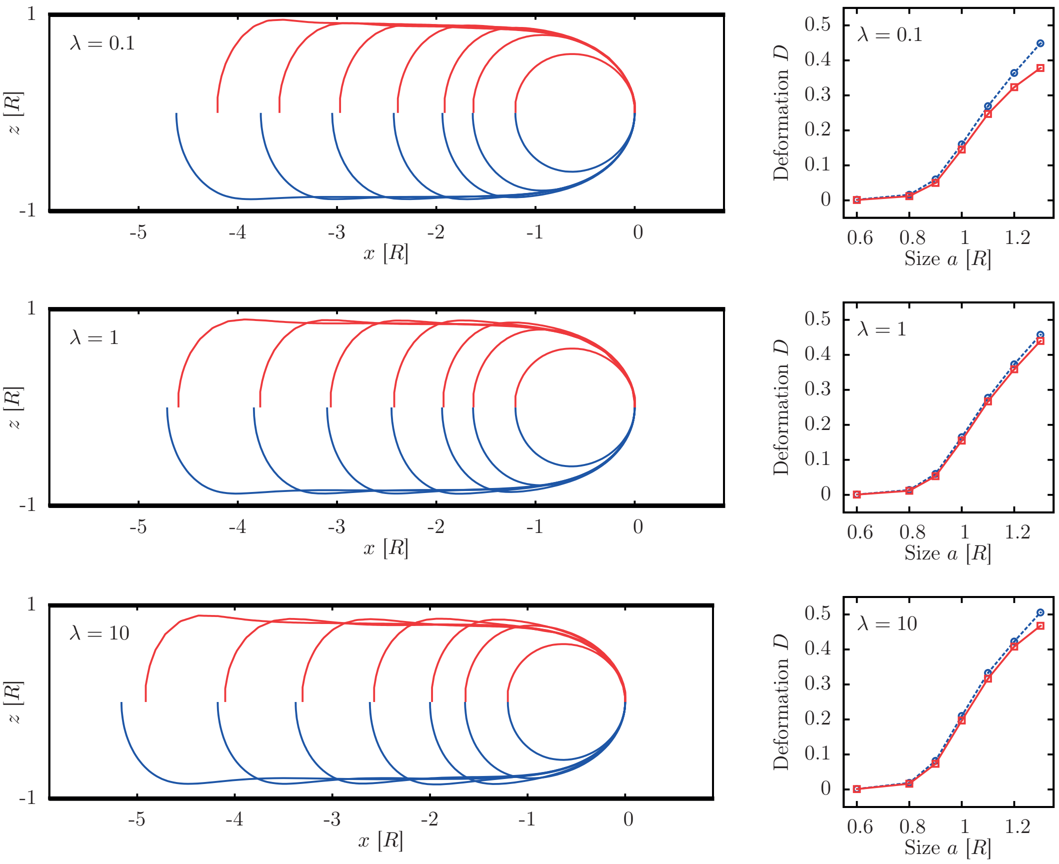

Figure 4.10: Equilibrium shape of droplets in a round capillary, compared to the results of Lac and Sherwood [2009]. *Left:* Shape of droplets in a capillary, at $Ca = 0.05$, varying viscosity ratio λ, and size $a/R = 0.6, 0.8, [0.1], 1.3$. The contours in red (top half) are from our simulation, in blue (bottom half) from Lac and Sherwood. Droplets are aligned at $x = 0$ for better readability. Differences in the total droplet length are due to deviations in the numerical flow rates, as discussed in the text. *Right:* Droplet deformation D at the respective viscosity ratios λ, dashed from Lac and Sherwood.

the center-line velocity does not maintain the expected value of $u_c = 2U$. A typical mesh with $\sim 10^5$ degrees of freedom has a center-line velocity of $u_c = 1.88U$ at the midpoint between inlet and outlet, and velocity and stress errors (see Section 4.2) of 7% and 10%, respectively. In all other simulations that we perform, microchannels have rectangular cross-sections, and do not suffer from the aforementioned error. However, to validate our simulation against known reliable results from 2D calculations, we accept this error in the flow rates, and compensate for it in the data analysis.

In a capillary of radius R and length $10R$, we create a droplet of volume $\frac{4\pi}{3}a^3$, with a the *droplet size*. For $a < 0.45R$, the initial droplet shape is spherical, whereas for larger a, the droplet is created as a prolate spheroid, such as to maintain a spacing of $0.05R$ between droplet and

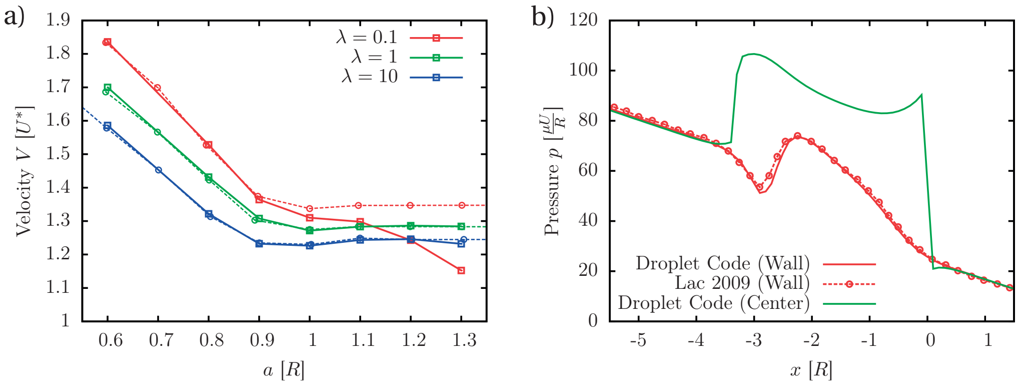

Figure 4.11: *a)* Downstream advection velocity at $Ca = 0.05$, for different droplet sizes a and viscosity ratios λ. For better readability, the advection velocity V for our results is scaled by $U^* := u_c/2$, using the center-line velocity $u_c = 1.88U$ we found in an empty channel. Dashed lines show the results by Lac and Sherwood [2009], with $u_c = 2U$. *b)* Fluid pressure in the channel, at the wall and in the channel center, for $Ca = 0.05$, $\lambda = 10$, $a = 1.1R$. The pressure in the channel center shows the Young-Laplace pressure jump at the droplet interface, which depends on the interface curvature.

side wall. From the initial droplet shape, we find the equilibrium shape by simulating forward in time, resetting the droplet center to the center of the capillary after every time step. We terminate the simulation when the droplet stops deforming. Following Lac and Sherwood, we consider a capillary number $Ca = 0.05$, viscosity ratios of $\lambda = 0.1, 1$ and 10 and droplet sizes of $0.6R \le a \le 1.3R$, and describe the droplet shape in terms of the deformation $D := \frac{l_x - l_z}{l_x + l_z}$ as defined in Section 4.4 (eq. 4.8).

For small droplets, the simulation reproduces the deformations found by Lac and Sherwood (Figure 4.10). For large droplets ($a > R$), the droplets deform less than expected. One reason is the advection velocity V of the droplets (Figure 4.11a): Due to the simulation error in total velocity, the effective capillary number is smaller, which reduces the size of the liquid layer between droplet and side wall. The advection velocity u_c in the channel center is 6% too small in an empty channel, and for small droplets, we find the same 6% decrease in advection velocity. The velocity error in the cylindrical capillary is larger than in the square duct (Section 4.2), because we represent the curved outer surface with flat, bilinear elements. A vastly improved accuracy can be achieved by using the smooth surface description (Section 3.4) both on the deforming droplet and on the curved capillary wall. With some changes in the implementation, the sharp edges for the inlet and outlet plane of the channel can be accommodated.

Despite the errors in advection velocity, the code correctly reproduces the pressure in the system, which is the dominant component of the wall-normal stress. Between the wall-normal stress reported by Lac and Sherwood and our simulation (Figure 4.11b), we find only small deviations, notably in the region of fast variation towards the rear of the droplet, where also the droplet shapes deviate from each other. Besides the wall-normal stress, which is a direct part of the solution of the boundary element method, we can also calculate the pressure at any point inside the domain (Section 2.1.4). As expected, the center line pressure equals the wall pressure away from the droplet, and jumps at the droplet interface to a higher value inside the droplet. The height of the pressure jump scales with the local curvature and surface tension (Section 2.3.1).

4.6 Rising Droplet under Gravity

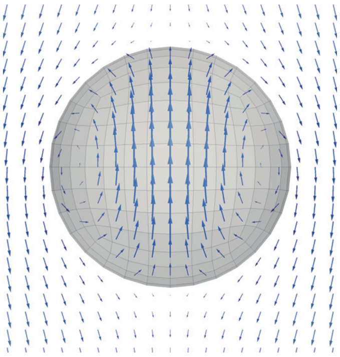

Figure 4.12: Flow in a droplet rising under gravity, at $\lambda = 10^{-2}$, in a comoving frame of reference.

When the fluid density inside a droplet is smaller than the density of the surrounding medium, a droplet rises up in a gravitational field. For spherical droplets in an infinite medium, the relation between upward velocity U_d and buoyancy force is described by the Hadamard-Rybczynski equation (Clift et al. [1978])

$$U_d = \frac{2}{9}\frac{\Delta\rho g R^2}{\mu}\frac{\lambda+1}{\lambda+2/3}, \tag{4.9}$$

with $\lambda := \mu_d/\mu$ the viscosity ratio, R the droplet radius, $\Delta\rho := \rho_d - \rho$ the density mismatch and g the gravitational acceleration. Since there is no intrinsic velocity scale, we measure velocities in terms of the viscous velocity scale $U := \frac{\mu}{\rho R}$. In the limits of very large ($\lambda \to \infty$) and very small ($\lambda \to 0$) inner viscosity, this relation represents the advection speed of a rigid sphere with no-slip and free-slip boundary conditions, respectively.[1]

For a rising deformable droplet to be spherical, the surface tension must be large against the buoyancy forces that deform the droplet, which holds if the Eötvös number

$$Eo := \frac{\Delta\rho g L^2}{\gamma}. \tag{4.10}$$

is small. We find that at $Eo = 1$, droplet deformation is negligible ($D < 10^{-4}$). For a spherical mesh of $\sim 10^3$ degrees of freedom at $Ca = 1$, $Eo = 1$, the advection velocity (Figure 4.13) closely matches the expected analytical values over the relevant range of viscosity ratios λ, with a small deviation at a small viscosity ratio.

---

[1] With the drag force given by buoyancy, $F_d = \frac{4\pi}{3}R^3\Delta\rho g$, Stokes' law yields a velocity of $U_d = \frac{2}{9}\frac{\Delta\rho g R^2}{\mu}$ for a no-slip sphere, whereas the velocity for a free-slip sphere is $U_d = \frac{1}{3}\frac{\Delta\rho g R^2}{\mu}$.

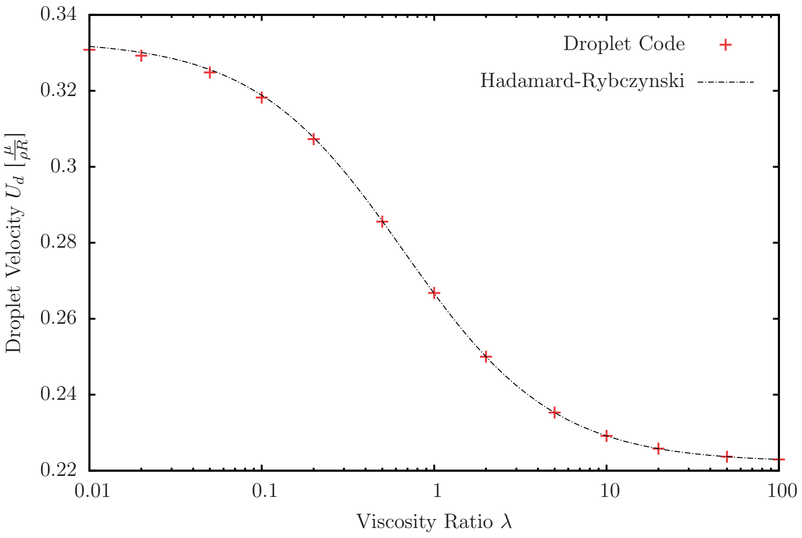

Figure 4.13: Velocity U_d of a nearly-spherical droplet rising in a gravitational field, compared to the analytical Hadamard-Rybczynski result (Clift et al. [1978]) for spherical droplets.

4.7 Dielectric Sphere in a Uniform Electric Field

To test the accuracy of the BEM-solver for dielectrics, we consider the case of a dielectric sphere placed at the origin in an infinitely extended medium with a uniform field $\boldsymbol{E}_0 = E_0\boldsymbol{e}_x$. The electric potential φ has the form (Landau et al. [1984])

$$\varphi(\boldsymbol{x}) = \begin{cases} -\frac{3}{2+\varepsilon}\,\boldsymbol{E}_0\cdot\boldsymbol{x} & |\boldsymbol{x}|\le R \\ -\left[1+\frac{1-\varepsilon}{2+\varepsilon}\left(\frac{R}{|\boldsymbol{x}|}\right)^3\right]\boldsymbol{E}_0\cdot\boldsymbol{x} & |\boldsymbol{x}|>R, \end{cases} \tag{4.11}$$

with $\varepsilon := \varepsilon_i/\varepsilon_o$ the permittivity ratio between the material inside and outside the sphere, and R the sphere radius. This electric potential creates an electric field $\boldsymbol{E}(\boldsymbol{x})$ with

$$\boldsymbol{E}(\boldsymbol{x}) = \begin{cases} \frac{3}{2+\varepsilon}\,\boldsymbol{E}_0 & |\boldsymbol{x}|\le R \\ \left[1+\frac{1-\varepsilon}{2+\varepsilon}\left(\frac{R}{|\boldsymbol{x}|}\right)^3\right]\boldsymbol{E}_0 - 3\frac{1-\varepsilon}{2+\varepsilon}\frac{R^3(\boldsymbol{E}_0\cdot\boldsymbol{x})}{|\boldsymbol{x}|^5}\,\boldsymbol{x} & |\boldsymbol{x}|>R. \end{cases} \tag{4.12}$$

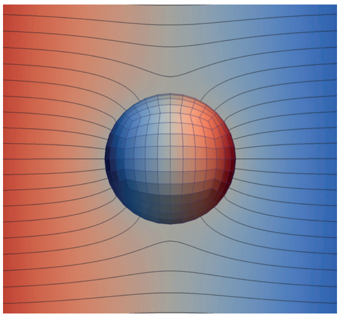

Figure 4.14: Electric field lines around a sphere in a uniform field, at $\varepsilon = 80$. The droplet is colored by the radial field component, the background by the electric potential φ.

We create the external field by prescribing the potential $\varphi_0(\boldsymbol{x}) = -E_0\boldsymbol{x}$ on the surfaces of a cube of edge length $200R$, and place the dielectric sphere of radius R with a permittivity ratio of $\varepsilon = 80$ (which is typical in experiments) near the center of the cube. Even at a relatively low mesh resolution of ~ 870 degrees of freedom, the numerical solution for the exterior electric field is accurate (Figure 4.15a). In particular, the jump in the electric field at the surface of the sphere is reproduced well.

One quantity of particular interest is the electric field on the surface, which determines the Maxwell surface stress. Since the tangential field components are determined by a surface integral (see Section 2.3.2), we can expect a significant error in these components. We quantify the error of the surface field as

$$\varepsilon_E := \sqrt{\frac{1}{N_v}\sum_i \frac{||\boldsymbol{E}_i - \boldsymbol{E}(\boldsymbol{x}_i)||^2}{||\boldsymbol{E}(\boldsymbol{x}_i)||^2}}, \tag{4.13}$$

with N_v the vertex count, $\boldsymbol{x}_i$ the vertex positions, $\boldsymbol{E}_i$ the calculated field at vertex i, and the analytic solution $\boldsymbol{E}(\boldsymbol{x})$ as in eq. (4.12). Due to the error in the tangential components, the total error in the surface field (Figure 4.15b) stays in the percent regime even at high resolutions. The error in the normal component of the field, which dominates the surface stress at high permittivity ratios (Section 2.3.2), is several orders of magnitude smaller.

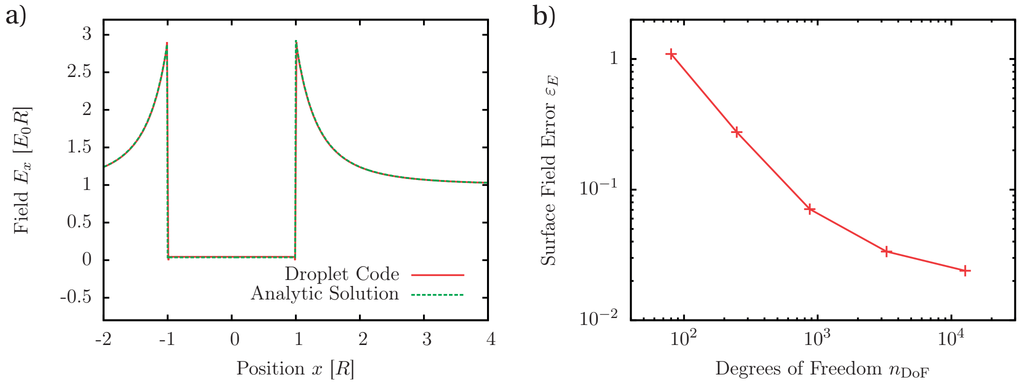

Figure 4.15: Field around a dielectric sphere in a uniform electric field. *a)* Field strength along the x-axis through the sphere center. *b)* Error ε_E of the electric field determined on the surface of the sphere.

4.8 Droplet in a Uniform Electric Field

Due to the Maxwell stress on the surface, dielectric droplets in a quiescent flow deform from their initial spherical shape when an electric field is present. The deformation grows with the field strength, but is countered by the surface tension. We therefore describe the field strength by the dimensionless electrical Bond number

$$Bo_E := \frac{\varepsilon_0 \varepsilon_c E^2 R}{\gamma}, \tag{4.14}$$

with ε_c the relative permittivity of the outer phase, E the electric field strength, $R = \sqrt[3]{\frac{3V}{4\pi}}$ the mean droplet radius and γ the surface tension.

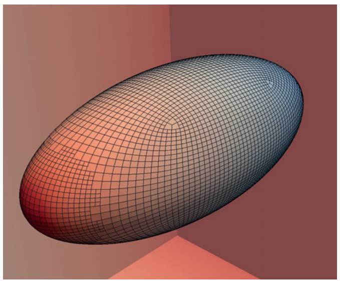

Figure 4.16: Deformed droplet in an electric field, at $\varepsilon = 10$, $Bo_E = 0.7$, colored by the normal component of the electric field.

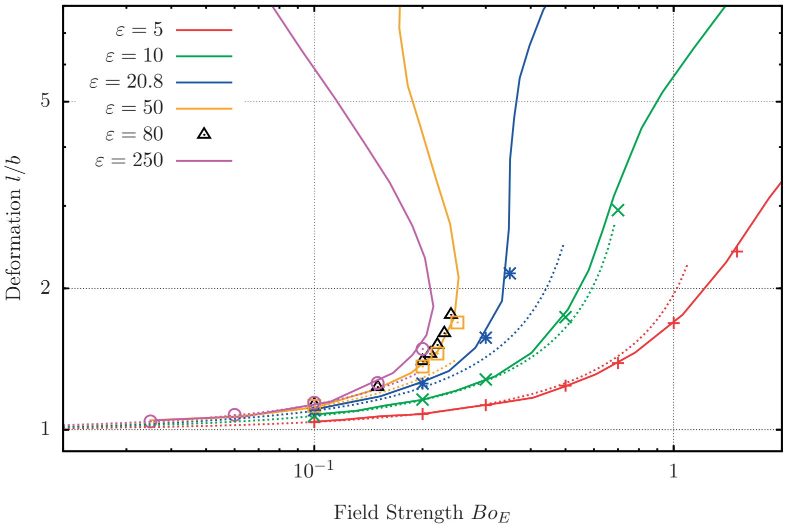

Figure 4.17: Deformation of a dielectric droplet in a uniform field, depending on the field strength E_0^2. Solid lines are analytical results for spheroidal droplets from Sherwood [1988], dotted lines the small-deformation approximation by O'Konski and Thacher Jr. [1953]. Points are fully resolved results from our code, at $\sim 10^5$ degrees of freedom.

For a uniform field $\boldsymbol{E}_0$ as in Section 4.7 and small Bo_E, the droplet assumes the shape of a prolate spheroid of length l and width b. O'Konski and Thacher Jr. [1953] describe the droplet shape by its eccentricity $e := \sqrt{1 - \frac{b^2}{l^2}}$ and use energy minimization to arrive at a relation

$$e = \frac{3}{2}\frac{\varepsilon - 1}{\varepsilon + 2}\sqrt{Bo_E} \tag{4.15}$$

between field strength and droplet shape, which is valid for small deformations ($e^2 \ll 1$). The aspect ratio $\frac{l}{b}$ of the droplet is then

$$\frac{l}{b} = \frac{1}{\sqrt{1 - \left(\frac{3}{2}\frac{\varepsilon-1}{\varepsilon+2}\right)^2 Bo_E}}. \tag{4.16}$$

With the same energy approach, Sherwood [1988] (and later Shchukin and Grigor'ev [1999]) found that ellipsoidal droplets at high permittivity ratios ($\varepsilon > 20.8$) are bistable, in other words have several energy minima for a range of field strengths E_0^2.

We create a highly resolved droplet mesh of $\sim 10^4$ degrees of freedom[2] at the center of a cube of edge length $100R$, on which we prescribe the external potential for field $\boldsymbol{E}_0$ as in Section 4.7. Starting from a sphere of radius R, we advance forward in time until a steady state solution has been found. The deformation matches the analytical predictions by O'Konski and Sherwood (Figure 4.17). The droplet shape is spheroidal for small deformations. For large deformations, the droplets deviate from a purely spheroidal shape in that they develop more pointed tips at both ends. This observation goes beyond the assumption of a spheroidal shape that the analytic approximations are based on.

---

[2] $n_{DoF} \approx 8000$ for the electrostatic solver, $n_{DoF} \approx 24000$ for the Stokes solver.

Stability of a Water Droplet

One permittivity ratio that we are particularly interested in is the value $\varepsilon = 80$, which is the contrast in electric permittivity between a water droplet and a non-polar outer phase (Lide [2004]). Using the approach of Sherwood [1988], we add up the surface energy

$$U_S = 2\pi\gamma R^2 \left[\alpha^{-2/3} + \alpha^{1/3}\frac{\arcsin(e)}{e}\right], \tag{4.17}$$

where $\alpha := \frac{l}{b} = \frac{1}{\sqrt{1-e^2}}$ describes the droplet deformation, and the electrostatic energy (Landau et al. [1984]; Sherwood [1988])

$$U_E = -\frac{1}{3}\frac{2\pi\varepsilon_0\varepsilon_c E_0^2 R^3(\varepsilon-1)}{1+\frac{1}{2}(\varepsilon-1)\cdot A_1(e)} \tag{4.18}$$

with $A_1(e) = -\frac{1}{\alpha^2 e^3}\left[2e - \ln\left(\frac{1+e}{1-e}\right)\right]$. Normalizing the total energy by the factor $2\pi\gamma R^2$ gives

$$U_\Sigma^* := \frac{U_S + U_E}{2\pi\gamma R^2} = \alpha^{-2/3} + \alpha^{1/3}\frac{\arcsin(e)}{e} - \frac{1}{3}\frac{Bo_E(\varepsilon-1)}{1+\frac{1}{2}(\varepsilon-1)\cdot A_1(e)}. \tag{4.19}$$

We then numerically find the energy saddle points

$$\frac{\partial U_\Sigma^*}{\partial e} = \frac{\partial^2 U_\Sigma^*}{\partial e^2} = 0, \tag{4.20}$$

i.e. the values of Bo_E where a stable droplet shape becomes unstable. At $\varepsilon = 80$, we find the lower equilibrium shape of the droplet to become unstable at a Bond number of $Bo_E = 0.23342$ and a deformation of $\frac{l}{b} = 1.94$. In the simulation, which does not assume a spheroidal droplet, the droplet with small deformation is stable at $Bo_E = 0.23$, whereas at $Bo_E = 0.24$ we don't find an equilibrium shape (Figure 4.17).

When the outer phase is slightly polarizable (for polydimethylsiloxanes, the relative permittivity is 2.5 to 2.8 depending on the molecular length [Moretto et al., 2000, p. 684]), the permittivity ratio is on the order of $\varepsilon \approx 30$. In this case, Sherwood's calculations suggest the critical Bond number where the droplet shape becomes unstable to be in the range $0.25 \leq Bo_E \leq 0.3$.

4.9 Summary

We validated our numerical code, and quantified the errors of the numerical discretization. Due to the smooth interpolation of the surface, the flow around a solid sphere (Section 4.1) can be calculated at high precision, with a relative error of 10^{-6} at a moderate 10^3 degrees of freedom. The stress on a solid sphere moving in quiescent flow is constant on the surface, and can therefore be represented with linear basis functions. The surface interpolation, numerical quadrature and the solver for the linear system, which we converge to an accuracy of 10^{-8}, have a combined error below 10^{-6} in this situation.

Couette flow in a cuboid fluid volume (Section 4.2) can be represented with bilinear elements, and errors are on the order of 10^{-6}. However, when flow and stress on the boundary do not change linearly, as in the case of flow through a rectangular duct, errors are three orders of magnitude higher: The order of the finite-support basis functions is too low to represent Stokes solutions accurately, and high mesh resolution is needed to compensate this error. High mesh resolution is particularly important in narrow gaps, where the mesh spacing should be at least on the order of the gap width (Section 4.3).

The validation of the droplet shape in different flow situations (Sections 4.4-4.6) confirm the correctness of the implementation. In a cylindrical capillary (Section 4.5), we observe an error in the mean flow on the order of 6%, which is due to the bilinear representation of the parabolic flow profile in the inlet and outlet, but also the curvature in the walls of the channel geometry, which we represented with a flat interpolation between mesh vertices. In the simulations we will show later, microchannels have rectangular cross-section, so that a flat surface representation is adequate for the channel surface.

The electric field on a droplet surface is calculated with two steps of boundary integration (see Section 2.2.2): In a first step, the flux through the surface is determined, from which the field is calculated via a nearly singular boundary integral in the second step. The total error of this procedure lies at 10^{-2} to 10^{-1}, depending on the mesh resolution (Section 4.7). The coupling to the Stokes solver produces results with similar accuracy (Section 4.8).

From our validation, we find that the linear order of shape functions dominates the error in our simulations. To increase the accuracy, quadratic elements can be used. Implementing them in the numerical code is tedious, but well supported by the numerical framework, and will improve the accuracy of the scheme.

Droplet Dynamics in Microchannels Part II

Droplets in microfluidic applications display complex interactions with each other and the surrounding microchannels. We combine numerical simulations with experimental results to understand the droplet behavior in two specific environments.

Microfluidic experiments are typically observed under a microscope, showing a 2D image of the droplet motion. System properties like the fluid viscosities or surface tensions are determined outside the device, before the experiment, and flow fields in the device can be measured by adding tracer particles to the flow. However, the resolution of experimental measurement techniques in the microfluidic system is limited, and quantities such as the pressure distribution or local interfacial stresses cannot be measured at all. Numerical simulations give us access to these important quantities. By comparing experimental observations to numerical simulations of the same system, we unveil the local physical effects that drive the behavior.

In this part of the thesis, we use the numerical boundary-element method to understand droplet dynamics. In Chapter 5, we investigate the interaction of two droplets as they meet in a Y-junction. We explore the process of droplet breakup, which is the limiting factor when reinjecting a dense emulsion into a microfluidic device. In Chapter 6, we analyze the efficiency of dielectrophoretic droplet sorters, which are an important component in many microchannel designs. Based on insights gained from numerical simulations, we design new electrode geometries for sorters, and show their superior performance in experiments.

The work leading to the results in this part of the thesis has been carried out in collaboration with other researchers, and is being prepared for publication in scientific journals. A preamble in each chapter explains the contributions of the respective collaborators, and the status of submission.

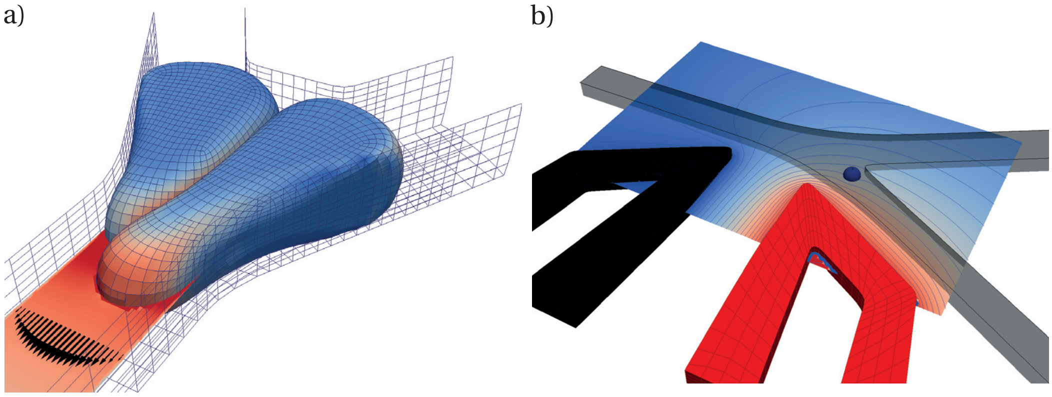

Droplet dynamics in microfluidic applications. *a)* Interaction of two droplets in a Y-junction (Chapter 5). *b)* Droplet sorting with dielectrophoresis (Chapter 6).

5 Droplet Breakup in Constrictions

Contents

5.1 Time-varying Droplet Configuration Determines Break-up Probability of Drops within a Concentrated Emulsion 80
5.2 Interaction and Breakup of Droplet Pairs in a Microchannel Y-Junction . . . 81
  5.2.1 Introduction 82
  5.2.2 Problem Formulation and Methods 83
  5.2.3 Results and Discussion 86
  5.2.4 Conclusion 94
  5.2.5 Appendix 95
5.3 Summary 96

This work has been carried out in collaboration with Jian-Wei Khor (U Stanford), Minkyu Kim (U Stanford), Sindy Tang (U Stanford) and Tobias M Schneider (EPFL). All collaborators designed the research. JK and MK carried out the experiments. SS (this author) performed the numerical simulations.

The first part of this work was published in Applied Physics Letters *[Khor et al., 2017]. Since the contribution of SS to the final text was small, we summarize the results here, but refer to the article for the full text.*

The second part is currently in the manuscript stage, for submission as Schütz et al. [2018b]. TMS and SS designed the outline, SS wrote the manuscript, with editing by the coauthors. With permission from the coauthors, we report here the full text of the manuscript, in its preliminary form and with changes to match the formatting.

When droplets that form a concentrated emulsion are funneled into a constriction, droplet interaction will lead to the disintegration of droplets under flow parameters where single droplets would keep their integrity. This jamming phenomenon limits the throughput for droplet reinjection, and for on-chip applications that store droplets in a densely packed configuration before processing. Rosenfeld et al. [2014] investigated the system and reported the probability of droplet breakup in its dependence on the capillary number Ca, which scales with the flow rate for a given droplet system. Gai et al. [2016b] described the rearrangement process of droplets before entering a constriction. For the dependence on system parameters like the capillary number ($Ca := \mu U / \gamma$), geometry of the constriction (including droplet confinement $a := R/R_H$, with R the characteristic droplet radius and R_H a characteristic channel diameter) and viscosity ratio λ, Gai et al. [2016a] found a scaling of the probability of droplet breakup at the constriction with the product $Ca \cdot \lambda \cdot a$. The breakup of droplets was generally attributed to the interaction of droplet pairs at the constriction [Rosenfeld et al., 2014], but no detailed description of this interaction or the underlying physical process was available.

5.1 Time-varying Droplet Configuration Determines Break-up Probability of Drops within a Concentrated Emulsion

In Khor et al. [2017], we correlated the probability for droplet breakup in concentrated emulsion with the offset in the leading edge between two respective droplet pairs upon entering the constriction. With Δx the leading-edge offset between two droplets, and D the characteristic droplet diameter, the fate of the more advanced droplet of the pair is determined by the capillary number Ca and the relative leading-edge offset $\Delta x / D$. At large capillary numbers ($Ca \geq 10^{-2}$) and small offsets ($\Delta x / D \leq 0.2$), there is a region where droplets always break up (Figure 5.1a). Small capillary numbers and/or large offsets do not lead to breakup, as

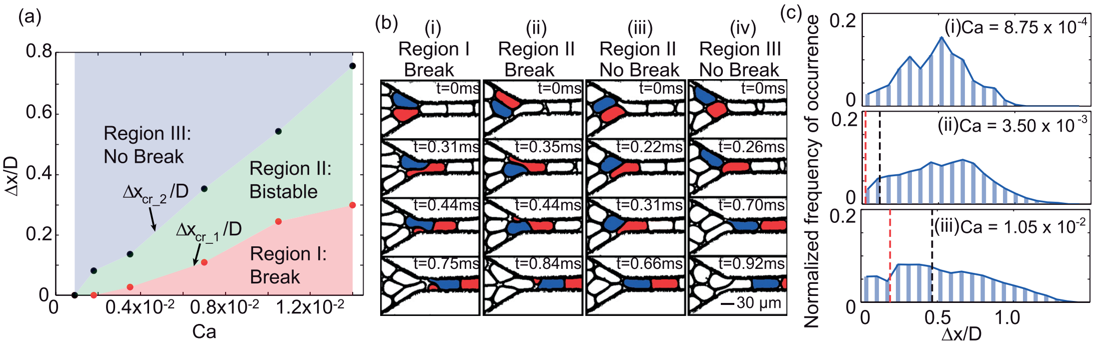

Figure 5.1: Droplet breakup in a concentrated emulsion. *a)* The occurrence of breakup depends on the leading-edge offset Δx between subsequent droplets, and the capillary number Ca. *b)* In the bistable region, the arrangement of additional droplet influences the breakup. *c)* The distribution of leading-edge offsets between droplets changes with the capillary number. – Figure reproduced from Khor et al. [2017] with permission from the other authors and the publisher.

the droplets rearrange and enter the constriction one after the other. In between these two regions, there is a bistable regime where offset and capillary number alone do not predict whether a droplet will break up: In the bistable region, the arrangement of additional droplets determines whether the leading droplet breaks (Figure 5.1b). The distribution of leading-edge offsets is a result of the droplet self-organization upstream from the constriction. At low flow rates ($Ca \sim 10^{-3}$), the distribution is peaked around $\Delta x/D \approx 0.5$, whereas higher flow rates ($Ca \sim 10^{-2}$) lead to a more homogeneous offset distribution with a higher maximum offset (Figure 5.1c). The distribution of offsets measured in the constriction and the relation between offset and breakup are sufficient to determine the fraction of droplets that break up.

Since the break-up probability of droplets is determined to a large extent by the configuration of just two droplets as they enter the constriction, we now investigate the interaction of two droplets that meet in a microchannel Y-junction.

5.2 Interaction and Breakup of Droplet Pairs in a Microchannel Y-Junction

Simon S Schütz[1], Jian-Wei Khor[2], Sindy K Y Tang[2] and Tobias M Schneider[1]

[1] Emergent Complexity in Physical Systems Laboratory (ECPS), École Polytechnique Fédérale de Lausanne (EPFL), Station 9, 1015 Lausanne, Switzerland

[2] Department of Mechanical Engineering, Stanford University, Stanford, CA 94305, USA

Abstract

We combine theory, numerics and experiments to investigate the breakup of two identical droplets entering a Y-junction with controlled spatial offset by which the second droplet trails the first. Based on fully resolved 3D simulations, we describe the flow physics leading to breakup. Scaling arguments, numerical simulation and experiments consistently show that for small initial offset breakup will occur with the fragment volume depending linearly on the offset. Above a critical offset, which increases with the capillary number, there is no breakup but both droplets subsequently enter the constriction without disintegration.

For capillary numbers up to $Ca \simeq 10^{-2}$, the two-droplet Y-junction results are consistent with breakup observations in dense emulsions flowing through a constricted microchannel, where droplet breakup limits the maximal throughput for sequential droplet processing. The deterministic relation between initial offset and resulting breakup in Y-junctions suggests that the stochasticity that is observed in emulsion breakup is caused by droplet interactions in the emulsion before the constriction, rather than in the microchannel constriction itself. The numerical value of the prefactor in the linear relation between initial offset and droplet fragment volume determined from precision experiments slightly differs from the one extracted from fully resolved numerical simulations. This discrepancy suggests that even at very high bulk surfactant concentrations, the rate-limiting surfactant adsorption kinetics allows for Marangoni stresses to develop and modify the droplet dynamics.

5.2.1 Introduction

In recent years, droplet microfluidics has become a standard tool for high-throughput biochemical assays, such as polymerase chain reaction (PCR) [Kiss et al., 2008], in vitro enzyme evolution, and drug screening [Brouzes et al., 2009; Agresti et al., 2010; Baret et al., 2009b]. One of the strengths of droplet microfluidics is the high rate at which droplets can be processed. However, this rate is limited due to the occurrence of droplet breakup at high flow velocities, in particular when droplets are stored as a concentrated or dense emulsion and then reinjected into the microfluidic system. Here, we investigate the physical mechanism driving the breakup within the emulsion that results primarily from the interaction of two droplets as they enter a narrow constriction simultaneously.

Past research on the breakup of droplets has focused on single droplets, either in the shear of an external flow [Stone and Leal, 1989b,a] or in interaction with microchannel walls in junctions [Link et al., 2004; Ménétrier-Deremble and Tabeling, 2006; Leshansky and Pismen, 2009]. Here, droplet breakup occurs when the exterior flow stretches the droplet, forming a neck that undergoes an autonomous pinch-off process [Hoang et al., 2013]. A similar process of induced neck formation and pinch-off has been observed experimentally for the interaction of two droplets in a T-junction [Christopher et al., 2009].

In emulsions that enter a constricted microchannel, the situation is more complicated. There, the occurrence of breakup appears to be stochastic, and the occurrence of breakup and size distribution of breakup fragments follows a probabilistic description. First results on the statistics of droplet breakup in dense emulsions were reported by Rosenfeld et al. [2014], who gave the probability of droplet breakup in terms of the capillary number Ca, which is the ratio of viscous and surface tension forces. Gai et al. [2016a] reported on the change of breakup probability when varying the droplet size and the viscosity ratio between droplet and continuous phase. Recently, we observed that for capillary numbers in an intermediate range ($Ca \sim 10^{-3}$), droplet breakup depends on the initial offset between the leading edges or the fronts of two droplets entering the constriction [Khor et al., 2017]. This observation suggests that droplet breakup in dense emulsions is controlled by the deterministic interaction of two droplets in the constriction, with stochasticity resulting from the irregular arrangement of droplet pairs in the dense emulsion.

Droplet breakup is controlled by a competition between viscous stresses that scale with $f_{\text{visc}} = \frac{\mu_d U}{H}$ and promote elongation and breakup of the droplet, and the surface tension stress that scales with $f_{\text{surf}} = \frac{\gamma}{R}$ that counteracts deformation. μ_d, U, H, γ, and R are the droplet viscosity, characteristic droplet speed, channel height, interfacial tension, and droplet radius, respectively. The ratio between viscous stress and surface tension,

$$\frac{f_{\text{visc}}}{f_{\text{surf}}} = \frac{\mu_d U R}{\gamma H} = Ca \cdot \lambda \cdot a \tag{5.1}$$

(with viscosity ratio $\lambda = \frac{\mu_d}{\mu}$, capillary number $Ca = \frac{\mu U}{\gamma}$, and relative droplet size $a = R/H$),

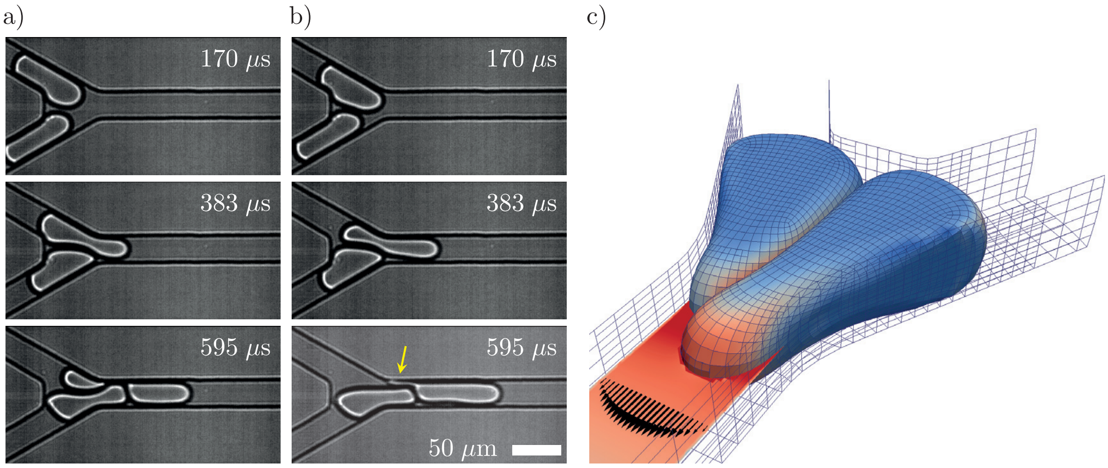

Figure 5.2: *a), b)* Interaction of droplet pairs (from the experiment at $Ca = 0.021$). Depending on their initial offset, droplet D_1 either breaks up (a), or not (b). The arrow in the last frame of (b) points out the shedding of a thin sheet of fluid from droplet D_1. *c)* Three-dimensional, fully resolved droplet shape (from the simulation at $\alpha = 30°$, $Ca = 0.06$). The surface mesh has approximately 7,000 vertices, corresponding to 21,000 degrees of freedom. Droplets are colored by the streamwise velocity. At mid-height in the channel, we determine the pressure field (colors) and velocity field (arrows).

gives an approximate scaling of the onset of droplet breakup [Gai et al., 2016a].

In this paper, we report an experimental, numerical and theoretical investigation of the two-droplet interaction that leads to droplet breakup. We study an isolated system of two identical droplets meeting in a Y-junction (Figure 5.2), where droplet breakup depends on the precisely controlled symmetry-breaking offset between the droplets. Based on fully-resolved 3D numerical simulation data, we quantitatively describe the physical processes that lead to the breakup process. A scaling analysis, fully resolved 3D simulations and precision experiments consistently show that (1) droplet breakup occurs when their fronts are below a critical offset, (2) the volume of the leading fragment depends linearly on the offset and (3) the value of the critical offset itself grows with the capillary number so that at higher Ca, a wider range of initial offsets leads to droplet breakup.

Precise quantitative comparison of prefactors between experiment and numerical simulation suggests that even at very high bulk surfactant concentrations, non-equilibrium surfactant distributions result in Marangoni stresses that modify the droplet dynamics.

5.2.2 Problem Formulation and Methods

Problem Formulation

In a continuous phase of viscosity μ, two identical droplets of volume $V = 50\,\text{pL}$ and viscosity μ_d enter a Y-junction between two symmetric inlet channels of height $H = 25\,\mu\text{m}$ and width

$W = 30\,\mu$m, and one outlet channel of the same size. The angle of the channel junction is $\alpha = 15°$ or $\alpha = 30°$. The flow rate in the two inlets is equal, and the total flow Q is varied between 0.4 mL/h and 2 mL/h. One droplet enters the constriction ahead of the other by a leading-edge offset δ_0 of up to $35\,\mu$m.

We choose the system height H as our characteristic length scale and the mean outlet velocity $U := Q/(WH)$ as characteristic velocity scale, which defines a characteristic time scale $\tau := H/U$ in a range between $30\,\mu$s and $170\,\mu$s. For a fixed channel geometry, the system is described by three dimensionless parameters, which are the droplet confinement factor $a := \sqrt[3]{\frac{3V}{4\pi}}/H$, the viscosity ratio $\lambda := \frac{\mu_d}{\mu}$, and the capillary number $Ca := \frac{\mu U}{\gamma}$, where γ is the surface tension between the droplet and continuous phase. In our system, confinement factor and viscosity ratio are fixed to $a = 0.914$ and $\lambda = 0.8$. At the considered length scales, the effect of inertia can be neglected. For fixed channel geometry, droplet size and fluids, we have one control parameter, the capillary number (controlled by the flow rate), which we vary between $Ca = 0.007$ and $Ca = 0.1$. The dynamics of droplet breakup depend on the capillary number Ca, and the initial droplet configuration, measured by the offset δ_0.

Numerical Simulation

Numerical simulations are performed with a Boundary Element Method (BEM) numerical code based on the DEAL.II numerical framework [Bangerth et al., 2007]. The MPI-parallel `C++` code solves the Stokes equations for incompressible Newtonian flow,

$$\mu\nabla^2\vec{u} - \nabla p = \vec{0}, \tag{5.2}$$

$$\nabla\cdot\vec{u} = 0, \tag{5.3}$$

both in the continuous phase and inside the droplets (with μ the dynamic viscosity inside the respective domain), under no-slip boundary conditions on the channel side walls, a prescribed velocity profile at the channel inlet, a constant reference pressure at the channel outlet, and a Young-Laplace surface stress of the form

$$\Delta\vec{f} = -2\gamma\kappa\vec{n} \tag{5.4}$$

at the droplet interfaces, where γ is the surface tension, κ the mean curvature and $\vec{n}$ the interface normal. Surfaces are represented by a dynamically refined quad mesh with a second-order (paraboloid) surface shape interpolation. Time stepping uses a first-order explicit scheme. The linear system of approximately 21,000 degrees of freedom (for velocity and stress at all interfaces) is solved with the iterative GMRES algorithm. The mesh is modified after each time step to fix the droplet volumes to the desired value, ensure a minimum gap width between all interfaces of $10^{-2}H$, and suppress distortions of the mesh cells. Simulations are performed for $0.03 \le Ca \le 0.1$ in increments of 0.01, for initial droplet offsets $0.05H \le \delta_0 \le 1.5H$. No breakup is observed for $Ca < 0.05$. The viscosity ratio is $\lambda = 0.8$ and the confinement factor is $a = 0.914$. The BEM-scheme does not capture the topological transition of droplet breakup. Instead, we detect the formation of a neck, and terminate the simulation when the neck width is below 10% of the channel width. Each simulation run requires between 600 and 2,700 CPU core-hours on a state-of-the-art x86 processor, with simulations at lower Ca demanding more computational effort. In total, we perform 122 simulations for the different values of Ca and δ_0 mentioned above.

Laboratory Experiments

Laboratory experiments use microchannels fabricated in poly(dimethylsiloxane) (PDMS) by soft lithography (Figure 5.3a). The microchannels are bonded to a glass substrate using oxygen plasma and then treated with Aquapel (Pittsburgh, PA) to make the walls of the channel hydrophobic. The height H of the channels is $25\,\mu$m and the width W of the constriction channel is $30\,\mu$m. The entrance angle α to the constriction is 15° respectively 30° (Figure 5.3b,c). The exit angle from the constriction is 5° to prevent droplet coalescence.

We use a flow-focusing nozzle to generate monodisperse droplets. The disperse phase consists of deionized water and the continuous phase consists of HFE-7500 (3M) containing an ammonium salt of Krytox (2% w/w) as a droplet stabilizer. The interfacial tension between the two liquids is measured to be 26.25 mN/m using a pendant drop goniometer. The viscosity of the continuous phase is 1.24 mPa s. The mean size of the droplets is 50 pL and the coefficient of variation of droplets is about 3% in volume. The generated droplets are collected and stored in a 3-mL syringe for 4 hours at room temperature. During this time, the drops cream to the top of the syringe to form a concentrated or dense emulsion, as the drops are less dense than the continuous phase. The volume fraction of the emulsion obtained is about 85%. The size of the droplets remains unchanged after their concentration.

For the break-up experiments, the dense emulsion is split into two syringes. The two syringes

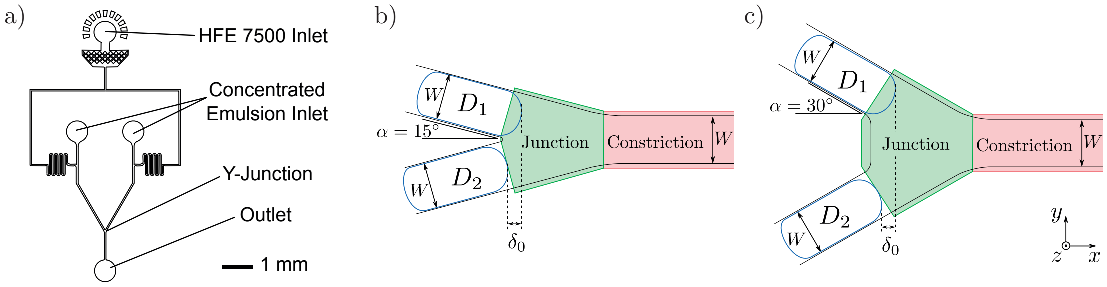

Figure 5.3: *a)* Design of the experimental microfluidic device. Microchannels have a height of $H = 25\,\mu$m and a width of $W = 30\,\mu$m, flow rates vary from 0.4 mL/h to 2.0 mL/h. *b), c)* Y-junction geometry: Two rectangular channels of height H and width W meet at different angles $\alpha = 15°$ (b), $\alpha = 30°$ (c). The junction leads into a constriction of width W. Two identical droplets D_1, D_2 arrive at the junction with an offset δ_0 in the streamwise direction.

of emulsions are injected into a new device via two separate inlets. Immediately downstream from the inlets for the emulsion, extra continuous phase is introduced at 90° to both of the branches to lower the volume fraction of the emulsion. The flow rate ratio between the dense emulsion and the continuous phase is fixed at 0.2 to obtain a final droplet volume fraction of about 14%. At this volume fraction, the drops are spaced by a sufficiently large distance from each other to avoid droplet interactions within the same branch prior to entering the constriction. The diluted drops from the two branches then travel downstream and meet at the Y-junction leading to the constriction, where break-up events are recorded. The height of the channel is smaller than the diameter of the droplets when spherical, and the drops always span the whole height of the channel. The total flow rates for our experiment varies from 0.4 mL/h to 2.0 mL/h, and are controlled by three syringe pumps (Kent Scientific), two for the dense emulsions, and one for the extra continuous phase to dilute the emulsions.

An inverted microscope mounted with a high-speed camera is used to acquire images of droplet pairs flowing through the constriction at a frame rate of 45,000 frames per second. This frame rate is sufficiently fast to resolve the leading edges or the fronts of the droplet pairs at the flow rates tested. A custom Matlab code is used to track the location, area, and shape of all droplet pairs ($n > 1,000$) as well as their broken fragments, and also to measure the offset between the droplet pairs in each frame. Details of the Matlab droplet pair detection algorithm are described by Gai et al. [2016a] and Khor et al. [2017].

5.2.3 Results and Discussion

Droplet interaction in the Y-junction proceeds as follows: As the two droplets enter the space of the junction, their interfaces form a vertical double interface. The front of the first droplet moves into the constriction more quickly, whereas the front of the second droplet slows down. When the front of the second droplet approaches the constriction, a neck forms in the first droplet. In situations where the initial leading-edge offset is small, this neck gets progressively thinner and finally pinches off – the first droplet breaks into two fragments (Figure 5.2a). Breakup is avoided when the initial offset is larger (Figure 5.2b): Like in the case of small offset, the droplets form a double interface, and the front of the first droplet moves faster while that of the second slows down. However, the rear of the first droplet clears the constriction entrance before a neck can pinch off – both droplets stay intact.

Physical Description of the Breakup Process

To gain a quantitative understanding of the breakup process, we perform a full 3D simulation of the flow and the droplet interaction in a 30°-junction at $Ca = 0.06$ and offset $\delta_0 = 0.1H$. The droplet interface shape is resolved on a sub-μm scale with a dynamic mesh of approximately 7,000 vertices (Figure 5.2c). The simulation gives access to the time-dependent full 3D geometry, velocity fields and the pressure.

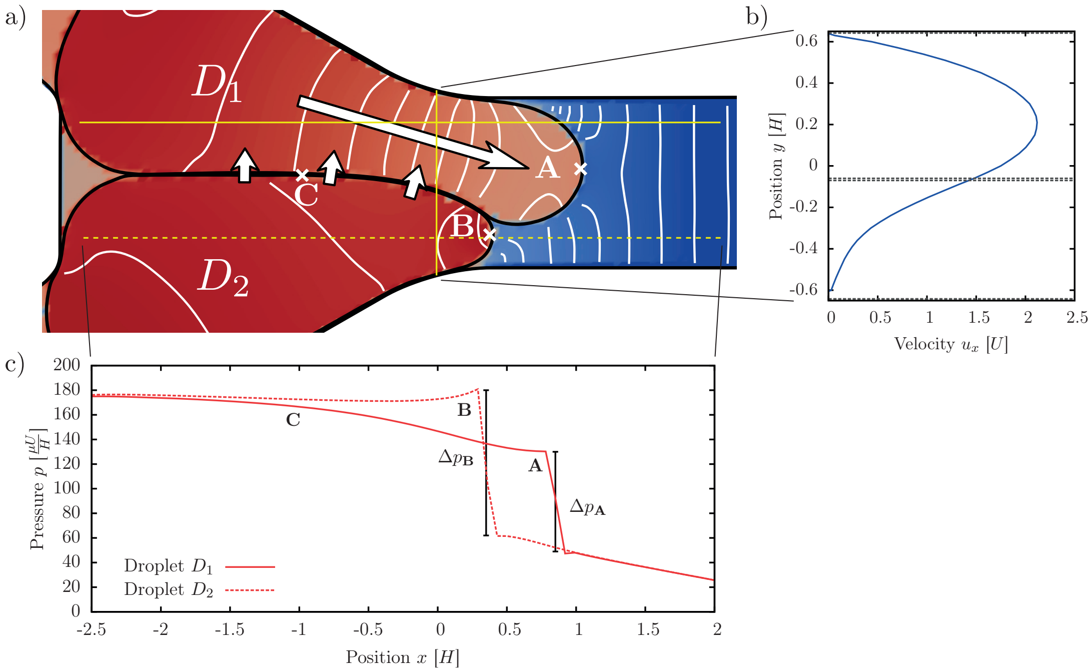

Figure 5.4: Interaction of two droplets with offset $\delta_0 = 0.1H$ at junction angle $\alpha = 30°$ and capillary number $Ca = 0.06$ (simulation). *a)* Midplane pressure field and contours. *b)* Flow velocity at the constriction (vertical solid line in a) in units of the mean flow rate U. The dotted line marks the position of the droplet double interface. *c)* Streamwise pressure profile (horizontal full and dashed lines in (a)) inside droplets D_1 and D_2. Due to the different front curvatures at points **A** and **B**, the pressure jump $\Delta p_{\mathbf{A}}$ is smaller than $\Delta p_{\mathbf{B}}$, inducing a pressure gradient that drives a relative flow.

As the droplets move into the common space of the junction and form a common interface, the front cap of the first droplet D_1 maintains a larger radius than the front of droplet D_2 due to the initial offset. Across our simulations, we find that for small but finite offsets ($\delta_0 < 0.3H$) the difference in front radius ΔR scales approximately with $\Delta R \approx 0.25\delta_0$.

The difference in front radius is the driving force behind the subsequent dynamics. For an interface under surface tension, a curvature of the interface leads to a pressure jump between the two sides, described by the Young-Laplace equation [Batchelor, 1967]

$$\Delta p = \gamma \left(\frac{1}{R_1} + \frac{1}{R_2} \right), \tag{5.5}$$

where R_1 and R_2 are the principal radii of curvature. The resulting pressure field across both droplets is shown in Figure 5.4: When the droplets reach the constriction, the horizontal front radius of D_1 (point **A**) is larger than that of D_2 (point **B**), so that the pressure jump $\Delta p_{\mathbf{A}}$ is smaller than the pressure jump $\Delta p_{\mathbf{B}}$. As the pressures are similar towards the back of the droplets, the pressure gradient within the bulk of D_1 (**C** → **A**) is larger than inside D_2 (**C** → **B**). The difference in pressure gradient drives a relative flow between the droplets (Figure

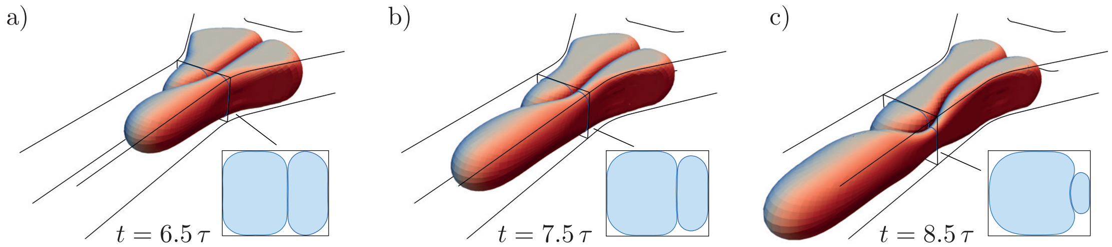

Figure 5.5: Interaction of two droplets with offset $\delta_0 = 0.1H$ at junction angle $\alpha = 30°$ and capillary number $Ca = 0.06$, at different times t after droplets enter the junction. Images from the simulation. A neck forms in the leading droplet, first only in the horizontal direction (a), then also vertically (b). After the neck starts forming in the vertical direction, pinch-off happens quickly (c).

5.4c). The relative flow increases the offset δ and thus the front radius of D_1, the process is self-reinforcing and leads to drainage of D_1 ahead of D_2. The drainage rate is proportional to the surface tension γ and inversely proportional to the shear stress $\mu_d U$ that counteracts the flow. A quantitative estimate of the drainage rate is given in Appendix 5.2.5.

The formation of a neck and subsequent pinch-off interrupt the drainage process: Along the double interface behind the front caps, the pressure in droplet D_2 is higher than in droplet D_1. This pressure difference is not fully compensated by the curvature of the double interface between the droplets, and leads to a cross-stream motion of the double interface towards droplet D_1, so that droplet D_1 elongates and a neck forms. As the neck enters the constriction, it gets so narrow that curvature in the vertical z-direction becomes larger (Figure 5.5). Driven by the large curvature in the vertical direction, the interface of D_1 separates from the top and bottom channel walls. From the point where the neck starts to cave in vertically, the process is self-reinforcing and resembles the Rayleigh-Plateau instability [Plateau, 1873; Eggers, 1997]. For a similar case of single-droplet breakup, Leshansky and Pismen [2009] and Hoang et al. [2013] found the transition to this autonomous pinch-off to lie at a neck width of $0.5H$ in channels with near-unity aspect ratio.

The time scale ΔT for the breakup process is dominated by the advection time between the formation of the double interface in the junction, and the arrival of the droplet caps in the constriction. This time scale is independent of the capillary number but only depends on geometry, and the characteristic time scale $\tau \equiv H/U$. Compared to this time, the formation of the vertical neck and pinch-off happen quickly. Breakup is avoided when the entire volume of D_1 can drain ahead of the forming neck during the time ΔT.

In summary, droplet interaction in a Y-junction is dominated by a drainage flow driven by surface tension. The drainage, by which one droplet moves ahead of the other, is interrupted by the formation of a neck due to a difference in internal pressure between the droplets. In the constriction, the neck formation becomes self-reinforcing, and leads to pinch-off.

Dependence of the Fragment Volume on the Initial Offset

We now use our understanding of the physical processes that drive droplet breakup to model the dependence on capillary number and initial droplet offset. In particular, we describe the effect of these parameters on the volume of the breakup fragments, which we can quantitatively determine in both simulation and experiment. With V_1 the volume of droplet D_1 before entering the junction, we consider the volume V_{1a} of the first fragment of this droplet after passing the constriction. If $V_{1a} = V_1$, no breakup has occurred. If $V_{1a} < V_1$, breakup has occurred, and at least two fragments have been created.

Neck formation takes place behind the front cap of droplet D_2, and only after some time ΔT, during which the fluid in D_1 drains ahead of the neck. The volume V_{1a} is then made up of three distinct parts. These parts, as illustrated in Figure 5.6, are the volume V_{cap} of the front cap of D_1, the volume V_{δ_0} by which the first droplet was ahead of the second as they entered the junction, and the volume V_{drain} that drains ahead of the neck during the neck formation. We approximate the shape of the front cap D_1 by a half-ellipsoid of radius $W/4$ in the horizontal plane and half-height $H/2$, with a volume of $V_{\mathrm{cap}} \approx \frac{\pi}{24} W^2 H$. The volume V_{δ_0} depends on the initial offset δ_0 and the cross-sectional area of the inlet channel, and is approximated as $V_{\delta_0} \approx \frac{WH\delta_0}{\cos\alpha}$.

Since the relation between the offset and the front radius difference ΔR is unknown, an estimation of the drained volume V_{drain} proves difficult. However, we know that the drained volume will grow with the initial offset δ_0 (which determines the initial curvature difference) and the factor $\frac{\gamma}{\mu_d U} \equiv \frac{1}{\lambda Ca}$ (which drives the drainage flow based on that curvature difference). This suggests a draining volume of $V_{\mathrm{drain}} \approx C_1 \cdot \frac{\delta_0}{\lambda Ca}$, where C_1 is an unknown constant. The sum of the three volume components gives the estimate

$$V_{1a} \;=\; V_{\mathrm{cap}} + V_{\delta_0} + V_{\mathrm{drain}} \;\approx\; \frac{\pi}{12} W^2 H + \frac{WH}{\cos\alpha} \cdot \delta_0 + C_1 \cdot \frac{\delta_0}{\lambda Ca}. \tag{5.6}$$

From this relation, we get several predictions for the scaling of the first fragment volume: We

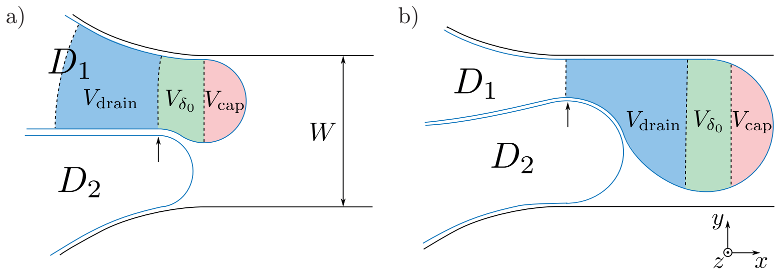

Figure 5.6: The final volume V_{1a} of the first fragment of D_1 after pinch-off comprises three parts: The volumes V_{δ_0} and V_{cap}, which are ahead of the neck before the start of necking (a), and the volume V_{drain} that drains through the neck before it pinches off completely (b). The neck forms behind the front cap of droplet D_2 (arrow).

expect the fragment volume to grow linearly with the offset, and with a steeper slope in the case of smaller capillary numbers. We define the critical offset δ_{crit} as the value of δ_0 at which the fragment volume reaches the full droplet volume. No breakup occurs for $\delta_0 \geq \delta_{\text{crit}}$. If the linear relation between initial offset and fragment volume is steeper at lower Ca, we expect δ_{crit} to be small at low Ca, and increase as Ca gets larger.

Scaling of the Fragment Volumes: Simulations

We test the analytical prediction using extensive numerical simulations with adaptively refined, highly resolved surface meshes (21,000 degrees of freedom) and at high temporal resolution (adaptive time steps around $10^{-3}\tau$) for 122 different combinations of capillary number and initial offset. The junction angles are $\alpha = 15°$ and $\alpha = 30°$, the capillary number range is $0.05 \leq Ca \leq 0.1$ and initial offsets are in the range $0 < \delta_0 < 1.4H$. For the entire range of offsets, the fragment volume V_{1a} displays the linear dependence on the initial offset that we predicted from the model (Figure 5.7a). In accordance with our expectations, the linear relation between initial offset and fragment volume is much steeper for small Ca than for large values of the control parameter. The critical offset δ_{crit} grows with the capillary number (Figure 5.7b). At small Ca, breakup only occurs for highly symmetric droplet configurations, whereas at large Ca ($Ca = 0.1$), we observe breakup even in situations where one droplet is ahead of the other by half of its length.

A higher junction angle decreases the range of offsets where breakup is observed. For junction angle $\alpha = 30°$, the values for the critical offset are smaller than for $\alpha = 15°$, since our Y-junction geometry leaves more space for droplet rearrangement and drainage at higher angles.

In addition to the behavior predicted by the analytic approximation, we find that for very small initial offsets, V_{1a} is not Ca-independent, but decreases with increasing Ca. Experiments

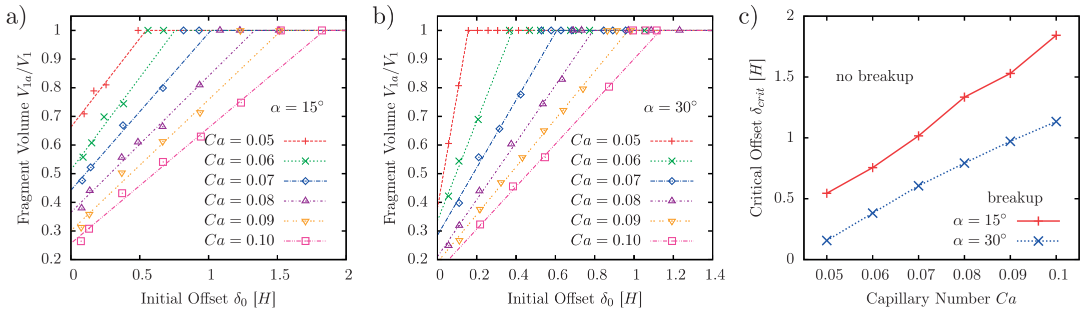

Figure 5.7: Simulation results for the relation between initial droplet offset and the resulting droplet breakup. *a), b)* Relative volume of the first droplet fragment after breakup, at a junction angle of $\alpha = 15°$ (a) and $\alpha = 30°$ (b). As the relative volume reaches one, no breakup occurs. Dashed lines show the piecewise linear trend. *c)* Critical offset at which no breakup occurs, as function of capillary number. The critical offset δ_{crit} is the offset δ_0 at which the linear extrapolation reaches 1.

confirm this behavior. The dependence on Ca for infinitesimal initial offsets, which the model for finite offsets does not capture, is likely a consequence of the fact that at higher capillary numbers, the droplet tip is more pointed and has a larger liquid film to its sides [Lac and Sherwood, 2009].

Scaling of the Fragment Volumes: Experiments

Experimental measurements complement the simulations. We perform experiments for the same Y-junction geometry as in the simulations, with the same junction angles and droplet size. By varying the flow rate, we measure capillary numbers in the range $0.007 \leq Ca \leq 0.035$. We do not actively control the offset between the two droplets coming in from the two branches prior to the Y-junction, but take advantage of the random variation in the spacing of droplets. By examining a large number of droplet pairs, this random variation in spacing conveniently allows us to obtain a large number of initial offset values δ_0 without the need for complicated active flow control. As the optical setup only allows imaging of the droplets in the horizontal plane, we measure the area of the droplets in this image plane as a measure for their volume. As seen in Figure 5.8, while there is a larger variation in the experimental data, they display the same behavior as the simulation results: The relative size of the first fragment grows linearly with the initial offset, and at a steeper slope for lower capillary numbers (Figure 5.8a,b). Consequently, the critical offset for droplet breakup grows with the capillary number, so that for larger capillary numbers, breakup is a common phenomenon, which occurs even for offsets on the scale of the droplet length (Figure 5.8c). As in the simulations, a larger junction angle results in a smaller critical offset.

Both the data from the simulation and from the experiments show the behavior that we expect from the theoretical scaling analysis. They explain how droplet breakup is more frequently observed at higher capillary numbers: The drainage flow, which prevents breakup, is driven by surface tension and scales with the inverse capillary number. For small capillary numbers, the

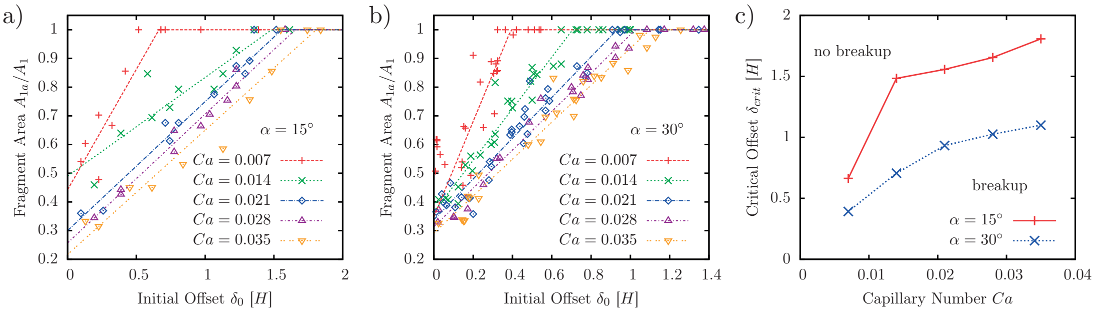

Figure 5.8: Experimental results for the relation between initial droplet offset and the resulting droplet breakup. *a), b)* Relative area of the first droplet fragment after breakup. As the relative area reaches one, no breakup occurs. Dashed lines show the piecewise linear trend. *c)* Critical offset at which no breakup occurs, as function of capillary number.

critical offset for breakup is small, so that it is statistically unlikely for a droplet pair to have an even smaller offset and break up. At larger capillary numbers, there is a wider range in offsets for which breakup is possible, so that droplet breakup becomes more and more frequent.

While we find great qualitative agreement between the fragment size data from the simulation and experiment, the experiments reveal an apparent quantitative discrepancy in the capillary number at which breakup is observed: Droplets break up at capillary numbers that are lower than the numerical predictions by a factor of $2-5$. This prefactor is only of order unity, but cannot be attributed to experimental uncertainties or numerical error alone. The potential influence of finite Reynolds number effects, which the simulation neglects, cannot account for this difference either: At the highest flow rate, $Q = 2\,\mathrm{mL/h}$ ($Ca = 0.035$), the local acceleration of the droplet front is $U/\tau^2 \approx 2\cdot 10^4\ \mathrm{m/s^2}$ for a fluid volume of roughly $H^3 \approx 15\,\mathrm{pL}$. The resulting inertial force of $43\,\mu\mathrm{N}$ is small compared to the $2.9\,\mathrm{mN}$ of the Laplace pressure acting on the droplet cap. Rather, we can show that the reason for the discrepancy is a nonequilibrium distribution of surfactants on the droplet interfaces, which is not part of the simulation.

For the surfactant used in the experiment (Krytox), the adsorption time to the interface is known to be on the scale of tens of milliseconds, and determined by the kinetics of the adsorption process rather than the bulk concentration [Riechers et al., 2016; Baret et al., 2009a]. The time scale of droplets passing the constriction, $\Delta T \approx 60{-}340\ \mu\mathrm{s}$, is two orders of magnitude smaller than that, so that we can assume that almost no additional surfactant is adsorbed during the process. This has two important consequences: First, since the total droplet area changes during the deformation process, the area concentration of surfactant and thus the surface tension changes accordingly. Second, the local expansion and contraction of the surface creates Marangoni stresses, which act along surface tension gradients in the interface plane. These Marangoni stresses counteract the deformation and thus prevent drainage, which promotes droplet breakup even at lower capillary numbers than those encountered in the simulation.

Quantitatively, the surfactant typically decreases surface tension by roughly a factor of two [Riechers et al., 2016], so that depletion of surfactants could effectively double the Laplace pressure in the droplet front cap. From the simulation, we extract the in-plane flow on the droplet surface, which redistributes surfactants and moves them to the rear of the droplets. The resulting flow field is shown in Figure 5.9, together with a color-coding for regions where the interface expands (red) or get compressed (blue). The total interfacial area of Droplet 1 expands by 32% during the droplet breakup (Droplet 2: 12%), with a much higher local expansion in the front cap (red areas in Figure 5.9). Even though the exact relation between surfactant density and surface tension is not known in detail, variations in surface tension are strong enough to effectively suppress the drainage mechanism that prevents droplet breakup.

The effect of the nonequilibrium surfactant distribution can be directly observed in the video material from the experiment: If the droplet gets too close to one side wall (as in the last panel of Figure 5.2b), a narrow sheet or finger of the droplet surface is swept away, breaking up

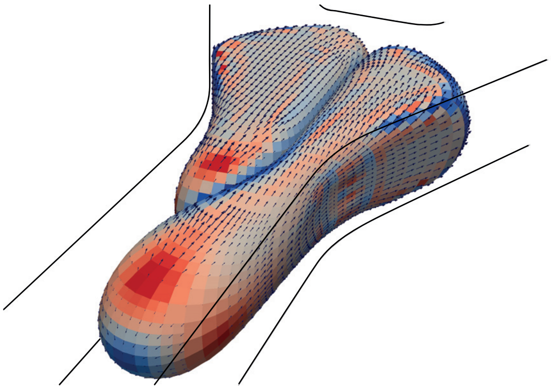

Figure 5.9: In-plane velocity divergence on the droplet surface, at $Ca = 0.06$ and $\delta_0 = 0.1H$. Images from the simulation. Colors show the in-plane divergence of the velocity on the droplet surface, in the range between $-3\tau^{-1}$ (blue) and $3\tau^{-1}$ (red). Vectors show the surface velocity relative to the mean velocity of D_1. The flow sweeps surfactants towards the back of the droplet, causing strong variations in the surfactant density.

into tiny droplets. This is not observed in simulations of droplets with Young-Laplace surface tension. If this effect of tip streaming [Stone, 1994], by which surfactant is removed from the droplet surface, occurs also in the upper parts of the channel, it is likely that the surfactant concentration is below the equilibrium concentration even before entering the junction.

Implications for Dense Emulsions

The two-droplet interactions are of practical interest when droplets in a dense emulsion enter a constriction. In dense emulsions, droplet breakup primarily results from the interaction of droplet pairs at the constriction entrance [Khor et al., 2017]. The droplet interaction in the Y-junction is a deterministic process, where the droplet configuration before the junction can be given purely in terms of the leading-edge offset. In contrast, droplet configurations in emulsions show a high variability and depend not only on initial droplet shapes in a droplet pair, but also on the configuration of more droplets upstream. This variability adds a stochastic component to the droplet interaction and breakup, which manifests itself as a bistable region in the relation between initial leading-edge offset and resulting breakup.

The impact of droplet interaction upstream of the constriction is two-fold: On one hand, the presence of additional droplets leads to an effectively lower angle at which droplet pairs approach the constriction, when one side of the microchannel is blocked by other droplets. We observe that this lower entrance angle promotes droplet breakup. On the other hand, droplets in a dense emulsion often reach the constriction in a staggered fashion [Gai et al., 2016b]. This staggering reduces the occurrence of highly symmetric droplet configurations that cause breakup.

Even though the flow situation upstream of the droplet pair differs, experimental results for the dependence of droplet breakup agree between the dense emulsion and the two-droplet interaction: The critical offset in the two-droplet interaction lies in the range between the maximum and minimum critical offsets observed in the dense emulsion at identical flow parameters. The experiments in this current paper give us the relation between initial offset, and the occurrence of breakup. Combining our knowledge of the critical breakup threshold from the two-droplet interaction $\delta_{\text{crit}}(Ca)$ (Figure 5.8c), and probability density $\rho(\delta_0)$ of initial offsets in the dense emulsion, we predict the breakup probability of droplets in a dense emulsion with the relation $p_{\text{break-up}} := \int_0^{\delta_{crit}} \rho(\delta_0)\, \mathrm{d}\delta_0$. For capillary numbers $Ca \leq 0.01$, the predicted breakup probability matches the experimental values from the emulsion within a 5% error. At higher capillary numbers ($Ca > 0.01$), the breakup probability in the emulsion experiment is higher than the prediction. Here the interaction of three or more droplets plays a significant role.

5.2.4 Conclusion

Combining an experimental study with numerical simulations and a theoretical analysis, we describe the breakup process of droplets entering a Y-junction. The droplet interaction follows a two-step process. In a first step, one droplet moves ahead of the other droplet, driven by an internal pressure gradient due to surface tension. In a second step, a neck forms in the first droplet, which breaks it up in an autonomous pinch-off process. When the drainage completes before the neck pinches off, breakup is avoided. The strength of the drainage process, and thus the occurrence of breakup, is determined by the offset between the droplets prior to entering the constriction.

A scaling analysis for the volume of the breakup fragments reveals a linear dependence between the volume of the first breakup fragment and the initial leading-edge offset between the droplets, which is found in both simulations and experiments. The linear relation determines the range of initial droplet offsets that result in droplet breakup. We report this range as a function of the capillary number Ca and for two different junction angles α.

Due to the timescale of the attachment kinetics of surfactants vastly exceeding the time scale of droplet advection and breakup, the surfactant concentration on the droplet surfaces is not in equilibrium, even at surfactant concentrations far above the critical micelle concentration (CMC). This induces both an overall change of the surface tension, and in-plane Marangoni stresses, which inhibit drainage and promote breakup. The nonequilibrium surfactant distribution results in a quantitative difference in the capillary number at which droplet breakup is observed. Experiments show droplet breakup at a smaller capillary number than the simulations, which do not model the surfactant dynamics. These findings stress the importance of gaining insights into the adsorption and redistribution processes of surfactants, which are an open field of ongoing research [van Hunsel et al., 1986; Stone and Leal, 1990; Song et al., 2006; Baret et al., 2009a; Riechers et al., 2016; Ponce-Torres et al., 2017].

Using our experimental data on the critical offset for droplet breakup in a Y-junction, we predict the probability of droplet breakup in dense emulsions at capillary numbers up to $Ca \simeq 10^{-2}$ within a 5% error. This quantitative agreement supports the description of emulsion droplet breakup as a deterministic process resulting from two-droplet interaction, where the primary source of stochasticity is the multi-droplet interaction upstream of the constriction that sets the leading-edge offset between droplets.

5.2.5 Appendix

Magnitude of the Relative Flow due to the Difference in Front Radius

For rectangular channels of aspect ratios H/W near unity, the relation between streamwise pressure gradient $\partial_x p$ and approximate mean flow velocity U is

$$U = -0.035 \frac{WH}{\mu} \cdot \partial_x p \tag{5.7}$$

where μ is the dynamic viscosity of the fluid inside the channel. This result can be reached by numerically evaluating the series representation of the analytic flow profile in the duct [Spiga and Morino, 1994].

Consider now the case of the two front caps of the droplets lying next to each other with difference in horizontal front radius $\Delta R \equiv R_1 - R_2 \ll 1$, each occupying about half of the width of the channel ($R_1 \approx R_2 \approx W/2$). With the ambient pressure the same between the droplets, the internal pressure will be higher in D_2 than D_1 by

$$\Delta p_{21} = \gamma \left(\frac{1}{R_2} + \frac{1}{H/2} \right) - \gamma \left(\frac{1}{R_1} + \frac{1}{H/2} \right) \approx \frac{\gamma \Delta R}{(W/2)^2}, \tag{5.8}$$

according to the Young-Laplace equation (5.5), with $\Delta p_{ij} \equiv p_i - p_j$.

This pressure difference exists at the front cap of the droplets, where it is supported by the local curvature of the interface, but not further back, where the common double interface between the droplets runs straight. This is the case at about a distance W from the droplet fronts, such that each droplet has an internal pressure gradient of

$$\partial_x p_{rel} = \mp \frac{\Delta p_{21}}{2W} = \mp \frac{2\gamma \Delta R}{W^3} \tag{5.9}$$

relative to the common mean internal pressure (with negative sign for D_1 and positive sign for D_2).

The pressure gradient drives a flow u_{rel} in x-direction, relative to the common mean flow U, with

$$u_{rel} = -0.035 \frac{WH}{2\mu_d} \cdot \partial_x p_{rel} = \pm 0.029 \cdot \frac{1}{\lambda Ca} \frac{\Delta R}{W} \cdot U, \tag{5.10}$$

(with positive sign for D_1 and negative sign for D_2) with the velocity-pressure-relation (5.7), the channel aspect ratio $W/H = 1.2$. Only small deviations from this relation are expected due to the opening angle, aspect ratio of the channels and additional effects. The velocity profile in Figure 5.4c shows the relative flow in each half of the channel superimposed with the mean flow of strength U.

5.3 Summary

We investigated the breakup of droplets that occurs when droplets enter a constricted channel. From experiments in concentrated emulsions (Section 5.1), we found that the breakup is determined primarily by the leading-edge offset in droplet pairs, and therefore depends largely on the interaction of two droplets. We then studied the isolated system of two droplets (Section 5.2). By simulating the droplet interaction numerically, we retrieved the pressure field in the system, which unveiled the physical mechanism behind droplet breakup. The scaling with capillary number and droplet offset is supported by simulation and experiments. Quantitative comparison between simulation and experiment suggests that surfactant-induced Marangoni stresses interfere with the breakup process and promote droplet breakup.

6 Dielectrophoretic Sorting of Droplets

Contents

6.1 Rational Design of a High-Throughput Droplet Sorter 98
6.1.1 Results and Discussion 101
6.1.2 Conclusions 110
6.1.3 Materials and Methods 111
6.1.4 Appendix 112
6.2 High Throughput Multiplexed Fluorescence Activated Droplet Sorting . . . 114
6.3 Summary 117

The main part (Section 6.1) of this work has been carried out in collaboration with Thomas Beneyton (CNRS, U Bordeaux), Jean-Christophe Baret (CNRS, U Bordeaux) and Tobias M Schneider (EPFL). JCB and TMS conceived the research. SS (this author) performed the numerical simulations under supervision of TMS. TB carried out the experiments under supervision of JCB. This part is currently in the manuscript stage, for submission as Schütz et al. [2018a]. All authors contributed to the writing of the manuscript. With permission from the coauthors, we report here the full text of the manuscript, in its preliminary form and with changes to match the formatting.

A second part (Section 6.2) has been carried out in collaboration with Ouriel Caën (U Paris Descartes), Mani S S Jammalamadaka (U Paris Descartes), Jérémy Vrignon (CNRS, U Bordeaux), Philippe Nizard (U Paris Descartes), Tobias M Schneider (EPFL), Jean-Christophe Baret (CNRS, U Bordeaux) and Valérie Taly (U Paris Descartes). OC and MJ carried out the experiments. SS performed the numerical simulations and analytical estimates. This part is currently submitted and under review as Caen et al. [2018]. Since SS contributed only part of the text, we summarize the results here, but refer to the article for the full text.

Sorting by *dielectrophoresis* [Pohl, 1958] has become a standard tool in droplet-based microfluidic applications. Dielectric droplets are actuated by strong electric fields, which generate Maxwell stresses on the droplet interface.

In Section 6.1, we explore the limits of droplet actuation by electric fields. Based on simulations of droplet stability in strong electric fields (see Section 4.8) and analytical calculations, we analyze droplet actuation in sorting geometries, and develop design principles for more gentle droplet actuation. This work is aimed at extending the range of droplet sorting to low surface tension applications, and increasing throughput and reliability of sorting.

In Section 6.2, we describe multiplexed sorting with multiple sorting electrodes and outlet channels. We show how the voltage applied to the sorting electrodes can be adjusted to reliably sort droplets of different radii.

6.1 Rational Design of a High-Throughput Droplet Sorter

Simon S Schütz[1], Thomas Beneyton[2], Jean-Christophe Baret[2] and Tobias M Schneider[1]

[1] Emergent Complexity in Physical Systems Laboratory (ECPS), École Polytechnique Fédérale de Lausanne (EPFL), Station 9, 1015 Lausanne, Switzerland

[2] Soft Microsystems, Centre de Recherche Paul Pascal, Unité de Recherche 5031, CNRS, University of Bordeaux, 33600 Pessac, France

Abstract

The high-throughput selection of individual droplets is an essential function in droplet-based microfluidics. Fluorescence-activated droplet sorting is achieved using electric fields triggered at rates up to 30 kHz, providing the ultra-high throughput relevant in applications where large libraries of compounds or cells must be analyzed. To achieve such sorting frequencies, electrodes have to create an electric field distribution that generates maximal actuating forces on the droplet while limiting the induced droplet deformation and avoiding disintegration.

We propose a metric characterizing the performance of an electrode design relative to the theoretical optimum and analyze existing devices using full 3D simulations of the electric fields. By combining parameter optimization with numerical simulation we derive design guidelines and propose optimized electrode configurations. When tested experimentally, the optimized design show significantly better performance than the standard designs.

Droplet-based microfluidics is a powerful technology for the miniaturization and automation of biochemical assays at a high throughput [Theberge et al., 2010]. The technology is key in a wide range of applications, for example for protein engineering [Agresti et al., 2010; Obexer et al., 2016; Romero et al., 2015], cell and microorganism screening [Brouzes et al., 2009; Eyer et al., 2017; Beneyton et al., 2016], sequencing [Klein et al., 2015; Zilionis et al., 2017] or molecular diagnostics [Pekin et al., 2011]. Sorting is achieved by addressing individual droplets and actuating them into different microchannels [Baret et al., 2009b; Agresti et al., 2010; Romero et al., 2015; Xi et al., 2017]. The fastest sorting speeds to date are achieved by actuating droplets using electric fields [Ahn et al., 2006b; Baret et al., 2009b; Romero et al., 2015]. The principle of sorting is based on *dielectrophoresis* (DEP): For droplets that have a dielectric contrast with the continuous phase, a non-uniform electric field leads to a net force on the droplet. This force then allows steering droplets across the streamlines of the background flow and into the desired outlet channel.

Two effects control the performance of a droplet sorting device: First, the electrical actuation moves droplets across streamlines of the flow. The deflection of the droplet is a function of the magnitude of the field and of duration the droplet is exposed to the field while being advected downstream. Second, the geometry of the microchannel ensures that the droplets deflected to different streamlines are actuated into the right outlet. Based on these considerations, many different droplet sorters have been designed [Ahn et al., 2006b; Baret et al., 2009b; Agresti et al., 2010; Sciambi and Abate, 2015; Gielen et al., 2016; Obexer et al., 2016; Frenzel and Merten, 2017; Girault et al., 2017], reaching sorting throughputs of up to 30 kHz [Sciambi and Abate, 2015]. A part of the rich *genealogy* of sorter designs is presented in Figure 6.1. Over the past years, these devices were adapted and used to match the constraints of the biological assays

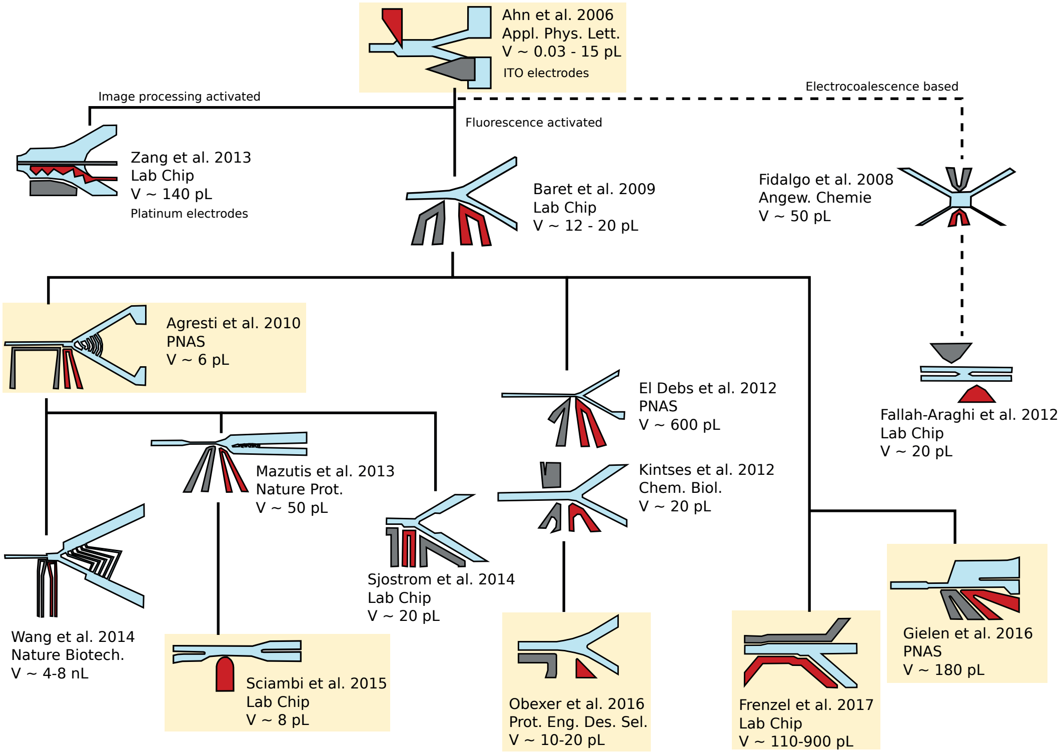
Ahn et al. 2006
Appl. Phys. Lett.
V ~ 0.03 - 15 pL
ITO electrodes
Image processing activated
Electrocoalescence based
Fluorescence activated
Zang et al. 2013
Lab Chip
V ~ 140 pL
Platinum electrodes
Baret et al. 2009
Lab Chip
V ~ 12 - 20 pL
Fidalgo et al. 2008
Angew. Chemie
V ~ 50 pL
Agresti et al. 2010
PNAS
V ~ 6 pL
El Debs et al. 2012
PNAS
V ~ 600 pL
Fallah-Araghi et al. 2012
Lab Chip
V ~ 20 pL
Mazutis et al. 2013
Nature Prot.
V ~ 50 pL
Kintses et al. 2012
Chem. Biol.
V ~ 20 pL
Sjostrom et al. 2014
Lab Chip
V ~ 20 pL
Wang et al. 2014
Nature Biotech.
V ~ 4-8 nL
Gielen et al. 2016
PNAS
V ~ 180 pL
Sciambi et al. 2015
Lab Chip
V ~ 8 pL
Obexer et al. 2016
Prot. Eng. Des. Sel.
V ~ 10-20 pL
Frenzel et al. 2017
Lab Chip
V ~ 110-900 pL

Figure 6.1: Following the seminal designs by Ahn et al. [2006b] and Baret et al. [2009b], many different sorters have been developed over the past decade. Electrode geometries have been guided by experimental trial and error, but none is based on rationally optimizing the field distribution in order to maximize droplet actuation. We analyze the highlighted sorter designs, and propose new, improved designs based on our findings.

performed in the droplet format. However, to the best of our knowledge, these devices were optimized by experimental trial and error, and none of the existing sorting devices are based on rationally optimizing the electrode geometry.

A seemingly straightforward way to make sorting systems more effective is to increase the strength of the electric fields, inducing a larger net force acting on the droplet. Thereby, the necessary deflection is achieved in shorter time, and higher sorting frequencies become accessible. However, this solution is not reliable: while the net force in dielectrophoresis is given by the field gradients, the field itself deforms the droplet without displacing the center of mass. When the field gets too strong, droplets disintegrate [Taylor, 1964]. An effective sorting geometry therefore needs to exert a strong actuation force on the droplet, without exceeding limits in the absolute field strength.

Here, we focus on the impact of the electrode design on the actuation of droplets in sorting devices. We first discuss physical limitations for high-throughput sorting, develop a metric characterizing the performance of an electrode design relative to the theoretical optimum and analyze existing devices. Based on fully resolved 3D simulations of the electric field together with parameter optimization, we then suggest rational design principles and propose optimized electrode designs that reduce the Maxwell stress on droplets during sorting. Experimental tests demonstrate the superior performance of the novel electrode designs. The proposed electrodes can easily be integrated and do not complicate the device fabrication compared to alternative inferior designs. Because the deformation of droplets in electric fields is counteracted by interfacial tension, optimized electrode designs that generate more gentle actuation forces are particularly important for applications that require the sorting of droplets with low surface tension [Kintses et al., 2012; Eastburn et al., 2014; Colin et al., 2015; Romero et al., 2015; Obexer et al., 2016].

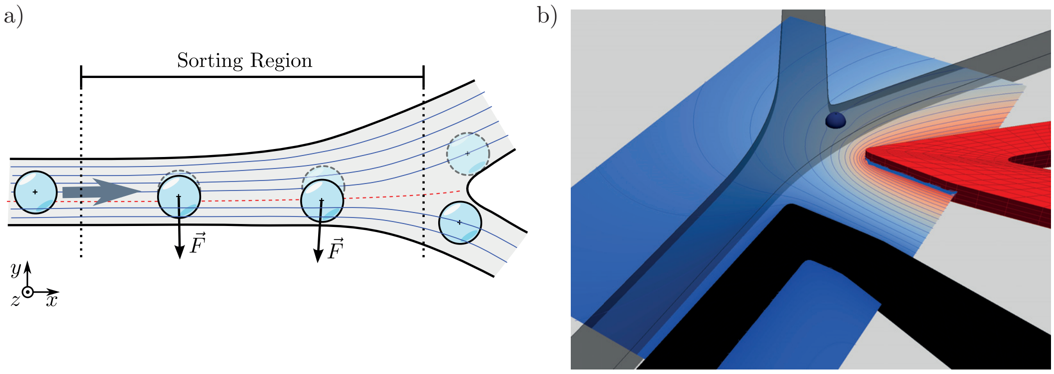

Figure 6.2: Mechanism of dielectrophoretic sorting. *a)* In the sorting region, the dielectrophoretic force $\vec{F}$ moves a droplet perpendicular to the streamlines, so that it exits through a different output channel. *b)* We determine the electric potential and field from a 3D boundary-element simulation. Visualized is the field at half-height in the channel.

6.1.1 Results and Discussion

The functioning principle of DEP droplet sorting is illustrated in Figure 6.2: In a flow region upstream from a microchannel junction, a dielectrophoretic force $\vec{F}$ is applied to a droplet when the electric field is activated. This force causes the droplet to drift across stream lines, and be guided into one outlet channel. The asymmetric design of the channel ensures that without an electric field the droplet is guided into the other channel. Selectively applying a voltage between the active and the ground electrode thereby allows to sort droplets.

The dielectric force emerges from the interaction of the electric field with dipoles induced in the droplet phase. The force $\vec{F}$ thus grows with the gradient $\nabla|\vec{E}|^2$ of the square of the electric field $\vec{E}$, and is independent of the field polarity. For small, sperical droplets, the force is given by [Pohl, 1958]

$$\vec{F} = 2\pi\varepsilon_0\varepsilon_c K R^3 \nabla|\vec{E}|^2 \tag{6.1}$$

with $K \equiv \frac{\varepsilon_d - \varepsilon_c}{\varepsilon_d + 2\varepsilon_c}$. Here, ε_0, ε_c, ε_d, and R are the vacuum permittivity, the relative permittivity of the continuous and droplet phase, and the droplet radius, respectively. Corrections to this small-droplet approximation are discussed in Appendix 6.1.4.

In response to the force, the droplet drifts across the stream lines. At near-unity viscosity ratio between droplet and continuous phase, the drift velocity is $U_{\text{drift}} \approx F/(5\pi\mu R)$, with F the cross-stream component of the dielectric force, and μ the viscosity of the outer fluid [Guyon et al., 2001]. For reliable sorting, the droplet needs to be displaced by approximately one droplet diameter, which takes a time $T = 2R/U_{\text{drift}}$. The maximum sorting frequency therefore scales as

$$f_{\max} \approx \frac{1}{T} = \frac{F}{10\pi\mu R^2}. \tag{6.2}$$

The sorting frequency is proportional to the dielectrophoretic force on the droplet, and inversely proportional to the viscosity of the continuous phase. If the actuation force varies along the path of the droplet, the time-averaged force determines the sorting frequency.

The force on the droplet may be increased by increasing the field gradient $\nabla|\vec{E}|^2$. However, there is a critical upper limit for the field strength: The dielectric force moving the droplet is caused by electric Maxwell stresses at the interface. In a field gradient the Maxwell stresses vary over the droplet surface resulting in the dielectrophoretic net force. The stress everywhere points outward of the droplet and deforms the initially round droplet. Surface tension counteracts the deforming Maxwell stresses, but when the field strength surpasses a critical value E_{crit}, surface tension becomes insufficient to maintain the round droplet shape, the droplet deforms and eventually disintegrates in the surrounding shear flow [Taylor, 1964; Sherwood, 1988].

Quantitatively, the relative strength of the Maxwell stress compared to surface tension is given by the electrical Bond number $Bo_E := \frac{\varepsilon_0 \varepsilon_c |\vec{E}|^2 R}{\gamma}$, with γ the surface tension coefficient. The Maxwell stress surpasses the surface tension at a Bo_E near unity, so that the critical field strength scales with $E_{\text{crit}} \propto \sqrt{\frac{\gamma}{\varepsilon_0 \varepsilon_c R}}$. Consequently, the critical field strength is particularly small for low surface tensions and large droplet radii.

The largest possible field gradient is achieved for a field increasing from zero to the critical strength E_{crit} across the droplet diameter $2R$. With eq. (6.1) this yields an upper bound $F_{\text{max}} = 2\pi\varepsilon_0\varepsilon_c K R^3 \frac{E_{\text{crit}}^2}{2R}$ for the force on a droplet. If one could generate arbitrary electric fields, droplets could be actuated with this maximum force. However, the field distribution is not arbitrary as the field has to satisfy Maxwell's equations and is generated by electrodes of fixed geometry. Consequently, the aim is to design electrodes such that the actuating force given by the gradient $\nabla|\vec{E}|^2$ is maximized along the path while the field strength remains below a maximum value E_{max}.

To quantify the efficiency of an electrode design, we normalize the spanwise force component $|F_y|$ acting acting on the droplet at each location, by the maximum force F_{max} This yields the non-dimensional *DEP force*

$$\xi := \frac{|F_y|}{F_{\text{max}}} = \frac{2R|\partial_y E^2|}{E_{\text{max}}^2}, \tag{6.3}$$

which quantifies how closely the actual force on a droplet at a given location approaches the maximum force. ξ can be written in terms of the field strength with E_{max} the maximum field in the microchannel. For a given electrode geometry the electric field grows proportionally with the voltage applied to the electrodes. The metric ξ is thus independent of the absolute field strength but characterizes the efficiency of the field geometry. In practice the voltage can be increased until E_{max} reaches the critical value E_{crit} for the specific droplet surface tension, size and material properties.

An efficient sorter will apply the maximum possible force over the entire length of the sorting segment to move the droplet across the stream lines. Outside this segment, forces should be minimized, so that subsequent droplets and other parts of the setup are not affected and droplets can be addressed individually. To quantify the overall performance of the sorter, we thus define the *DEP efficiency*

$$\Xi := \frac{1}{|S|} \int_S \xi \, \mathrm{d}s, \tag{6.4}$$

which measures the average DEP force along the sorting segment S ranging from the location where ξ exceeds a threshold value of 1%, to the bifurcation between the two outlet microchannels. The DEP efficiency is a dimensionless measure between zero and one, which describes the overall actuation of a droplet relative to the maximum possible actuation for this droplet. Both the location-dependent DEP force ξ and the integrated efficiency Ξ are independent of the absolute size of the system and material properties of the liquids. They are performance metrics characterizing the efficiency of the electrode and sorter geometry and will thus be used for optimizing electrode designs.

To determine the DEP force and efficiency for a given system, we perform a 3D boundary-element simulation of the electric field around the sorting electrodes. The boundary-element method solves the electrostatic Laplace equation by finding the electric potential and flux on the surface of the sorting electrodes, and then extends the field into the volume. Details of the method are given in the Materials and Methods section. As we will discuss later, 3D features of the electric field play a vital role in the sorting process, so that a fully resolved 3D computation is indispensable. From the 3D simulation, we calculate the electric field and its gradients in a 2D plane at half-height in the channel (Figure 6.2b).

We analyze the efficiency of several electrode designs (highlighted in Figure 6.1) that have been developed in the past years. Figure 6.3 presents the DEP force ξ in the channel midplane, which we extract from a 3D simulation of the field. The normalization ensures that the DEP force never exceeds 1 inside the microchannel (gray). The force ξ along the approximate path of a droplet (red dashed line) is shown in the upper panel together with the integrated performance metric Ξ.

The design by Ahn et al. [2006b] (Figure 6.3a) was the first design to demonstrate DEP droplet sorting, and uses two different layers in the design for the microchannels and the electrodes. The subsequent sorters have electrodes on the same level as the microchannels. The sorter by Agresti et al. [2010] (b) places an active electrode parallel to the sorting segment, and slows droplets during sorting by widening the channel. Sciambi and Abate [2015] (c) focus on reducing the shear on droplets, which allows them to increase the flow rate. Their electrode is close to the microchannel, but rounded, which is less efficient. The recent designs used by Gielen et al. [2016] (d), Obexer et al. [2016] (e) and Frenzel and Merten [2017] (f) have long active electrodes, which are very effective. The efficiency of the design by Obexer et al. is low because a strong and constant actuation force on droplets is reached only after the sorting junction. These sorter designs have been developed over a time period of roughly a decade (2006-2017) and show a trend of increasing efficiency, with Gielen et al. reaching the highest efficiency at $\Xi = 0.161$.

The performance metric Ξ allows to quantitatively compare the efficiency of different electrode geometries and design better electrodes that substantially outperform previous sorter designs. Well performing existing sorters have an extended flat electrode parallel to the channel as well as shielding electrodes. We will first consider the optimal shape of a single active electrode and then discuss further benefits of increasing the device complexity by additional shielding electrodes. This rational design procedure yields efficiency improvements of almost 100% over the latest design by Gielen et al., and optimized electrodes significantly outperform classical designs in experimental tests.

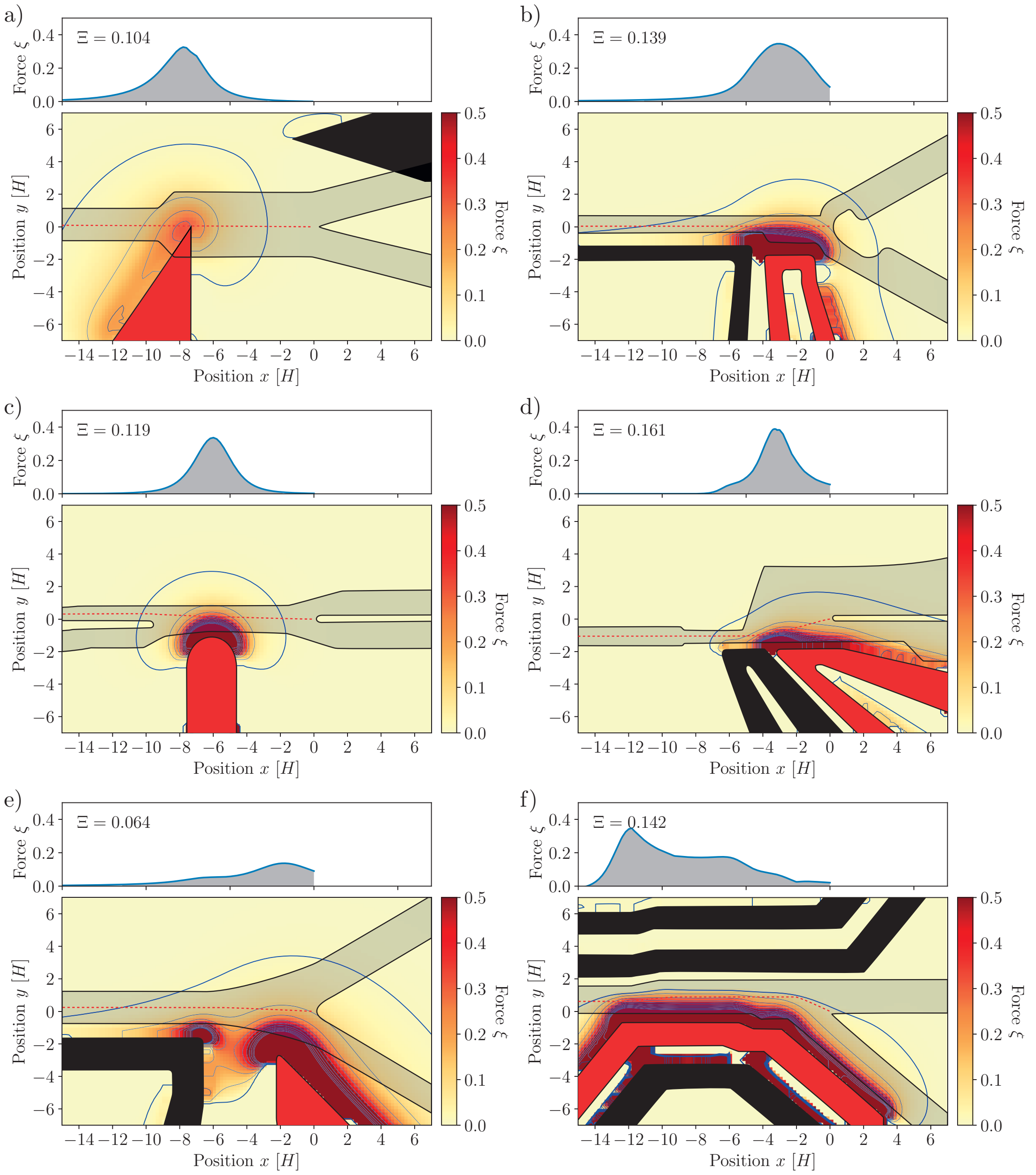

Figure 6.3: Relative DEP force ξ around the electrode designs of *a)* Ahn et al. [2006b], *b)* Agresti et al. [2010], *c)* Sciambi and Abate [2015], *d)* Gielen et al. [2016], *e)* Obexer et al. [2016] and *f)* Frenzel and Merten [2017]. The thick contour line is $\xi = 10^{-2}$. The dashed line in the channel center estimates the dividing streamline between the outlets, along which we average the DEP force ξ to get the total DEP efficiency Ξ. The top panel shows the DEP force ξ along the droplet path and the total DEP efficiency Ξ. The electrodes in Ahn's design are coated on a plane below the microchannel; all other designs have electrodes next to the channel and of equal height H. The channel height is *a)* $H = 25\,\mu$m, *b)* $H = 25\,\mu$m, *c)* $H = 30\,\mu$m, *d)* $H = 80\,\mu$m, *e)* $H = 21\,\mu$m, *f)* $H = 75\,\mu$m.

For a straight, rectangular microchannel of constant cross-section and aspect ratio 2, we consider one active electrode parallel to the channel with grounded counter-electrodes at infinity, as shown in Figure 6.4a. The straight electrode causes a strong deflection force along its whole length (Figure 6.4b), with an efficiency $\Xi = 0.212$ that is 32% higher than what the existing designs achieve. The side view on the electrode (Figure 6.4c) reveals the reason for the large force along the whole electrode: The field lines spread in the out-of-plane direction, which leads to the high field gradients that attract droplets. When designing a sorting device in a 2D top view, one easily overlooks this 3D effect of the electric field, which cannot be captured by any 2D analysis of the device. Free parameters in the design of this simple bar electrode are the electrode length L, and its distance D_E from the channel center line. We optimize the two geometric parameters L and D_E to maximize the efficiency Ξ (Figure 6.4d). The distance

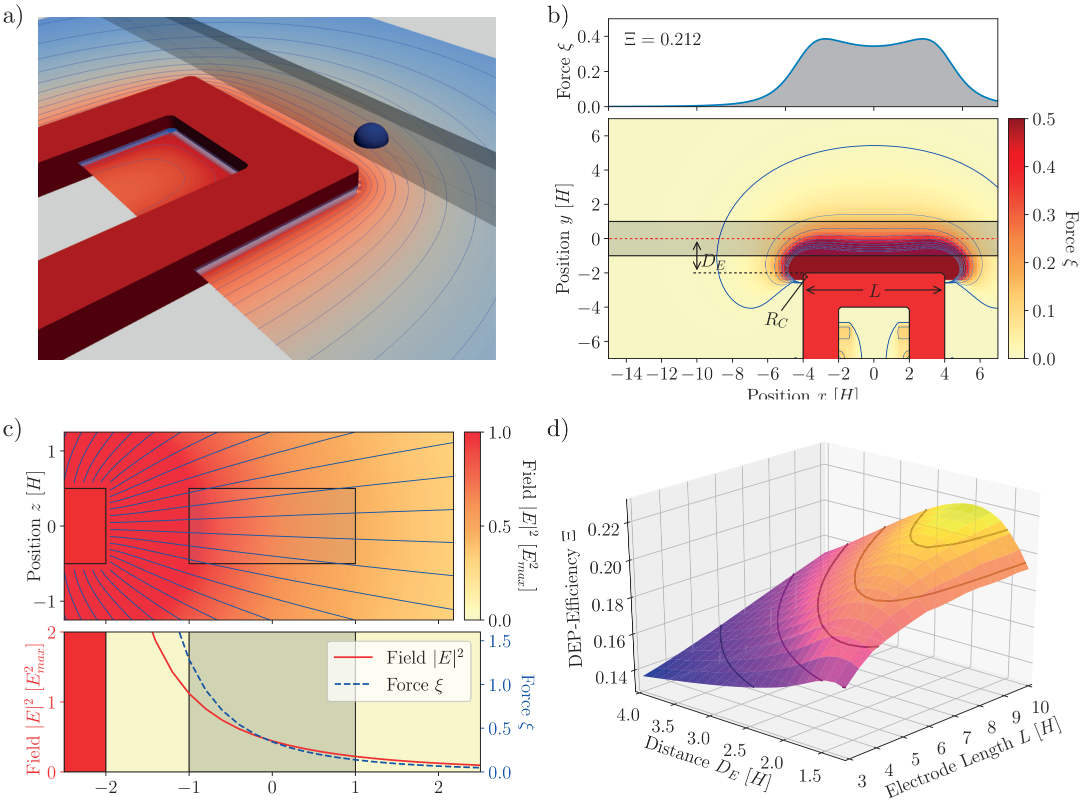

Figure 6.4: Sorting with a simple bar electrode. *a)* 3D geometry of an electrode of height H and length $L = 8H$, next to a microchannel of height H and width $2H$. The droplet radius is $R = H/2$. *b)* Deflection force ξ on a droplet traveling through the microchannel shown in *a)*. Contours and DEP force ξ as in Figure 6.3. *c)* Side view of electrode and microchannel. The deflection force is dominated by the spread of field lines in the z-direction *(top)*. With the distance from the main electrode, the force ξ decays faster than the field $|E|^2$ *(bottom)*. *d)* The sorting efficiency changes with the electrode length L and distance D_E between electrode and channel center. Longer electrodes are more efficient, and $D_E \approx 2H$ gives the highest sorting efficiency for long electrodes.

between electrode and channel center has a clear optimum at $D_E \approx 2H$: The field decays with the distance from the electrode, so that the actuation force is stronger when the droplet is close to the electrode. However, in very close proximity to the electrode, the field shape is set by the electrode height, and the actuation force gets weaker. The optimum distance D_E is thus on the scale of the electrode height. Long electrodes perform better because they offer a longer region of strong droplet actuation, relative to regions of stray field where droplet actuation is suboptimal. In practice, to maintain a high sorting frequency, a sorter with a long electrode must be operated at a high flow rate that poses other challenges. We therefore limit the electrode length to $8H$, where further efficiency gains due to longer electrodes become marginal.

An appropriately dimensioned active electrode with ground at infinity alone provides a 32% performance increase. However, far reaching stray fields are created, that may have unwanted side-effects on parts of the microfluidic chip not associated with the droplet sorter. To integrate many sorters in a chip and address individual sorters while minimizing crosstalk, shielding electrodes are necessary. Such additional electrodes at ground potential not only help isolate the sorter from the remainder of the microchip, but can also further increase the sorting efficiency.

For a main electrode of length $L = 8H$, ground electrodes as shown in Figure 6.5a reduce the length of the sorting segment by 30% and increase efficiency by roughly the same amount, to $\Xi = 0.270$. This correponds a 68% improvement over the reference design by Gielen et al., where half of the improvement is due to the added shielding electrodes. By reducing stray fields, the shielding causes a step-like transition from zero to the full actuation force of the straight electrode. This effect is enhanced by sharp corners of the electrodes (Figure 6.5b).

In the design of the shielding, it is critical to leave a gap right across the main sorting electrode:

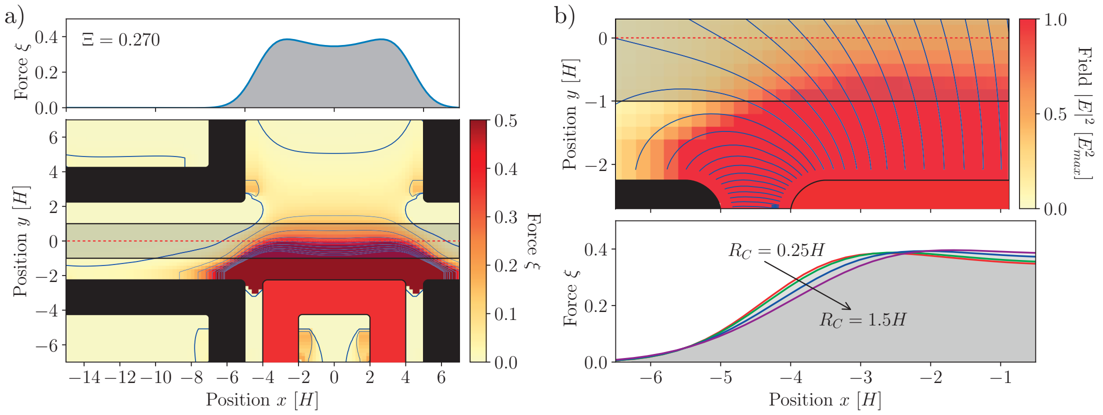

Figure 6.5: Sorting with a shielded electrode. *a)* Deflection force ξ of a simple electrode of height H and $L = 8H$, $D_E = 2.25H$. Contours and DEP force ξ as in Figure 6.3. *b)* The field is particularly strong at the corners of the electrode. Sharp corners increase the force on the droplet locally, and lead to an overall higher efficiency.

Here, some space is required so that the field emanating from the main electrode can spread freely.

The combination of one active electrode and appropriately design shielding electrodes allows for significant efficiency improvements. Further efficiency increases are possible when increasing the complexity of the design and adding a second active electrode. An active electrode of the same polarity as the main sorting electrode, but on the opposite side of the channel (Figure 6.6a) creates an electric field in the channel that partially cancels the field of the main electrode. This reduces the field strength in the channel, whereas the field gradient remains strong. The highest sorting efficiency ($\Xi = 0.290$) is reached when the voltage of the second

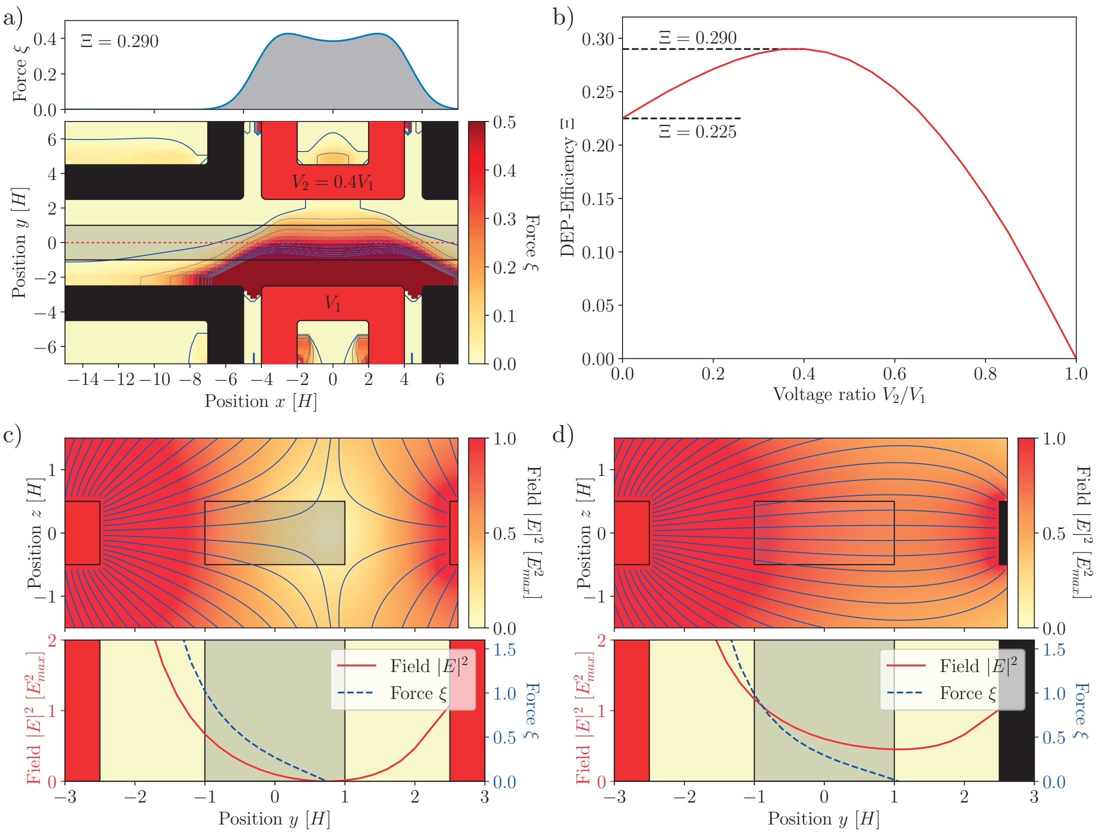

Figure 6.6: Sorting with two active electrodes. *a)* Deflection force of a pair of two active electrodes at a voltage ratio $V_2/V_1 = 0.4$, at $L = 8H$, $D_E = 2.5H$. Contours and DEP force ξ as in Figure 6.3. *b)* The overall efficiency depends on the voltage ratio. The highest efficiency is reached at $V_2/V_1 \approx 0.4$; for higher or lower voltages on the second electrode, the efficiency decays quickly and is often lower than in the complete absence of the second active electrode. *c)* Side view of electrode and microchannel at $V_2/V_1 = 0.7$. The field lines spread in the vertical z-direction, creating a region where the field almost vanishes *(top)*. The field gradient remains high, so that a high deflection force can be reached *(bottom)*. *d)* Side view of electrode and microchannel at $V_2 = 0$. When the second electrode is present, but not active, the field gradient is weaker, so that the efficiency of the sorter decreases.

electrode is roughly ~ 40% of the main electrode's voltage (Figure 6.6b,c). If the secondary voltage is higher, the field minimum moves into the channel, so that the force on the droplet decreases. If the secondary voltage is too low (or zero, as for the shielding electrodes), field lines do not spread in the vertical direction (Figure 6.6d) and the field gradient is reduced. Choosing the optimal voltage for a second active electrode further improves the sorter efficiency, but the increase is less dramatic than the increase due to suitably optimizing a single active electrode or introducing shielding electrodes. Furthermore, a second electrode at a different potential increases the complexity of the device so that a single active electrode might be the best choice in most applications. However, a second active electrode may be very beneficial if not only the electrodes but also the channel design is adapted. If the channel and electrodes are chosen to be symmetric, droplets in the channel center only need to be moved by half the distance for reliable sorting, which effectively doubles the sorting frequency. Such a symmetric design also underlies the multiplexed sorter discussed by Girault et al. [2017].

Based on performance metrics for the efficiency of dielectrophoretic sorters, we have optimized electrode designs and shown that efficiency improvements of 32% relative to the best existing designs can be achieved by a single active electrode, that the improvement increases to 68% when appropriate shielding is added, and that a 77% improvement can be achieved using a second active electrode, which complicates the device significantly. Relative to the common electrode design by Obexer et al., multifold efficiency improvements are achieved. We experimentally compare the performance of the optimized electrode designs to the common setup. Table 6.1 presents parameters of the tested electrodes including efficiency, sorting segment length and required electrode voltage.

To characterize the performance of the electrode shape independent of flow-related parameters, we perform experiments for fixed microchannel geometry, flow rates, droplet volume and sorting frequency. Electrode and microchannel designs are taken from Obexer et al. [2016] (Figure 6.3e) and compared to the bar electrode of length $L = 8H = 196\,\mu$m without and with local shielding (Figures 6.4a and 6.5a). Width and height of the microchannel and droplet diameter are $50\,\mu$m, $24\,\mu$m, and $25\,\mu$m, respectively. We apply a 20 kHz AC field at a voltage between 0 and 1 kV. As experiments for a second active electrode (Figure 6.6a) did not show a clear advantage over the single electrode with shielding, we do not present experimental

Design	Efficiency Ξ	Length $\lvert S\rvert$ $[H]$	Voltage V_1 $[E_{crit}H]$
Reference design (Fig. 6.3e)	0.064	11.4	6.4
Optimized bar electrode (Fig. 6.4a)	0.212	17.5	6.0
Electrode with shielding (Fig. 6.5a)	0.270	12.5	5.0
Two active electrodes (Fig. 6.6a)	0.290	13.0	6.6

Table 6.1: Efficiency, length of the sorting segment, and electrode voltage for the reference design by Obexer et al. [2016], and the improved electrode designs with an electrode length of $L = 8H$. At a similar sorting segment length and electrode voltage, the new designs show a vastly higher efficiency.

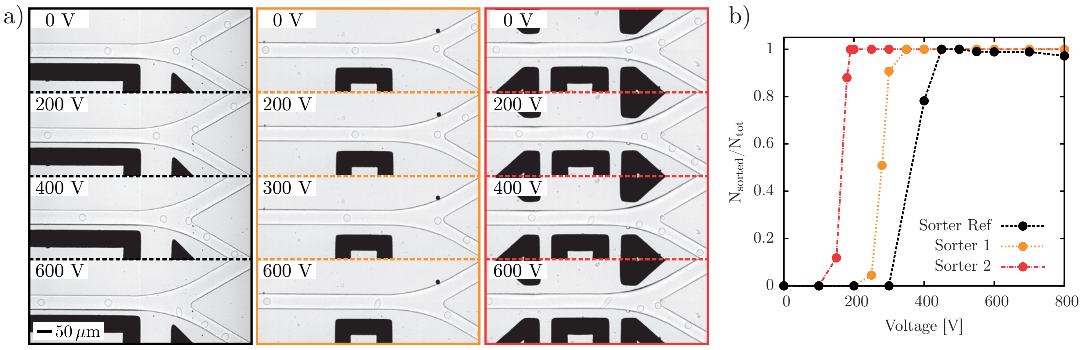

Figure 6.7: Droplet sorting at different electrode voltages, for the reference sorter by Obexer et al. [2016] (Sorter Ref), and our new designs without (Sorter 1) and with (Sorter 2) local shielding. *a)* Typical droplet trajectories at the different electrode voltages. *b)* Success rate of sorting for the different designs. The new designs sort droplets at a low voltage, making them easy to integrate and to operate at high throughput.

results on this very complex design.

By varying the voltage applied to the sorting electrode, we determine the voltage at which all droplets are correctly sorted into the sorting outlet. The existing sorter requires a voltage of 450 V for reliable sorting, whereas the new designs without and with shielding perform the same task at the much lower voltage of 350 V and 200 V, respectively (Figure 6.7).

A lower sorting voltage reduces stray fields and thus simplifies the integration of a sorter with complex microchannel designs. Reduction of the sorting voltage alone does however not imply an increase of the highest achievable sorting frequencies. The limitation is the induced deformation of droplets which will eventually lead to droplet disintegration and limit the sorting frequency. Improved electrode designs will induce much less droplet deformation while still reliably actuating droplets.

At the minimum voltage where reliable sorting is possible, we compare the deformation of droplets between the existing and the (shielded) new design (Figure 6.8). In the reference design, droplets deform significantly, up to a deformation of 22% (where deformation is the deviation of the aspect ratio from unity, $\delta := l_z / l_x - 1$). The droplet deformation is considerably weaker in the new design, with a maximum deformation of just 11%. With the new design, fields are weaker, and thus move droplets gently across the stream lines. To achieve higher sorting frequencies the actuating force and thus voltage needs to be increased. Critical droplet deformations are reached much later for the optimized electrode design so that higher frequencies are possible.

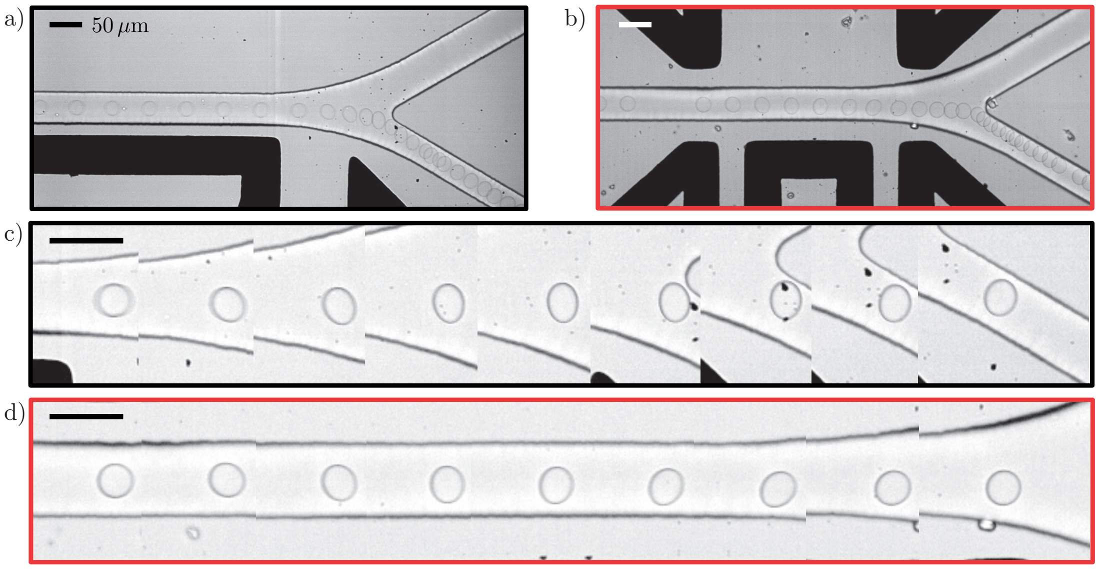

Figure 6.8: Deformation of droplets in *a)* the reference geometry and *b)* the new electrode design with shielding. Electrode voltages were 450 V in the reference geometry and 200 V in the new design, which were the respective thresholds for reliable sorting. *c)* and *d)* show the droplet shape in detail.

6.1.2 Conclusions

We investigate the physical limits of throughput in droplet sorting. With the aid of a 3D boundary-element simulation, we characterize the efficiency of the electrode shape for common sorting devices. Our analysis reveals that 3D effects render long, straight electrodes along the microchannel much more effective than the 2D picture would suggest, and that well-placed ground electrodes increase the sorting efficiency further.

Based on our analysis, we suggest technically feasible designs improving the sorting performance. We demonstrate this superior performance experimentally, by showing that under identical conditions, droplets in the new designs are sorted at much smaller deformations and 50% lower electrode voltages. One consequence is that the sorting rate can be pushed much higher before droplets start to disintegrate. Our analysis suggests that a secondary active electrode can increase the efficiency of a sorting device further, but at the cost of a much higher technical complexity.

The gentle actuation of droplets is particularly relevant for low surface tension applications and systems with large droplets, which are particularly susceptible to breaking up in strong fields. The significant increase in efficiency in both simulation and experiment highlight the power of the rational approach to designing microfluidic systems. Numerically, the efficiency of a particular microfluidic design can be evaluated in seconds, allowing for a fast multidimensional parameter optimization that vastly outperforms traditional trial-and-error methods.

6.1.3 Materials and Methods

Numerical Simulation

The electric field around the electrodes was calculated using a Boundary Element Method (BEM) numerical code written in *C*++, which is based on the Finite-Element framework *deal.ii* [Bangerth et al., 2007]. We solved the Laplace equation for the electrostatic potential φ (with $\vec{E} = -\nabla(\varphi)$),

$$\Delta\varphi \; = \; 0, \tag{6.5}$$

with the potential φ fixed to the voltages V_1 (V_2) and zero on the active sorting electrode(s) and the ground electrode, respectively. For simulations with a finite-size droplet, the boundary condition for the interface was $\varepsilon_c \vec{E}_c = \varepsilon_d \vec{E}_d$. Depending on the mesh complexity, the electrode surfaces were represented by $10^3 - 10^4$ bilinear quadrangular elements. Numerical solution of the discretized boundary integral equation with the GMRES method yielded the field strength on the electrode surfaces, from which we constructed (via integration with appropriate Green's functions) the field and field gradient at discrete points in the volume. The simulation code is parallelized with MPI. Each simulation took 3 minutes on a standard desktop computer. We analyzed 8 existing sorter geometries and performed 800 simulations with different parameter combinations (electrode length, spacing between electrode and channel center, corner radius, voltage of the secondary electrode) for the new electrode designs.

Laboratory Experiments

Poly-(dimethylsiloxane) (PDMS, Sylgard 184) microfluidic devices were fabricated from SU-8 3025 negative photoresists molds as described by Beneyton et al. [2014]. Aquapel (PPG Industries) was used to hydrophobize the channels. Nemesys syringe pumps (Cetoni) were used to control the flows in the microfluidic channels and syringes were connected to the devices with PTFE tubing (ID 0.3 mm, OD 0.76mm; Fisher Scientific). 8 pL w/o droplets were produced (3500 Hz) using a 20x15 μm nozzle dropmaking device in fluorinated oil (Novec7500, 3M) and were stabilized against coalescence by a perfluoropolyether-polyethyleneglycol block-copolymer surfactant (3% w/w) [Beneyton et al., 2016]. Droplets were collected off-chip and stored in a glass vial. Droplets were then co-flown with fluorinated oil in sorting devices with a 50 μm (width) x 24 μm (height) main channel. Sorting efficiency was investigated with constant hydrodynamics conditions ($\mathrm{F_{emulsion}} = 20\ \mu\mathrm{L.h}^{-1}$ and $\mathrm{F_{oil}} = 700\ \mu\mathrm{L.h}^{-1}$) by applying a 20 kHz AC field form 0 to 1 kV (Agilent 33210A function generator connected to a Trek 623B high voltage amplifier). Droplets were imaged at 13 000 fps using a high-speed camera (Phantom v210) and movies were analyzed using the Phantom Camera Control software (PCC 2.1.4).

Acknowledgements

J.-C.B. acknowledges the support from the ERC (FP7/2007-2013/ERC Starting Grant 306385-SofI), from the French state in the frame of the "Investments for the future", Programme IdEx Bordeaux, ANR-10-IDEX-03-02 and of the "Région Aquitaine". We would like to thank Dr. Ouriel Caën and Dr. Valérie Taly (Univ. Paris Descartes) for fruitful discussions.

6.1.4 Appendix

Accuracy of the Approximation Formula for Small Radii

To estimate the deflection force $\vec{F}$ on the droplets, we use relation (6.1) by Pohl [1958], which is valid for spherical droplets whose radius R is small compared to the characteristic length scale of the electric field. Since the actual droplet radius is similar to the size of the electrodes that create the field, Pohl's equation is only an approximation. Here, we investigate its accuracy for large droplets.

We use a single electrode of length $L = 8H$ and a spherical droplet of radius R with a trajectory on the microchannel centerline. We calculate the electric field around the electrodes in the presence of the droplet (Figure 6.9), using a mesh of approximately 2,200 degrees of freedom. From the field at the droplet surface, we determine the cross-stream deflection force F_R along the droplet path, which we compare to the approximated force F_0 from equation (6.1). The approximation error is quantified by the integrated force difference along the droplet path,

$$\varepsilon_R := \frac{\langle |F_R - F_0| \rangle}{\langle F_R \rangle}, \tag{6.6}$$

where $\langle ... \rangle$ denotes the spatial average along the droplet path.

We find that the approximation accurately describes the force for small R, but underestimates the force for larger R, as shown in Figure 6.9b,c. The approximation error ε_R is on the order of few percent and increases for $R > 0.1H$. At $R = 0.5H$, when the droplet diameter equals the channel height, the relative error is $\varepsilon_R = 4.6\%$: For typical droplet sizes and channel layouts, the approximation conservatively underestimates the sorting efficiency, with a relative error on the order of 5%.

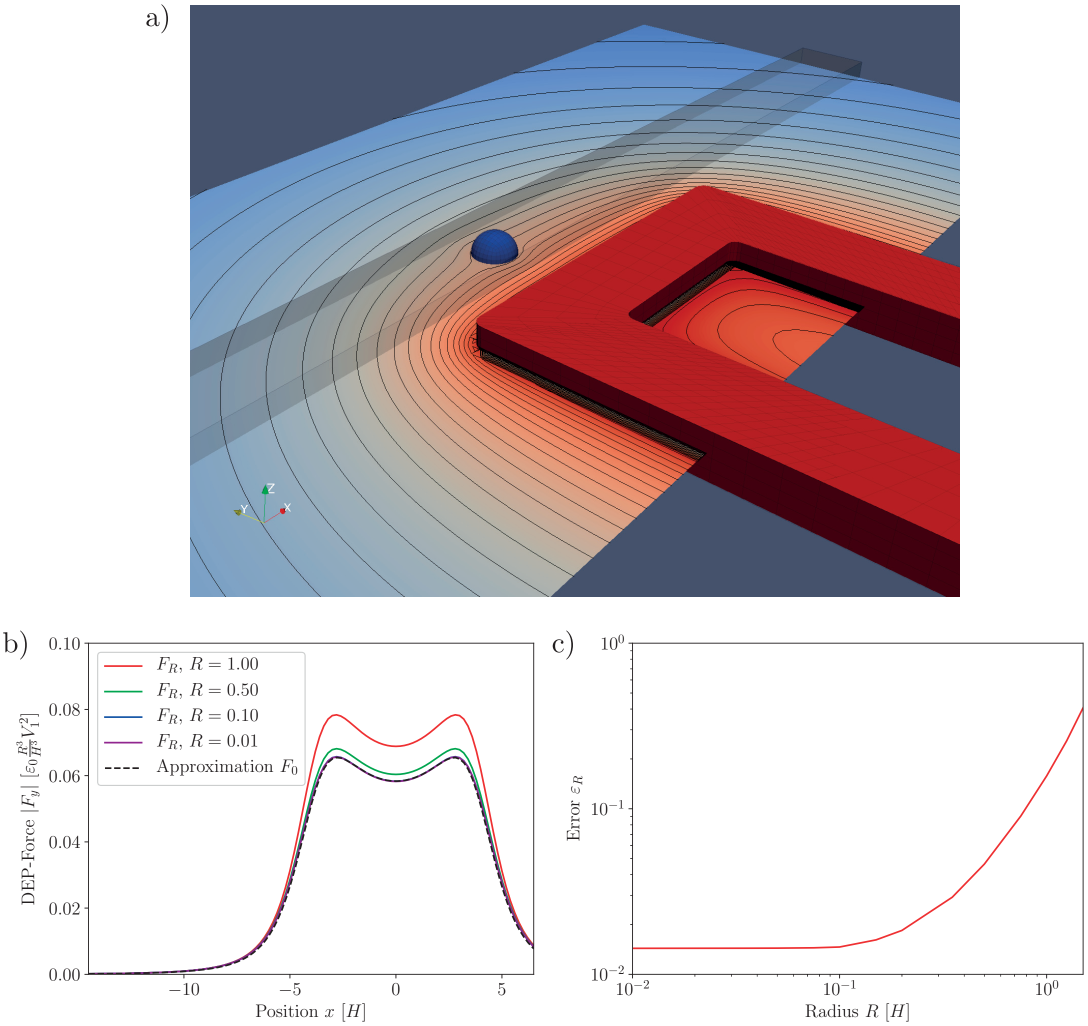

Figure 6.9: Deflection force on a droplet with finite radius. *a)* Droplet ($R = 0.5H$) in a microchannel next to an active electrode. Equipotential contour lines around the sorting electrode show the distortion of the field due to the finite-size droplet. *b)* Deflection force of the approximation formula, and the full 3D simulation, for different droplet radii R. *c)* Relative error of the approximation formula against droplet radius R. The error ε_R for $R \to 0$ does not converge to zero due to the limited numerical precision of the simulation.

6.2 High Throughput Multiplexed Fluorescence Activated Droplet Sorting

In Caen et al. [2018], we propose a multiplexed dielectrophoretic droplet sorter for applications where more than just two distinct species of droplets need to be sorted. In a symmetric sorting chamber with five outlet channels, we use two active electrodes to actuate droplets. The electrode voltage and length of the pulse select the outlet channel. The variation of the electrode voltage allows us to operate with a higher number of outlet channels per electrode, compared to other approaches such as the design by Frenzel and Merten [2017], which sorts multiple droplet species by concatenating a large number of two-way sorters in quick succession (with two active electrodes per two-way sorter), or the three-way sorter by Girault et al. [2017] with two active electrodes for three outlet channels.

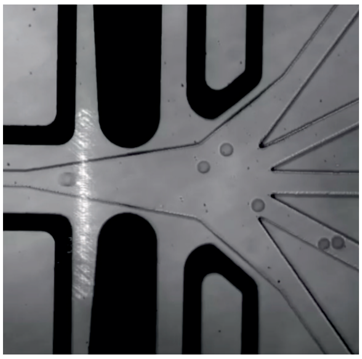

Figure 6.10: Multiplexed sorting geometry in the experiment. – Image by Ouriel Caën 2017, used with permission.

We accompany the design of the experimental system by numerical simulations with the coupled electro/Stokes solver. The droplet trajectories that we find numerically match the experimental observations (Figure 6.11). To operate the sorting geometry with droplets of different size, we estimate how the droplet voltages need to be scaled to allow reliable sorting. If the droplet radius R is not much smaller than the channel height H, work by Keh and Chen [2001] suggests that the drag force F_{drag} scales as

$$F_{\text{drag}} \propto R^2 U_{\text{drift}}, \tag{6.7}$$

where U_{drift} is the drift velocity of the droplet relative to the viscous background flow. The drag on the droplet compensates the dielectrophoretic actuation force F_{DEP}, which by eq. (6.1) [Pohl, 1958] scales with

$$F_{\text{DEP}} \propto R^3 V_{pp}^2, \tag{6.8}$$

with V_{pp} the peak-to-peak voltage of the sorting electrodes that create the electric field. Consequently, the drift velocity $U_{\text{drift}} \propto RV_{pp}^2$ is constant if the electrode voltage is chosen as $V_{pp} \propto 1/\sqrt{R}$. The scaling is supported by our numerical simulations (Figure 6.12). Experimentally, choosing an appropriate electrode voltage is important in our sorter design, as the strength of the electric field selects the outlet channel.

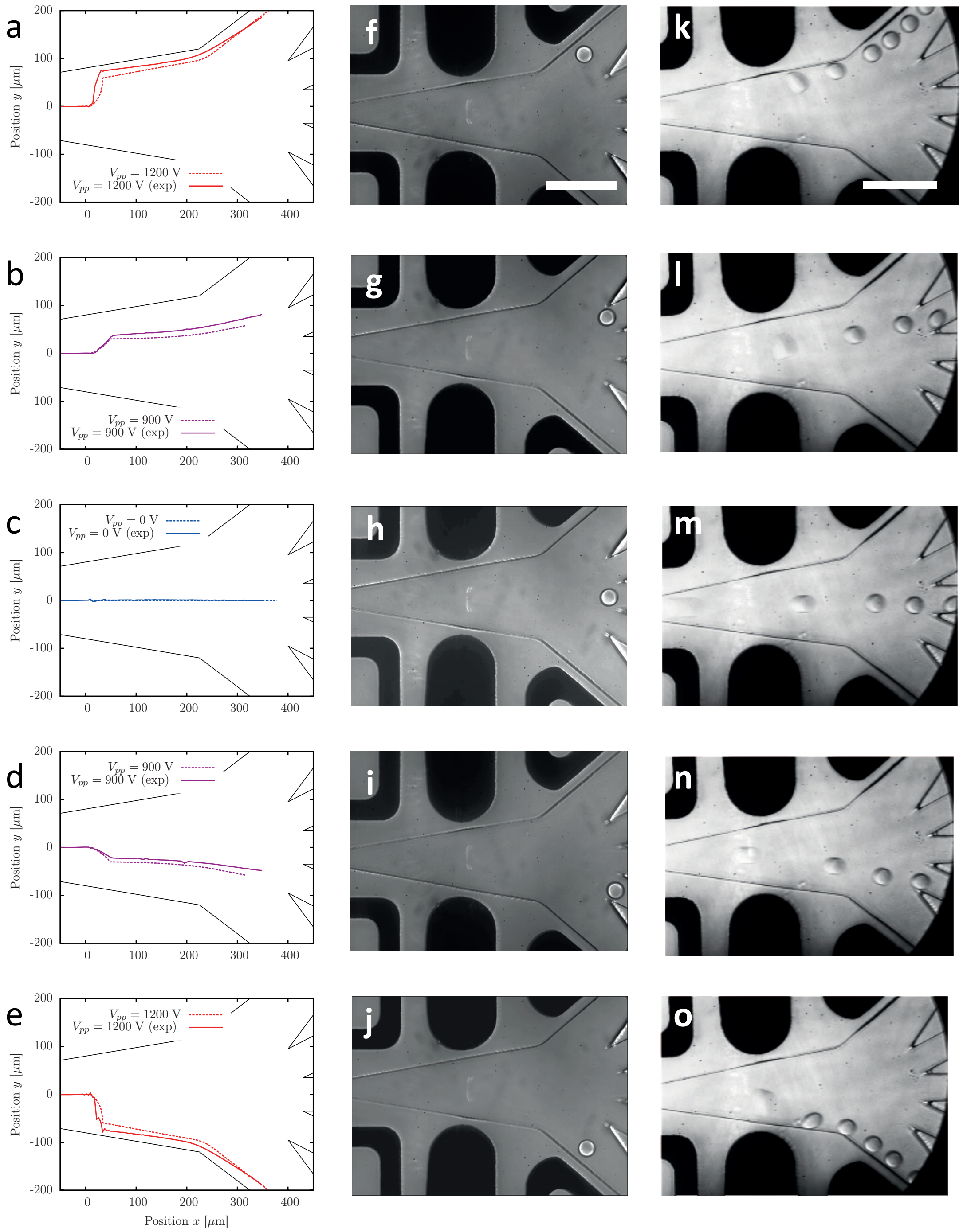

Figure 6.11: Numerically predicted and experimentally observed droplet trajectories in the multiplexed sorting geometry. The scale bar is 200 μm. – Figure reproduced from Caen et al. [2018] with permission from the other authors.

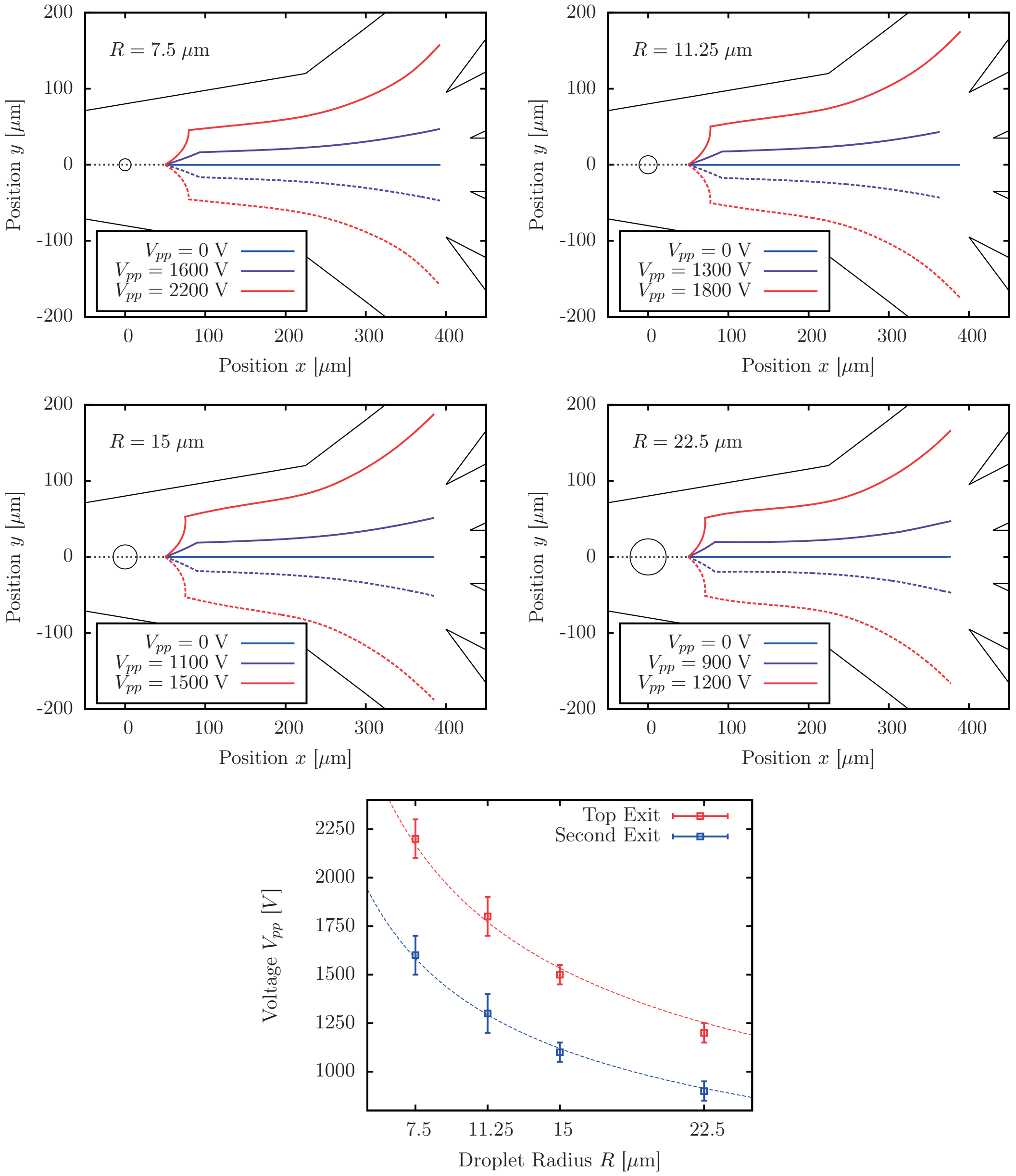

Figure 6.12: Electrode voltages for sorting of droplets with different characteristic radius R in the multiplexed sorting geometry. – Figure reproduced from Caen et al. [2018] with permission from the other authors.

6.3 Summary

Fast actuation of droplets with electric fields requires high field strengths, which can cause droplet disintegration. To achieve high throughput in dielectrophoretic droplet sorting, we apply a gentle force for a longer amount of time, which achieves the same droplet displacement relative to the background flow but reduces the short-term stress on the droplet. The required gradient in the electric field is created with long, straight electrodes. By combining the straight electrodes with shielding, we can operate a droplet sorting device at lower voltages and causes less droplet deformation (Section 6.1).

For sorting a droplet population of five different types, we use a multiplexed droplet sorter (Section 6.2), which is compact and requires just two active electrodes. In this design, larger droplets require a lower sorting voltage . Since large droplets are also more susceptible to breakup in strong fields (see Section 6.1), fast and efficient sorting works best if the droplet size matches the height of the channel geometry.

7 Conclusions and Outlook

Contents

7.1 3D Boundary Element Simulation of Droplets 119

7.2 Droplet Dynamics in Microchannels 122

7.3 Final Remarks 124

This thesis studies the dynamics of droplets in microfluidic applications. It comprises two parts: The design and implementation of a 3D boundary element scheme to simulate droplet motion in complex microchannel geometries, and a study on droplet dynamics and interaction in two specific flow situations. For each of the parts, we summarize our findings, and give an outlook for future research.

7.1 3D Boundary Element Simulation of Droplets

The design and implementation of the 3D boundary element scheme is reported in Part I. While the general concept for simulating multi-phase flow and electric fields with the boundary element method is well established, there exists no publically available framework to solve the coupled system in arbitrary geometries. We therefore implemented the boundary integral equations in C++, building upon the flexible finite-element library deal.ii.

Solving the boundary integral equations in the complex geometry poses several challenges, which we addressed in our implementation. First, the discretized mesh for the complex microchannel geometries must be created. For this, we implemented automatic mesh generation routines for a number of different flow configurations, including a description for microchannel shapes via Bezier curves. Second, as the boundary element algorithm scales with the square of the number of degrees of freedom, we developed a surface representation that describes smoothly curved surfaces with a small number of mesh vertices (where degrees of freedom are defined), which also allows for a fast computation of the surface curvature. A local mesh refinement based on geometrical criteria increases resolution where large variations in the surface velocity or stress fields are expected. Special quadrature rules and singularity subtraction techniques mitigate the errors in numerical quadrature when evaluating boundary integrals that exist only in a principal-value sense. Forward integration in time uses an explicit time stepping scheme, and respects the one-way coupling between electric and Stokes solver.

In an extensive validation phase, we found that our simulation reproduces known results from simulation and theory, outperforming other simulation approaches in some of the applications. The boundary element method has been parallelized, and scales well with the number of processors.

Outlook

Numerical Approximation

While the validation confirmed the numerical code to be correct, there are numerical errors that depend on the mesh resolution, the type of finite-element basis functions, and numerical quadrature. From Section 4.2, we see that bilinear interpolation dominates the error for typical stress and velocity fields on the boundary. Even for a simple flow in a duct, the convergence order is only linear in the number of degrees of freedom, and relative errors on the order of 10^{-3} for $N = 10^4$ degrees of freedom are common. Extending the simulation to a second-order (quadratic) scheme for the boundary fields is possible in the framework of the current implementation, and increases the convergence order of the solution. The original scheme avoids this higher order representation to reduce the number of degrees of freedom (especially since only the velocities on the cell's corner vertices are needed to advance in time), but quadratic elements are a good compromise between number of degrees of freedom and accuracy of the description, given that the Stokes equations are second-order in space.

In a second-order scheme, quadratic interpolation can also be used for the mesh surface, with the intermediate vertices between the cell corners adjusted to minimize curvature jumps on the edge. This simplifies the description of surface shape, but might have lower accuracy than our custom implementation of a second-order paraboloid fitting.

Scaling of Runtime with System Size

When discussing the advantages of the boundary-element scheme, it is often argued that the method is more efficient than comparable finite-element methods, because a mesh of resolution Δx is described with $N \propto 1/(\Delta x)^2$ degrees of freedom when describing the 2D boundary in the BEM scheme, whereas the FEM scheme represents the 3D volume and thus requires $N \propto 1/(\Delta x)^3$ degrees of freedom. While it is true that the BEM scheme describes the surface fields with better accuracy, we want to explicitly point out here that for solving the linear system of the discretized boundary integral equations, the BEM scheme is at a disadvantage, because there is global coupling between the degrees of freedom, and the work for setting up the linear system is of order $\mathcal{O}(1/(\Delta x)^4)$. In the finite element method, coupling is local and the linear system sparse. Nevertheless, the boundary element method is suitable for complex geometries: Setting up and solving the linear system is trivial to parallelize, and only the degrees of freedom (which are fewer than in the finite element method) need to be shared between the nodes. As computer systems become more and more parallel, their performance is increasingly limited by data communication, rather than pure computing effort. This development favors the boundary element method even in large or highly resolved systems.

Time Stepping

An increase in mesh resolution or representation order will have to be accompanied by more elaborate time stepping schemes. In the explicit Euler scheme that we currently employ, the time step has to be small in order to avoid instabilities in the interface shape. While implicit schemes will be difficult to combine with the boundary-element approach, explicit higher-order time integration schemes like the second-order Runge-Kutta scheme or the Adams-Bashforth scheme are comparatively easy to implement and increase stability, if the difficulties we met when combining them with our mesh stabilization and refinement algorithms are overcome. In addition, the formation of small-scale spatial oscillations in the shape of the free interface can be suppressed with interface stabilization techniques (such as the one presented by Nagel and Gallaire [2015]). Here, the change in Young-Laplace stress on the interface during a time step is anticipated, and the local surface stress adjusted accordingly.

Topological Transitions

Changes in mesh topology due to droplet coalescence or break-up are computationally expensive in our simulation, as the hierarchical quadrilateral mesh structure requires a complete re-meshing at every topological transition. Triangular meshes are more flexible in this respect. They are easier to refine and coarsen locally, and can be broken up and reconnected without consequences for the global structure (as for example shown by Cristini et al. [2001]). However, quadrilateral meshes provide an easier mapping and integration for the reference element, and thus better approximation quality for a given number of degrees of freedom. For simulations without topological transitions, we prefer quadrilateral meshes.

Handling of Narrow Gaps

In narrow gaps, either between two droplet interfaces or between a droplet and the microchannel wall, flow is typically very regular, and can be described by a 2D lubrication approximation (as in Bretherton [1961]; Goldman et al. [1967]). If an appropriate matching to the bulk BEM solution at the boundaries of the thin-film region can be found, simulating lubrication flow could be an alternative to solving the Stokes equations in narrow gaps, where the close distance between boundaries leads to strong hydrodynamic interaction and thus nearly-singular integrals over the Greens' functions.

7.2 Droplet Dynamics in Microchannels

In Part II of this thesis, we investigated droplet interaction in narrow constrictions and droplet sorting by dielectrophoresis. We combined results from the numerical simulation with analytic calculations and experiments.

From experiments on the reinjection of concentrated emulsions into narrow channels, we found that the breakup of droplets is mostly controlled by two-droplet interaction at the constriction. With our numerical tools, we could then study two-droplet interaction in a junction. The physical mechanism behind droplet breakup turned out to be an autonomous pinch-off process similar to the Rayleigh-Plateau instability, driven by a pressure difference between the two droplets caused by differences in the front radius. Careful comparison between simulation and experiments revealed a quantitative difference in the critical Capillary numbers for droplet breakup. From an analysis of the time scales and relative strengths of different physical processes in the system, we determined that surfactants on the droplet interface would not be in equilibrium during the fast process of droplet deformation and breakup, so that Marangoni stresses would inhibit droplet deformation and breakup in the experiment.

For dielectric droplet sorting, we derived a quantitative measure of the efficiency of a droplet sorting device. Analyzing existing sorter designs, we isolated the features that would lead to gentle sorting at low voltages, avoiding strong droplet deformations and breakup. Experiments show the superior performance of a sorting design with long, straight electrodes and shielding. In a study on multiplexed droplet sorting, we used the full capabilities of our numerical code to simulate droplet motion in electric fields. We find quantitative agreement with the experiments, and contribute results on the dependence of the electrode voltage on the droplet size.

Outlook

Droplet Breakup in Concentrated Emulsions

At lot remains to be understood about collective effects such as local jamming, which appears to affect the breakup of densely packed droplets in microchannel constrictions. While some predictions for the scaling and reliability of droplet reinjection exist (notably the study by Gai et al. [2016a]), the physical basis of the scaling is not addressed. Here, the analytical model that we derived from two-droplet interaction could be extended to include the effects of different droplet sizes, opening angles of the constriction, or even the influence of a third and more droplets.

Effects of Marangoni Stresses

The effect of surfactants on droplet dynamics and breakup is a current field of study, but simple models could be implemented in the numerical code. Besides a comparison with the experimental data for two-droplet interaction, one observation that a surfactant model for complex droplet interaction might help explain is the complex internal flow pattern inside droplets in densely packed emulsions. Leong et al. [2016] measure an internal flow in a packed emulsion, which is qualitatively different from flows we find in simulations that assume no Marangoni stresses. Marangoni stresses oppose any surface stretching and thus explain the observed flow (Figure 7.1).

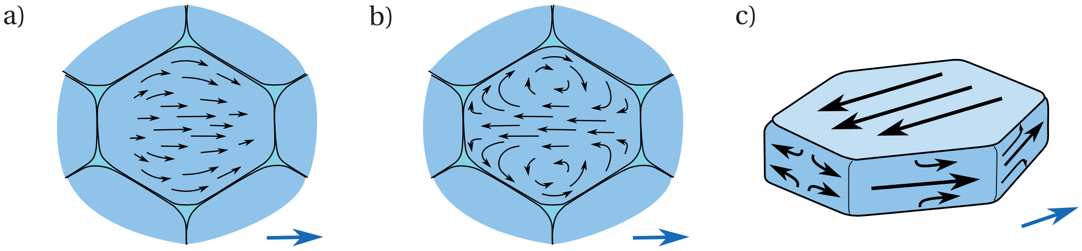

Figure 7.1: Internal flow in closely packed droplets. Flow vectors in the inertial frame of the droplet. Blue arrows indicate the direction of downstream motion. *a)* Sketch of the midplane flow that we estimate from preliminary simulations for a compressible interface. Backward flow on the top and bottom boundaries (not shown) is compensated by a forward flow in the center. *b)* Flow pattern observed in experiments by Leong et al. [2016]. The flow in the center is backwards. *c)* Flow pattern of an incompressible interface that drives the flow as observed in the experiments. Backwards advection of the top and bottom droplet interface relative to the mean droplet motion is compensated by a forward motion on the sides, which explains the internal circulation that experiments show.

Droplet Sorting

Our study on droplet sorting is focused on the electrode designs, while the geometry of microchannels has not been addressed. Experiments show that strong shear, in particular at the dividing channel wall at the bifurcation, can lead to droplet disintegration at high flow rates [Sciambi and Abate, 2015]. Combining a microchannel design that reduces shear on droplets with the here presented optimized electrode layout that minimizes droplet deformation due to dielectric forces would be the next step in high-throughput sorting applications. By varying the channel cross-section, the advection speed of droplets can be modified, so that droplets spend more time in the zone of high field strength. If droplets are actuated strong enough to avoid collisions with the channel bifurcation, shear forces are reduced.

Understanding of Droplet Pinch-Off

In addition to these application-related points, some open questions remain for a more fundamental understanding of droplet behavior. In particular, droplet pinch-off is an interesting process that merits closer study. Eggers [1997] discusses the self-similar pinch-off scaling of a liquid thread in a gas of negligible viscosity; but a viscous outer fluid will likely change the scaling qualitatively. The study of droplet break-up in constrictions brought up the question whether the equilibrium shape of two liquid threads (or extended droplets) in a rectangular channel could be derived from simple geometrical considerations, and how the breakup transition from threads to droplets might progress in time (Figure 7.2).

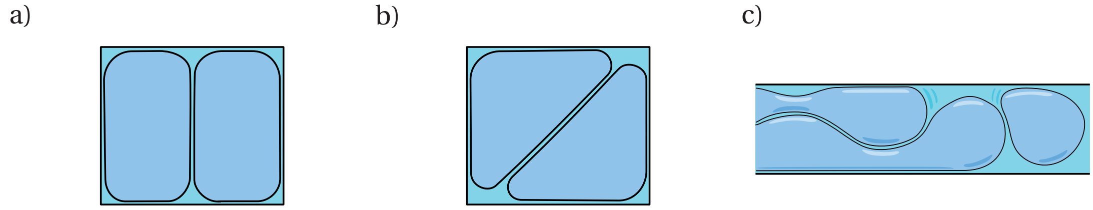

Figure 7.2: Breakup of liquid threads in a long, straight channel. *a), b)* Configurations of long droplets in a rectangular channel, cross-section view. Different stable droplet configurations could exist depending on the channel aspect ratio and degree of confinement. *c)* Depending on the geometry, small droplets might have lower surface energy than two long liquid threads lying side by side. A breakup cascade into small droplets would then be possible.

7.3 Final Remarks

With the ever increasing availability of computational power, complex flow problems can be studied in unprecedented detail. We have shown how numerical tools, combined with experimental observations, deepen our understanding of highly nonlinear physical phenomena. Of course, confronting the theoretical models with physical reality carries the risk of discovering that rotationally symmetric droplets, flows without inertia or surfactant-free interfaces do not exist in nature. But equipped with the tools to compare model and reality in practically relevant flows, we are ready to test assumptions, uncover effects that have previously been overlooked or ignored, and refine the models that describe the flow physics.

A Jacobian, Normal and Curvature of the Smooth Surface Representation

In Section 3.4, we present a smooth representation of the surface on droplet interfaces. The representation is defined by the mapping (3.28) from a reference element $(a,b) \in [0,1] \times [0,1]$ onto a cell of the boundary mesh. Here, we note the expressions to calculate the Jacobian of this mapping, the local normal of the surface, and the curvature κ that drives the Young-Laplace stress (Section 2.3.1).

A.1 Jacobian and Normal Vector

Both the Jacobian of the mapping and the unit normal vector of the surface are calculated from the derivatives of $\boldsymbol{x}$ with respect to the reference cell coordinates (a,b). For the paraboloid $\boldsymbol{x}_i(a,b)$ of corner vertex $\boldsymbol{v}_i$, the derivatives are

$$
\begin{aligned}
\frac{\partial \boldsymbol{x}_i}{\partial a} &= (\partial_a x_i) \cdot \hat{\boldsymbol{e}}_{x,i} + (\partial_a y_i) \cdot \hat{\boldsymbol{e}}_{y,i} + \left[2\alpha_i x_i (\partial_a x_i) + 2\beta_i y_i (\partial_a y_i) + \gamma_i (x_i (\partial_a y_i) + (\partial_a x_i) y_i)\right] \cdot \hat{\boldsymbol{n}}_i \\
\frac{\partial \boldsymbol{x}_i}{\partial b} &= (\partial_b x_i) \cdot \hat{\boldsymbol{e}}_{x,i} + (\partial_b y_i) \cdot \hat{\boldsymbol{e}}_{y,i} + \left[2\alpha_i x_i (\partial_b x_i) + 2\beta_i y_i (\partial_b y_i) + \gamma_i (x_i (\partial_b y_i) + (\partial_b x_i) y_i)\right] \cdot \hat{\boldsymbol{n}}_i
\end{aligned}
$$

with the derivatives of the bilinear interpolation $\boldsymbol{x}_b(a,b)$ given by

$$
\begin{aligned}
\partial_a \boldsymbol{x}_b &= (1-b)(\boldsymbol{v}_1 - \boldsymbol{v}_0) + b(\boldsymbol{v}_3 - \boldsymbol{v}_2) & \qquad \partial_b \boldsymbol{x}_b &= (1-a)(\boldsymbol{v}_2 - \boldsymbol{v}_0) + a(\boldsymbol{v}_3 - \boldsymbol{v}_1) \\
\partial_a x_i &= [\partial_a \boldsymbol{x}_b] \cdot \hat{\boldsymbol{e}}_{x,i} & \partial_b x_i &= [\partial_b \boldsymbol{x}_b] \cdot \hat{\boldsymbol{e}}_{x,i} \\
\partial_a y_i &= [\partial_a \boldsymbol{x}_b] \cdot \hat{\boldsymbol{e}}_{y,i} & \partial_b y_i &= [\partial_b \boldsymbol{x}_b] \cdot \hat{\boldsymbol{e}}_{y,i}.
\end{aligned}
$$

For the interpolation (3.28), we then get the tangent vectors at (a,b),

$$
\begin{aligned}
\boldsymbol{t}_a := \frac{\partial \boldsymbol{x}}{\partial a} &= \psi_0'(a)\psi_0(b)\boldsymbol{x}_0 + \psi_1'(a)\psi_0(b)\boldsymbol{x}_1 + \psi_0'(a)\psi_1(b)\boldsymbol{x}_2 + \psi_1'(a)\psi_1(b)\boldsymbol{x}_3 \\
&+ \psi_0(a)\psi_0(b)\frac{\partial \boldsymbol{x}_0}{\partial a} + \psi_1(a)\psi_0(b)\frac{\partial \boldsymbol{x}_1}{\partial a} + \psi_0(a)\psi_1(b)\frac{\partial \boldsymbol{x}_2}{\partial a} + \psi_1(a)\psi_1(b)\frac{\partial \boldsymbol{x}_3}{\partial a},
\end{aligned}
$$

$$
\begin{aligned}
\boldsymbol{t}_b := \frac{\partial \boldsymbol{x}}{\partial b} &= \psi_0(a)\psi_0'(b)\boldsymbol{x}_0 + \psi_1(a)\psi_0'(b)\boldsymbol{x}_1 + \psi_0(a)\psi_1'(b)\boldsymbol{x}_2 + \psi_1(a)\psi_1'(b)\boldsymbol{x}_3 \\
&+ \psi_0(a)\psi_0(b)\frac{\partial \boldsymbol{x}_0}{\partial b} + \psi_1(a)\psi_0(b)\frac{\partial \boldsymbol{x}_1}{\partial b} + \psi_0(a)\psi_1(b)\frac{\partial \boldsymbol{x}_2}{\partial b} + \psi_1(a)\psi_1(b)\frac{\partial \boldsymbol{x}_3}{\partial b}.
\end{aligned}
$$

From the tangent vectors we determine the surface normal vector [Bronstein et al., 2008, p. 267]

$$
\boldsymbol{N} = \frac{\boldsymbol{t}_a \times \boldsymbol{t}_b}{|\boldsymbol{t}_a \times \boldsymbol{t}_b|}, \tag{A.1}
$$

and the Jacobian of the mapping from the reference cell

$$
J = |\boldsymbol{t}_a \times \boldsymbol{t}_b|. \tag{A.2}
$$

A.2 Curvature

To determine the mean curvature κ at (a,b), we calculate the second derivatives of the paraboloid $\boldsymbol{x}_i$ as

$$
\begin{aligned}
\frac{\partial^2 \boldsymbol{x}_i}{\partial a^2} &= [2\alpha_i(\partial_a x_i)^2 + 2\beta_i(\partial_a y_i)^2 + 2\gamma_i(\partial_a x_i)(\partial_a y_i)] \cdot \hat{\boldsymbol{n}}_i, \\
\frac{\partial^2 \boldsymbol{x}_i}{\partial b^2} &= [2\alpha_i(\partial_b x_i)^2 + 2\beta_i(\partial_b y_i)^2 + 2\gamma_i(\partial_b x_i)(\partial_b y_i)] \cdot \hat{\boldsymbol{n}}_i, \\
\frac{\partial^2 \boldsymbol{x}_i}{\partial a \partial b} &= (\partial_{ab} x_i) \cdot \hat{\boldsymbol{e}}_{x,i} + (\partial_{ab} y_i) \cdot \hat{\boldsymbol{e}}_{y,i} \\
&+ [2\alpha_i(\partial_a x_i)(\partial_b x_i) + 2\beta_i(\partial_a y_i)(\partial_b y_i) + \gamma_i((\partial_b x_i)(\partial_a y_i) + (\partial_a x_i)(\partial_b y_i))] \cdot \hat{\boldsymbol{n}}_i \\
&+ [2\alpha_i x_i(\partial_{ab} x_i) + 2\beta_i y_i(\partial_{ab} y_i) + \gamma_i(x_i(\partial_{ab} y_i) + (\partial_{ab} x_i) y_i)] \cdot \hat{\boldsymbol{n}}_i,
\end{aligned}
$$

using first derivatives of the bilinear interpolation as in Section A.1 and second derivatives

$$
\begin{aligned}
\partial_{ab} \boldsymbol{x}_b &= (\boldsymbol{v}_0 + \boldsymbol{v}_3) - (\boldsymbol{v}_1 + \boldsymbol{v}_2), \\
\partial_{ab} x_i &= [\partial_{ab} \boldsymbol{x}_b] \cdot \hat{\boldsymbol{e}}_{x,i}, \\
\partial_{ab} y_i &= [\partial_{ab} \boldsymbol{x}_b] \cdot \hat{\boldsymbol{e}}_{y,i}.
\end{aligned}
$$

Together with the first derivatives noted in Section A.1, the second derivatives of $\boldsymbol{x}_i$ are needed to calculate derivatives of the mapping (3.28),

$$
\begin{aligned}
\frac{\partial^2 \boldsymbol{x}}{\partial a^2} &= \psi_0''(a)\psi_0(b)\boldsymbol{x}_0 + \psi_1''(a)\psi_0(b)\boldsymbol{x}_1 + \psi_0''(a)\psi_1(b)\boldsymbol{x}_2 + \psi_1''(a)\psi_1(b)\boldsymbol{x}_3 \\
&+ 2\psi_0'(a)\psi_0(b)\frac{\partial \boldsymbol{x}_0}{\partial a} + 2\psi_1'(a)\psi_0(b)\frac{\partial \boldsymbol{x}_1}{\partial a} + 2\psi_0'(a)\psi_1(b)\frac{\partial \boldsymbol{x}_2}{\partial a} + 2\psi_1'(a)\psi_1(b)\frac{\partial \boldsymbol{x}_3}{\partial a} \\
&+ \psi_0(a)\psi_0(b)\frac{\partial^2 \boldsymbol{x}_0}{\partial a^2} + \psi_1(a)\psi_0(b)\frac{\partial^2 \boldsymbol{x}_1}{\partial a^2} + \psi_0(a)\psi_1(b)\frac{\partial^2 \boldsymbol{x}_2}{\partial a^2} + \psi_1(a)\psi_1(b)\frac{\partial^2 \boldsymbol{x}_3}{\partial a^2},
\end{aligned}
$$

$$\begin{aligned}
\frac{\partial^2 \boldsymbol{x}}{\partial b^2} =\ & \psi_0(a)\psi_0''(b)\boldsymbol{x}_0 + \psi_1(a)\psi_0''(b)\boldsymbol{x}_1 + \psi_0(a)\psi_1''(b)\boldsymbol{x}_2 + \psi_1(a)\psi_1''(b)\boldsymbol{x}_3 \\
& + 2\psi_0'(a)\psi_0(b)\frac{\partial \boldsymbol{x}_0}{\partial b} + 2\psi_1'(a)\psi_0(b)\frac{\partial \boldsymbol{x}_1}{\partial b} + 2\psi_0'(a)\psi_1(b)\frac{\partial \boldsymbol{x}_2}{\partial b} + 2\psi_1'(a)\psi_1(b)\frac{\partial \boldsymbol{x}_3}{\partial b} \\
& + \psi_0(a)\psi_0(b)\frac{\partial^2 \boldsymbol{x}_0}{\partial b^2} + \psi_1(a)\psi_0(b)\frac{\partial^2 \boldsymbol{x}_1}{\partial b^2} + \psi_0(a)\psi_1(b)\frac{\partial^2 \boldsymbol{x}_2}{\partial b^2} + \psi_1(a)\psi_1(b)\frac{\partial^2 \boldsymbol{x}_3}{\partial b^2},
\end{aligned}$$

$$\begin{aligned}
\frac{\partial^2 \boldsymbol{x}}{\partial a \partial b} =\ & \psi_0'(a)\psi_0'(b)\boldsymbol{x}_0 + \psi_1'(a)\psi_0'(b)\boldsymbol{x}_1 + \psi_0'(a)\psi_1'(b)\boldsymbol{x}_2 + \psi_1'(a)\psi_1'(b)\boldsymbol{x}_3 \\
& + \psi_0'(a)\psi_0(b)\frac{\partial \boldsymbol{x}_0}{\partial b} + \psi_1'(a)\psi_0(b)\frac{\partial \boldsymbol{x}_1}{\partial b} + \psi_0'(a)\psi_1(b)\frac{\partial \boldsymbol{x}_2}{\partial b} + \psi_1'(a)\psi_1(b)\frac{\partial \boldsymbol{x}_3}{\partial b} \\
& + \psi_0(a)\psi_0'(b)\frac{\partial \boldsymbol{x}_0}{\partial a} + \psi_1(a)\psi_0'(b)\frac{\partial \boldsymbol{x}_1}{\partial a} + \psi_0(a)\psi_1'(b)\frac{\partial \boldsymbol{x}_2}{\partial a} + \psi_1(a)\psi_1'(b)\frac{\partial \boldsymbol{x}_3}{\partial a} \\
& + \psi_0(a)\psi_0(b)\frac{\partial^2 \boldsymbol{x}_0}{\partial a \partial b} + \psi_1(a)\psi_0(b)\frac{\partial^2 \boldsymbol{x}_1}{\partial a \partial b} + \psi_0(a)\psi_1(b)\frac{\partial^2 \boldsymbol{x}_2}{\partial a \partial b} + \psi_1(a)\psi_1(b)\frac{\partial^2 \boldsymbol{x}_3}{\partial a \partial b}.
\end{aligned}$$

We now define the coefficients of the first and second fundamental form [Bronstein et al., 2008, p. 270f],

$$\begin{aligned}
E &:= \boldsymbol{t}_a \cdot \boldsymbol{t}_a & F &:= \boldsymbol{t}_a \cdot \boldsymbol{t}_b & G &:= \boldsymbol{t}_b \cdot \boldsymbol{t}_b \\
L &:= \frac{\partial^2 \boldsymbol{x}}{\partial a^2} \cdot \boldsymbol{n} & M &:= \frac{\partial^2 \boldsymbol{x}}{\partial a \partial b} \cdot \boldsymbol{n} & N &:= \frac{\partial^2 \boldsymbol{x}}{\partial b^2} \cdot \boldsymbol{n},
\end{aligned}$$

and write the mean curvature κ as

$$\kappa = \frac{EN - 2FM + GL}{2(EG - F^2)}. \tag{A.3}$$

Bibliography

Jeremy J Agresti, Eugene Antipov, Adam R Abate, Keunho Ahn, Amy C Rowat, Jean-Christophe Baret, Manuel Marquez, Alexander M Klibanov, Andrew D Griffiths, and David A Weitz. Ultrahigh-throughput screening in drop-based microfluidics for directed evolution. *Proc. Natl. Acad. Sci.*, 107:4004–4009, 2010.

Keunho Ahn, Jeremy J Agresti, Henry Chong, Manuel Marquez, and David A Weitz. Electrocoalescence of drops synchronized by size-dependent flow in microfluidic channels. *Appl. Phys. Lett.*, 88(26):264105, 2006a.

Keunho Ahn, Charles Kerbage, Tom P Hunt, R M Westervelt, Darren R Link, and David A Weitz. Dielectrophoretic manipulation of drops for high-speed microfluidic sorting devices. *Appl. Phys. Lett.*, 88(2):024104, 2006b.

Shelley L Anna, Nathalie Bontoux, and Howard A Stone. Formation of dispersions using "flow focusing" in microchannels. *Appl. Phys. Lett.*, 82(3):364–366, 2003.

Wolfgang Bangerth, Ralf Hartmann, and Guido Kanschat. deal.II—A general-purpose object-oriented finite element library. *ACM Trans. Math. Softw.*, 33(4):24–es, 2007.

Wolfgang Bangerth, Timo Heister, Luca Heltai, Guido Kanschat, Martin Kronbichler, Matthias Maier, and Bruno Turcksin. The deal. II Library, Version 8.3. *Arch. Numer. Softw.*, 4(100): 1–11, 2016.

Jean-Christophe Baret, Felix Kleinschmidt, Abdeslam El Harrak, and Andrew D Griffiths. Kinetic aspects of emulsion stabilization by surfactants: A microfluidic analysis. *Langmuir*, 25(11):6088–6093, 2009a.

Jean-Christophe Baret, Oliver J Miller, Valerie Taly, Michaël Ryckelynck, Abdeslam El-Harrak, Lucas Frenz, Christian Rick, Michael L Samuels, J Brian Hutchison, Jeremy J Agresti, Darren R Link, David A Weitz, and Andrew D Griffiths. Fluorescence-activated droplet sorting (FADS): efficient microfluidic cell sorting based on enzymatic activity. *Lab Chip*, 9(13):1850–8, 2009b.

D Barthès-Biesel and A Acrivos. Deformation and burst of a liquid droplet freely suspended in a linear shear field. *J. Fluid Mech.*, 61(1):1–22, 1973.

George Keith Batchelor. *An Introduction to Fluid Mechanics*. Cambridge University Press, New York, 1967. ISBN 0-521-66396-2.

Thomas Beneyton, Faith Coldren, Jean-Christophe Baret, Andrew D Griffiths, and Valérie Taly. CotA laccase: high-throughput manipulation and analysis of recombinant enzyme libraries expressed in E. coli using droplet-based microfluidics. *Analyst*, 139(13):3314–3323, 2014.

Thomas Beneyton, I Putu Mahendra Wijaya, Prexilia Postros, Majdi Najah, Pascal Leblond, Angélique Couvent, Estelle Mayot, Andrew D Griffiths, and Antoine Drevelle. High-throughput screening of filamentous fungi using nanoliter-range droplet-based microfluidics. *Sci. Rep.*, 6:27223, 2016.

B J Bentley and L G Leal. An experimental investigation of drop deformation and breakup in steady, two-dimensional linear flows. *J. Fluid Mech.*, 167:241, 1986.

Evangelos Bertakis, Sven Groß, Jörg Grande, Oliver Fortmeier, Arnold Reusken, and Andreas Pfennig. Validated simulation of droplet sedimentation with finite-element and level-set methods. *Chem. Eng. Sci.*, 65(6):2037–2051, 2010.

Jérôme Bibette, F Leal Calderon, and P Poulin. Emulsions: basic principles. *Reports Prog. Phys.*, 62(6):969–1033, 1999.

Francis Patton Bretherton. The motion of long bubbles in tubes. *J. Fluid Mech.*, 10(02):166, 1961.

I N Bronstein, K A Semendjajew, G Musiol, and H Mühlig. *Taschenbuch der Mathematik*. Verlag Harri Deutsch, Frankfurt, 7th edition, 2008. ISBN 978-3-8171-2007-9.

Quentin Brosseau, Jérémy Vrignon, and Jean-Christophe Baret. Microfluidic Dynamic Interfacial Tensiometry (μDIT). *Soft Matter*, 10(17):3066–76, 2014.

Eric Brouzes, Martina Medkova, Neal Savenelli, Dave Marran, Mariusz Twardowski, J Brian Hutchison, Jonathan M Rothberg, Darren R Link, Norbert Perrimon, and Michael L Samuels. Droplet microfluidic technology for single-cell high-throughput screening. *Proc. Natl. Acad. Sci.*, 106(34):14195–14200, 2009.

Ouriel Caen, Simon S Schütz, Mani S S Jammalamadaka, Jérémy Vrignon, Philippe Nizard, Tobias M Schneider, Jean-Christophe Baret, and Valérie Taly. High throughput multiplexed fluorescence activated droplet sorting. *Prep.*, 2018.

Xiaodong Chen and Vigor Yang. Thickness-based adaptive mesh refinement methods for multi-phase flow simulations with thin regions. *J. Comput. Phys.*, 269:22–39, 2014.

G F Christopher, J Bergstein, N B End, M Poon, C Nguyen, and S L Anna. Coalescence and splitting of confined droplets at microfluidic junctions. *Lab Chip*, 9(8):1102–1109, 2009.

Jenifer Clausell-Tormos, Diana Lieber, Jean Christophe Baret, Abdeslam El-Harrak, Oliver J. Miller, Lucas Frenz, Joshua Blouwolff, Katherine J. Humphry, Sarah Köster, Honey Duan, Christian Holtze, David A. Weitz, Andrew D. Griffiths, and Christoph A. Merten. Droplet-Based Microfluidic Platforms for the Encapsulation and Screening of Mammalian Cells and Multicellular Organisms. *Chem. Biol.*, 15(5):427–437, 2008.

Roland Clift, John R Grace, and Martin E Weber. *Bubbles, drops, and particles.* Academic Press, New York, 1978. ISBN 0-486-44580-1.

Pierre Yves Colin, Balint Kintses, Fabrice Gielen, Charlotte M. Miton, Gerhard Fischer, Mark F. Mohamed, Marko Hyvönen, Diego P. Morgavi, Dick B. Janssen, and Florian Hollfelder. Ultrahigh-throughput discovery of promiscuous enzymes by picodroplet functional metagenomics. *Nat. Commun.*, 6, 2015.

Vittorio Cristini and Yung-Chieh Tan. Theory and numerical simulation of droplet dynamics in complex flows - a review. *Lab Chip*, 4(4):257, 2004.

Vittorio Cristini, Jerzy Bławzdziewicz, and Michael Loewenberg. An Adaptive Mesh Algorithm for Evolving Surfaces: Simulations of Drop Breakup and Coalescence. *J. Comput. Phys.*, 168 (2):445–463, 2001.

Erik Dahlström, Patrick Dengler, Anthony Grasso, Chris Lilley, Cameron McCormack, Doug Schepers, and Jonathan Watt. Scalable Vector Graphics (SVG) 1.1 (Second Edition) - W3C Recommendation, 2011. URL `http://www.w3.org/TR/SVG11/`.

Wei-Shen Dai and Michael J. Shelley. A numerical study of the effect of surface tension and noise on an expanding Hele–Shaw bubble. *Phys. Fluids A Fluid Dyn.*, 5(9):2131–2146, 1993.

B. E. Debs, R. Utharala, I. V. Balyasnikova, A. D. Griffiths, and C. A. Merten. Functional single-cell hybridoma screening using droplet-based microfluidics. *Proc. Natl. Acad. Sci.*, 109(29): 11570–11575, 2012.

Dennis J Eastburn, Adam Sciambi, and Adam R Abate. Identification and genetic analysis of cancer cells with PCR-activated cell sorting. *Nucleic Acids Res.*, 42(16):1–10, 2014.

Jens Eggers. Nonlinear dynamics and breakup of free-surface flows. *Rev. Mod. Phys.*, 69(3): 865–930, 1997.

H Engels. *Numerical Quadrature and Cubature.* Academic Press, London, 1980. ISBN 0-12-238850-X.

Klaus Eyer, Raphaël C L Doineau, Carlos E Castrillon, Luis Briseño-Roa, Vera Menrath, Guillaume Mottet, Patrick England, Alexei Godina, Elodie Brient-Litzler, Clément Nizak, Allan Jensen, Andrew D Griffiths, Jérôme Bibette, Pierre Bruhns, and Jean Baudry. Single-cell deep phenotyping of IgG-secreting cells for high-resolution immune monitoring. *Nat. Biotechnol.*, 35(10):977–982, 2017.

Ali Fallah-Araghi, Jean-Christophe Baret, Michael Ryckelynck, and Andrew D. Griffiths. A completely in vitro ultrahigh-throughput droplet-based microfluidic screening system for protein engineering and directed evolution. *Lab Chip*, 12(5):882—-891, 2012.

Luis M. Fidalgo, Graeme Whyte, Daniel Bratton, Clemens F. Kaminski, Chris Abell, and W. T S Huck. From microdroplets to microfluidics: Selective emulsion separation in microfluidic devices. *Angew. Chemie - Int. Ed.*, 47(11):2042–2045, 2008.

Daniel Frenzel and Christoph A Merten. Microfluidic train station: highly robust and multiplexable sorting of droplets on electric rails. *Lab Chip*, 17(6):1024–1030, 2017.

Ya Gai, Jian Wei Khor, and Sindy K Y Tang. Confinement and viscosity ratio effect on droplet break-up in a concentrated emulsion flowing through a narrow constriction. *Lab Chip*, 16: 3058–3064, 2016a.

Ya Gai, Chia Min Leong, Wei Cai, and Sindy K Y Tang. Spatiotemporal periodicity of dislocation dynamics in a two-dimensional microfluidic crystal flowing in a tapered channel. *Proc. Natl. Acad. Sci.*, 113(43):12082–12087, 2016b.

Cory J Gerdts, Valentina Tereshko, Maneesh K Yadav, Irina Dementieva, Frank Collart, Andrzej Joachimiak, Raymond C Stevens, Peter Kuhn, Anthony Kossiakoff, and Rustem F Ismagilov. Time-controlled microfluidic seeding in nL-volume droplets to separate nucleation and growth stages of protein crystallization. *Angew. Chemie - Int. Ed.*, 45(48):8156–8160, 2006.

Fabrice Gielen, Raphaelle Hours, Stephane Emond, Martin Fischlechner, Ursula Schell, and Florian Hollfelder. Ultrahigh-throughput-directed enzyme evolution by absorbance-activated droplet sorting (AADS). *Proc. Natl. Acad. Sci. U. S. A.*, 113(47):E7383–E7389, 2016.

Mathias Girault, Hyonchol Kim, Hisayuki Arakawa, Kenji Matsuura, Masao Odaka, Akihiro Hattori, Hideyuki Terazono, and Kenji Yasuda. An on-chip imaging droplet-sorting system: a real-time shape recognition method to screen target cells in droplets with single cell resolution. *Sci. Rep.*, 7:40072, 2017.

A J Goldman, R G Cox, and H Brenner. Slow viscous motion of a sphere parallel to a plane wall—II Couette flow. *Chem. Eng. Sci.*, 22(4):653–660, 1967.

P M Gresho and R L Sani. *Incompressible Flow and the Finite Element Method, Volume 1: Advection-Diffusion and Isothermal Laminar Flow.* John Wiley & Sons, Chichester, 1998. ISBN 0 471 96789 0.

Andrew J Griggs, Alexander Z Zinchenko, and Robert H Davis. Low-Reynolds-number motion of a deformable drop between two parallel plane walls. *Int. J. Multiph. Flow*, 33(2):182–206, feb 2007.

E Guyon, J-P Hulin, L Petit, C D Mitescu, and D F Jankowski. *Physical Hydrodynamics.* Oxford University Press, Oxford, 2001. ISBN 978-0-19-870245-0.

Luca Heltai, Marino Arroyo, and Antonio DeSimone. Nonsingular isogeometric boundary element method for Stokes flows in 3D. *Comput. Methods Appl. Mech. Eng.*, 268:514–539, 2014.

D a Hoang, L M Portela, C R Kleijn, M T Kreutzer, and V van Steijn. Dynamics of droplet breakup in a T-junction. *J. Fluid Mech.*, 717(2013):R4, 2013.

Dustin L House. *Applications of the Boundary-Element Method for Electrokinetics in Microfluidics*. Phd thesis, Vanderbilt University, 2012.

Haakan N Joensson and Helene Andersson Svahn. Droplet microfluidics-A tool for single-cell analysis. *Angew. Chemie - Int. Ed.*, 51(49):12176–12192, 2012.

Huan J Keh and Po Y Chen. Slow motion of a droplet between two parallel plane walls. *Chem. Eng. Sci.*, 56(24):6863–6871, 2001.

Jian Wei Khor, Minkyu Kim, Simon S Schütz, Tobias M Schneider, and Sindy K Y Tang. Time-varying droplet configuration determines break-up probability of drops within a concentrated emulsion. *Appl. Phys. Lett.*, 111(12):124102, 2017.

Balint Kintses, Christopher Hein, Mark F Mohamed, Martin Fischlechner, Fabienne Courtois, Céline Lainé, and Florian Hollfelder. Picoliter cell lysate assays in microfluidic droplet compartments for directed enzyme evolution. *Chem. Biol.*, 19(8):1001–1009, 2012.

Margaret Macris Kiss, Lori Ortoleva-Donnelly, N Reginald Beer, Jason Warner, Christopher G Bailey, Bill W Colston, Jonathon M Rothberg, Darren R Link, and John H Leamon. High-Throughput Quantitative Polymerase Chain Reaction in Picoliter Droplets. *Anal. Chem.*, 80 (23):8975–8981, 2008.

Allon M Klein, Linas Mazutis, Ilke Akartuna, Naren Tallapragada, Adrian Veres, Victor Li, Leonid Peshkin, David A Weitz, and Marc W Kirschner. Droplet barcoding for single-cell transcriptomics applied to embryonic stem cells. *Cell*, 161(5):1187–1201, 2015.

Etienne Lac and J D Sherwood. Motion of a Drop along the Centreline of a Capillary in a Pressure-Driven Flow. *J. Fluid Mech*, 640:27–54, 2009.

L D Landau, J S Bell, M J Kearsley, L P Pitaevskii, E M Lifshitz, and J B Sykes. *Electrodynamics of Continuous Media*. Pergamon Press, Oxford, second edition, 1984. ISBN 978-0-08-030275-1.

Marie Leman, Faris Abouakil, Andrew D. Griffiths, and Patrick Tabeling. Droplet-based microfluidics at the femtolitre scale. *Lab Chip*, 15(3):753–765, 2015.

Chia Min Leong, Ya Gai, and Sindy K Y Tang. Internal flow in droplets within a concentrated emulsion flowing in a microchannel. *Phys. Fluids*, 28(11):112001, 2016.

A M Leshansky and L M Pismen. Breakup of drops in a microfluidic T junction. *Phys. Fluids*, 21:023303, 2009.

David R Lide. *CRC Handbook of Chemistry and Physics.* CRC Press, Boca Raton, 85th edition, 2004. ISBN 0-8493-0485-7.

D. R. Link, S. L. Anna, D. A. Weitz, and H. A. Stone. Geometrically Mediated Breakup of Drops in Microfluidic Devices. *Phys. Rev. Lett.*, 92(5):4, 2004.

H A Lorentz. Ein allgemeiner Satz, die Bewegung einer reibenden Flüssigkeit betreffend, nebst einigen Anwendungen desselben. *Abhand. Theor. Phys.*, 1:23–42, 1907.

Linas Mazutis and Andrew D Griffiths. Selective droplet coalescence using microfluidic systems. *Lab Chip*, 12(10):1800–1806, 2012.

Linas Mazutis, John Gilbert, W Lloyd Ung, David A Weitz, Andrew D Griffiths, and John A Heyman. Single-cell analysis and sorting using droplet-based microfluidics. *Nat. Protoc.*, 8 (5):870–891, 2013.

Laure Ménétrier-Deremble and Patrick Tabeling. Droplet breakup in microfluidic junctions of arbitrary angles. *Phys. Rev. E*, 74(3):035303, 2006.

Hans-Heinrich Moretto, Manfred Schulze, and Gebhard Wagner. Silicones. In *Ullmann's Encycl. Ind. Chem.* Wiley-VCH Verlag GmbH & Co. KGaA, Weinheim, Germany, jun 2000.

Mathias Nagel. *Modeling Droplets Flowing in Microchannels.* PhD thesis, Ecole Polytechnique Fédérale de Lausanne, 2014.

Mathias Nagel and François Gallaire. Boundary elements method for microfluidic two-phase flows in shallow channels. *Comput. Fluids*, 107:272–284, 2015.

Richard Obexer, Moritz Pott, Cathleen Zeymer, Andrew D. Griffiths, and Donald Hilvert. Efficient laboratory evolution of computationally designed enzymes with low starting activities using fluorescence-activated droplet sorting. *Protein Eng. Des. Sel.*, 29(9):355–366, 2016.

C T O'Konski and H C Thacher Jr. The distortion of aerosol droplets by an electric field. *J. Phys. Chem.*, 57(11):955–958, 1953.

M E O'Neill. A slow motion of viscous liquid caused by a slowly moving solid sphere: an addendum. *Mathematika*, 14(02):170, 1967.

Deniz Pekin, Yousr Skhiri, Jean-Christophe Baret, Delphine Le Corre, Linas Mazutis, Chaouki Ben Salem, Florian Millot, Abdeslam El Harrak, J Brian Hutchison, Jonathan W Larson, Darren R Link, Pierre Laurent-Puig, Andrew D Griffiths, and Valérie Taly. Quantitative and sensitive detection of rare mutations using droplet-based microfluidics. *Lab Chip*, 11 (13):2156, 2011.

Roger Peyret. *Spectral Methods for Incompressible Viscous Flow.* Springer, New York, 2000. ISBN 0-387-95221-7.

Joseph Antoine Ferdinand Plateau. *Statique Expérimentale et Théoretique des Liquides Soumis aux Seules Forces Moléculaires.* Gauthier-Villars, Paris, 1873.

Herbert Ackland Pohl. Some effects of nonuniform fields on dielectrics. *J. Appl. Phys.*, 29(8): 1182–1188, 1958.

A Ponce-Torres, J M Montanero, M A Herrada, E J Vega, and J M Vega. Influence of the Surface Viscosity on the Breakup of a Surfactant-Laden Drop. *Phys. Rev. Lett.*, 118(2):024501, 2017.

C Pozrikidis. *Boundary Integral and Singularity Methods in Linearized Viscous Flow.* Cambridge University Press, 1992.

C Pozrikidis. *Introduction to Theoretical and Computational Fluid Dynamics.* Oxford University Press, 2011.

R F Probstein. *Physicochemical Hydrodynamics – An Introduction.* Wiley, Hoboken, New Jersey, 2nd edition, 2003.

Birte Riechers, Florine Maes, Elias Akoury, Benoît Semin, Philipp Gruner, and Jean-Christophe Baret. Surfactant adsorption kinetics in microfluidics. *Proc. Natl. Acad. Sci.*, 113(41):11465–11470, 2016.

Philip A Romero, Tuan M Tran, and Adam R Abate. Dissecting enzyme function with microfluidic-based deep mutational scanning. *Proc. Natl. Acad. Sci.*, 112(23):7159–7164, 2015.

Milton J Rosen and Joy T Kunjappu. *Surfactants and interfacial phenomena.* John Wiley & Sons, 2012. ISBN 1-118-22902-9.

Liat Rosenfeld, Lin Fan, Yunhan Chen, Ryan Swoboda, and Sindy K Y Tang. Break-up of droplets in a concentrated emulsion flowing through a narrow constriction. *Soft Matter*, 10 (3):421–430, 2014.

Youcef Saad and Martin H Schultz. GMRES: A Generalized Minimal Residual Algorithm for Solving Nonsymmetric Linear Systems. *SIAM J. Sci. Stat. Comput.*, 7(3):856–869, 1986.

Simon S Schütz, Thomas Beneyton, Jean-Christophe Baret, and Tobias M Schneider. Rational Design of a High-Throughput Droplet Sorter. *Prep.*, 2018a.

Simon S Schütz, Jian Wei Khor, Sindy K Y Tang, and Tobias M Schneider. Interaction and breakup of droplet pairs in a microchannel Y-junction. *Prep.*, 2018b.

Adam Sciambi and Adam R Abate. Accurate microfluidic sorting of droplets at 30 kHz. *Lab Chip*, 15(1):47–51, 2015.

Ralf Seemann, Martin Brinkmann, Thomas Pfohl, and Stephan Herminghaus. Droplet based microfluidics. *Reports Prog. Phys.*, 75(1):016601, 2011.

S I Shchukin and A I Grigor'ev. Critical equilibrium spheroidal deformation of a drop of dielectric liquid in a uniform electrostatic field. *Tech. Phys.*, 44(7):758–762, 1999.

J D Sherwood. Breakup of fluid droplets in electric and magnetic fields. *J. Fluid Mech.*, 188: 133, 1988.

Yulii Shikhmurzaev. *Capillary Flows with Forming Interfaces*. Chapman and Hall/CRC, sep 2007. ISBN 978-1-58488-749-2.

Staffan L. Sjostrom, Yunpeng Bai, Mingtao Huang, Zihe Liu, Jens Nielsen, Haakan N. Joensson, and Helene Andersson Svahn. High-throughput screening for industrial enzyme production hosts by droplet microfluidics. *Lab Chip*, 14(4):806–813, 2014.

Qing Song, Alexander Couzis, Ponisseril Somasundaran, and Charles Maldarelli. A transport model for the adsorption of surfactant from micelle solutions onto a clean air/water interface in the limit of rapid aggregate disassembly relative to diffusion and supporting dynamic tension experiments. *Colloids Surfaces A Physicochem. Eng. Asp.*, 282-283:162–182, 2006.

M Spiga and G L Morino. A symmetric solution for velocity profile in laminar flow through rectangular ducts. *Int. Commun. Heat Mass Transf.*, 21(4):469–475, 1994.

H Stone and L Gary Leal. The influence of initial deformation on drop breakup in subcritical time-dependent flows at low Reynolds numbers. *J. Fluid Mech.*, 206:223–263, 1989a.

Howard A Stone. Dynamics of Drop Deformation and Breakup in Viscous Fluids. *Annu. Rev. Fluid Mech.*, 26(1):65–102, 1994.

Howard A Stone and L Gary Leal. Relaxation and Breakup of an Initially Extended Drop in an Otherwise Quiescent Fluid. *J. Fluid Mech.*, 198:399–427, 1989b.

Howard A Stone and L Gary Leal. The effects of surfactants on drop deformation and breakup. *J. Fluid Mech.*, 220:161–186, 1990.

Alok Sutradhar, Glaucio H Paulino, and Leonard J Gray. *Symmetric galerkin boundary element method*. Springer, Berlin, Heidelberg, 2008. ISBN 9783540687702.

Geoffrey Ingram Taylor. Disintegration of Water Drops in an Electric Field. *Proc. R. Soc. A Math. Phys. Eng. Sci.*, 280(1382):383–397, 1964.

Ashleigh B Theberge, Fabienne Courtois, Yolanda Schaerli, Martin Fischlechner, Chris Abell, Florian Hollfelder, and Wilhelm T S Huck. Microdroplets in Microfluidics: An Evolving Platform for Discoveries in Chemistry and Biology. *Angew. Chem., Int. Ed.*, 49:5846–5868, 2010.

Todd Thorsen, Richard W Roberts, Frances H Arnold, and Stephen R Quake. Dynamic pattern formation in a vesicle-generating microfluidic device. *Phys. Rev. Lett.*, 86(18):4163–4166, 2001.

Joshua D Tice, Helen Song, Adam D Lyon, and Rustem F Ismagilov. Formation of Droplets and Mixing in Multiphase Microfluidics at Low Values of the Reynolds and the Capillary Numbers. *Langmuir*, 19(22):9127–9133, 2003.

G Tryggvason, B Bunner, A Esmaeeli, D Juric, N Al-Rawahi, W Tauber, J Han, S Nas, and Y J Jan. A Front-Tracking Method for the Computations of Multiphase Flow. *J. Comput. Phys.*, 169 (2):708–759, 2001.

P B Umbanhowar, V Prasad, and David A Weitz. Monodisperse emulsion generation via drop break off in a coflowing stream. *Langmuir*, 16(2):347–351, 2000.

J van Hunsel, G Bleys, and P Joost. Adsorption Kinetics at the Oil / Water Interface. *J. Colloid Interface Sci.*, 114(2):432–441, 1986.

Benjamin L. Wang, Adel Ghaderi, Hang Zhou, Jeremy Agresti, David A. Weitz, Gerald R. Fink, and Gregory Stephanopoulos. Microfluidic high-throughput culturing of single cells for selection based on extracellular metabolite production or consumption. *Nat. Biotechnol.*, 32(5):473–478, 2014.

Lisen Wang, Lisa a Flanagan, Edwin Monuki, Noo Li Jeon, and Abraham P Lee. Dielectrophoresis switching with vertical sidewall electrodes for microfluidic flow cytometry. *Lab Chip*, 7 (9):1114–20, 2007.

Yechun Wang and Panagiotis Dimitrakopoulos. Low-Reynolds-number droplet motion in a square microfluidic channel. *Theor. Comput. Fluid Dyn.*, 26(1-4):361–379, 2012.

George M Whitesides. The origins and the future of microfluidics. *Nature*, 442(7101):368–373, 2006.

Hengdong Xi, Hao Zheng, Wei Guo, Alfonso M Ganan-Calvo, Ye Ai, Chia-Wen Tsao, Jun Zhou, Weihua Li, Yanyi Huang, Nam-Trung Nguyen, and Say Hwa Tan. Active droplet sorting in microfluidics: a review. *Lab Chip*, 17:751–771, 2017.

Emerson Zang, Susanne Brandes, Miguel Tovar, Karin Martin, Franziska Mech, Peter Horbert, Thomas Henkel, Marc Thilo Figge, and Martin Roth. Real-time image processing for label-free enrichment of Actinobacteria cultivated in picolitre droplets. *Lab Chip*, 13(18):3707—-3713, 2013.

Bo Zheng, L. Spencer Roach, and Rustem F Ismagilov. Screening of protein crystallization conditions on a microfluidic chip using nanoliter-size droplets. *J. Am. Chem. Soc.*, 125(37): 11170–11171, 2003.

Rapolas Zilionis, Juozas Nainys, Adrian Veres, Virginia Savova, David Zemmour, Allon M. Klein, and Linas Mazutis. Single-cell barcoding and sequencing using droplet microfluidics. *Nat. Protoc.*, 12(1):44–73, 2017.

Alexander Z Zinchenko and Robert H Davis. A boundary-integral study of a drop squeezing through interparticle constrictions. *J. Fluid Mech.*, 564:227–266, 2006.

Alexander Z Zinchenko, Michael A Rother, and Robert H Davis. A novel boundary-integral algorithm for viscous interaction of deformable drops. *Phys. Fluids*, 9(6):1493–1511, 1997.

SIMON SEBASTIAN SCHÜTZ

e-mail: simon.schuetz@epfl.ch

CURRICULUM VITAE

Education

2014-2018	**PhD**, EPFL, Lausanne, Switzerland
2012-2013	**M.Sc.** (with distinction), **Computer Science**, Georg-August-Universität, Göttingen, Germany Final Mark: **1.0**
2011-2013	**M.Sc.** (with distinction), **Physics**, Georg-August-Universität, Göttingen, Germany Master Thesis: Lagrangian Properties of Transport in Weakly Turbulent Rayleigh-Bénard Convection Final Mark: **1.0**
2008-2011	**B.Sc.** (with distinction), **Physics**, Georg-August-Universität, Göttingen, Germany Bachelor Thesis: Monte Carlo Simulations of Pattern Formation on Solid Surfaces by Ion Bombardment: Effects of Surface Barriers and Mass Flows Final Mark: **1.2**
2008	**Abitur** (university-entrance diploma) Max-Planck-Gymnasium, Göttingen, Germany Final Mark: **1.0**

Awards and Scholarships

2014	**Dr.-Berliner-Dr.-Ungewitter-Award**, in Acknowledgement of the Master Thesis in Physics
2011-2013	Scholarship of the **German Academic Scholarship Foundation** (*Studienstiftung des Deutschen Volkes*, SDV)
2010	RISE Scholarship of the **German Academic Exchange Service**, for a research internship at Johns Hopkins University, Baltimore, USA
2008	**Dr. Walther Liebehenz-Preis** für besondere Leistungen in den geisteswissenschaftlichen Fächern

Publications in Peer-Reviewed Journals

1. J W Khor, M Kim, S S Schütz, T M Schneider, S K Y Tang (2017). Time-varying droplet configuration determines break-up probability of drops within a concentrated emulsion.

In: *Applied Physics Letters* 111(12), p. 124102

2. S S Schütz and E Bodenschatz (2016). Two-particle dispersion in weakly turbulent thermal convection. In: *New J Physics* 18(6), p. 065007

Conference Contributions

2017	**Poster** at *Swiss Soft Days*, Lausanne, Switzerland
2016	**Poster** at *EMBL Conference on Microfluidics*, Heidelberg, Germany
2016	**Talk** at *Capillary and Two-Phase Flows Seminar Day*, Lausanne, Switzerland
2015	**Poster** at *Gordon Research Conference on Soft Condensed Matter Physics*, New London, NH, USA
2014	**Conference Talk** at *European Fluid Mechanics Conference 10*, Copenhagen, Denmark
2013	**Poster** at *548th WE-Heraeus-Seminar on Pattern Creation in Nature and Materials*, Bayreuth, Germany
2013	**Conference Talk** at *European Turbulence Conference 14*, Lyon, France

Instruction and Teaching

2018	Supervising **Student Project** on CFD Simulation and Visualization (3rd year Bachelor students)
2009-2017	**Teaching assistant** for courses *Turbulence* (1st year Master students), *Incompressible Fluid Mechanics* (3rd year Bachelor), *General Physics* (1st year Bachelor), *Introduction to C++ programming* (1st year Bachelor)
2003-2013	**Scouting leader**, member of the organizing committee of local scouting group (CPD e.V., *Stamm Brüder Grimm*), troop leader for two years

Professional Experience

2009-2014	**Max Planck Institute for Dynamics and Self-Organization** (MPIDS), Göttingen, Germany Student assistant, software development for real-time scientific data analysis, FPGA real-time image processing, visualization
2012	**Georg-August-Universität Göttingen**, Göttingen, Germany Student assistant, software development for economic experiments at Chair for Economic Policy and SME Research
2011	**Fraunhofer Ernst-Mach-Institute**, Freiburg i. Brsg., Germany Intern, preliminary studies and simulations for LEO satellite missions
2007-2008	**Egosoft GmbH**, Würselen, Germany Part-time, software development for PC game "X3: Terran Conflict", AI routines for NPC objects, coordinating beta test